INFORMATION TO USERS

The most advanced technology has been used to photograph and reproduce this manuscript from the microfilm master. UMI films the text directly from the original or copy submitted. Thus, some thesis and dissertation copies are in typewriter face, while others may be from any type of computer printer.

The quality of this reproduction is dependent upon the quality of the copy submitted. Broken or indistinct print, colored or poor quality illustrations and photographs, print bleedthrough, substandard margins, and improper alignment can adversely affect reproduction.

In the unlikely event that the author did not send UMI a complete manuscript and there are missing pages, these will be noted. Also, if unauthorized copyright material had to be removed, a note will indicate the deletion.

Oversize materials (e.g., maps, drawings, charts) are reproduced by sectioning the original, beginning at the upper left-hand corner and continuing from left to right in equal sections with small overlaps. Each original is also photographed in one exposure and is included in reduced form at the back of the book. These are also available as one exposure on a standard 35mm slide or as a 17" x 23" black and white photographic print for an additional charge.

Photographs included in the original manuscript have been reproduced xerographically in this copy. Higher quality 6" x 9" black and white photographic prints are available for any photographs or illustrations appearing in this copy for an additional charge. Contact UMI directly to order.

U·M·I

Alloying element vaporization and emission spectroscopy of plasma during laser welding of stainless steels

Collur, Murali Mohan, Ph.D.

The Pennsylvania State University, 1988

U·M·I

The Pennsylvania State University

The Graduate School

ALLOYING ELEMENT VAPORIZATION AND EMISSION SPECTROSCOPY OF

PLASMA DURING LASER WELDING OF STAINLESS STEELS

A Thesis in

Metals Science and Engineering

by

Murali Mohan Collur

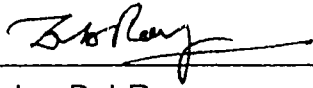Submitted in Partial Fulfillment
of the Requirements
for the Degree of

Doctor of Philosophy

December 1988
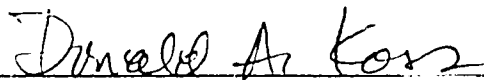
© 1988 by Murali Mohan Collur

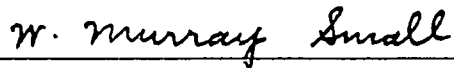We approve the thesis of Murali Mohan Collur.

Date of Signature

_____   7/16/'88

Tarasankar DebRoy
Associate Professor of Metallurgy
Chair of Committee
Thesis Advisor

_____   10/21/88

Donald A. Koss
Professor of Metallurgy
In   Charge of Graduate Programs in
     Metals Science and Engineering

_____   7-16-88

W. Murray Small
Associate Professor of Metallurgy

_____   7-12-88

John H. Hoke
Professor Emeritus of Metallurgy

_____   7/8/88

Russell Messier
Associate Professor of Engineering
     Science and Mechanics

ABSTRACT

During laser welding, the use of a high power laser beam focussed to a very small area leads to relatively high weld pool temperatures and significant vaporization of volatile elements. A fraction of the atoms of the vaporized material can become excited or ionized leading to the formation of a plasma. The plasma absorbs the laser beam energy, and in turn, reduces the power density available at the metal surface. Therefore, a knowledge of the vaporization losses and the plasma properties under various welding conditions is required as these parameters affect not only the penetration but also the composition of the weldment.

The vaporization rates and the weld pool temperatures were determined under various welding conditions using a carbon dioxide laser. Since the weld pool is surrounded by plasma during laser welding, the role of the plasma in the vaporization of alloying elements was physically modeled by allowing molten copper drops to vaporize isothermally both in the presence and the absence of plasma. Emission spectroscopy (using an Optical Multi-Channel Analyzer) was utilized to monitor the alloying element loss and for the characterization of the plasma formed during pulsed laser welding of AISI 201 stainless steels under various welding conditions. Plasma diagnostic techniques were utilized to determine the electron temperatures and the number density of electrons in the plasma to gain an understanding of the laser-plasma-solid interactions.

The overall vaporization rates during laser welding were controlled by plasma-influenced intrinsic vaporization of alloying elements from the weld

pool surface with the plasma suppressing the vaporization rate. The dominant species in the plasma were found to be iron, manganese and chromium, which were present predominantly in an excited neutral state and to a lesser extent in an ionized state. When welding was conducted at constant welding speed, shielding gas flow rate and composition, the intensities of various emissions could be used to monitor the vaporization rate and the weld pool shape. The plasma formed in an argon shielding atmosphere was found to be more than that in helium shielding atmosphere due to the lower thermal conductivity of argon. The electron temperatures were determined to be in a wide range of about 4,000 K to about 9,000 K. The electron temperatures, velocity profiles of helium gas jet and the concentration profiles of the various species in the plasma were determined by a combination of experimental and theoretical studies. This information, in turn, was used to determine the absorption of the laser beam by the plasma. The plasma enveloping the weld pool was found to absorb about 5.8 % of the total laser power. The utility of emission spectroscopy in determining the composition of the base metal was also demonstrated.

TABLE OF CONTENTS

TABLE OF CONTENTS (continued)

TABLE OF CONTENTS (continued)

LIST OF TABLES

LIST OF TABLES (continued)

LIST OF FIGURES

LIST OF FIGURES (continued)

LIST OF FIGURES (continued)

LIST OF FIGURES (continued)

ACKNOWLEDGEMENTS

I express my gratitude to my thesis advisor, Dr. Tarasankar DebRoy, for his patient discussions and help throughout the various stages of this research. Appreciation is also extended to Dr. Murray Small, Dr. John Hoke and Dr. Russell Messier for serving on the thesis committee.

The completion of this work would have been impossible without the assistance of many other people, who kindly shared their time to provide useful advice on general and particular aspects of this investigation. I wish to thank all of them including fellow students, staff personnel and faculty members.

The funding for this research was provided by the the Department of Energy, for which I am extremely grateful.

I would like to dedicate this thesis to my parents and to my late grandmother but for whose constant love, support and encouragement, the completion of this thesis would not have been possible. Last, but not the least, my heartfelt thanks to my wife, Charushree, who was a consant source of love, moral support and encouragement throughout the final stages of my doctoral work.

Chapter 1

INTRODUCTION

1.1 General introduction

The scope for technically and commercially feasible laser welding applications has increased to a large extent since the development of multikilowatt continuous wave carbon dioxide lasers (1,2). The availability of these high power lasers and the need for precision joining techniques lead to the development of various deep penetration laser welding applications. Although lasers have been utilized for a wide variety of materials processing applications, laser welding is not acceptable for the fabrication of a large number of important engineering alloys. If an alloy contains one or more volatile components, its fabrication using a high power density laser beam leads to significant vaporization of alloying elements and inadequate control of composition and properties of the weld. This problem is especially important in laser welding because the high power laser beam focussed to a very small area leads to relatively high weld pool temperature and significant vaporization of volatile elements. Vaporization may result in welds of low tensile strength and unacceptable porosity (3). The vaporized material also influences the plasma (excited and ionized atoms of the vaporized material and the shielding gas along with free electrons) composition which in turn determines the amount of the laser beam energy that reaches the substrate. This is because the plasma could reflect and absorb the laser energy which in turn reduces the power density available at the metal surface and limits weld penetration (4).

In the industrial welding environment, there is a need to monitor the alloying element loss and the properties of the weldment real-time during the welding process. In addition, an understanding of the alloying element vaporization and the role of plasma on the vaporization kinetics and the laser-solid interactions is imperative in order to optimize the welding process and the properties of the weldment. Such information relevant to laser welding of stainless steels is not available in the literature.

Figure 1 depicts some of the important physical processes occurring during laser welding leading to vaporization and plasma plume formation. The absorbed energy is deposited in a layer about 10^{-5}cm thick and penetrates into the material by thermal conduction as shown in Figure 1(a). When the surface reaches the melting temperature, a liquid interface propagates into the material as indicated in Figure 1(b). With continued irradiation, the surface begins to vaporize as shown in Figure 1(c) and a hole begins to be drilled. If the laser light is intense enough, absorption in the vaporized material leads to the formation of a high temperature plasma. The plasma can grow back along the beam toward the laser as a "laser supported absorption" (LSA) wave. The plasma absorbs a portion of the incident radiation and shields the surface as shown in Figure 1(d). The absorption of the incident laser beam by the plasma is given by

$$I(x) = I_0 \exp(-\alpha x) \qquad [1]$$

where $I(x)$ is the beam intensity emerging out of the plasma, I_0 is the incident beam intensity, α is the absorption coefficient (cm^{-1}) of the plasma and x is the domain of the plasma through which the laser beam passes.

Figure 1: A schematic diagram of the important physical processes occurring during laser welding. (adapted from reference 5).
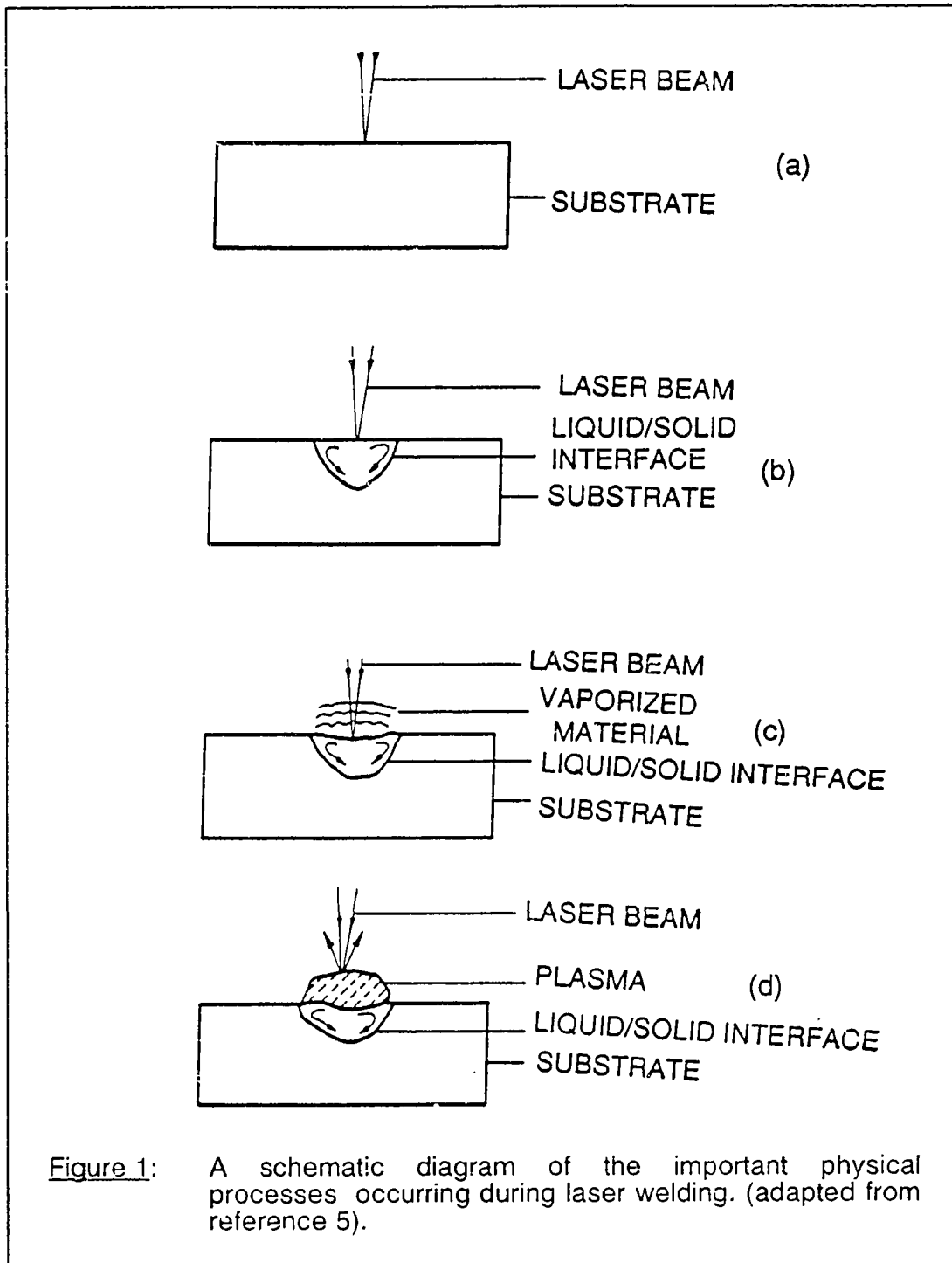
The vaporization of alloying elements during welding is a complex process which can be broadly subdivided into three steps. The first step involves the transport of the alloying elements from the interior to the surface of the weld pool aided by the fluid motion in the weld pool (6). Secondly, once the alloying element reaches the surface of the weld pool, the rate of vaporization is determined by the surface temperature distribution, local concentration of the alloying element, the extent of surface coverage by the surface active elements (which are present invariably in most iron-based alloys) and by other factors such as the surface agitation and modification of the nature of the interface due to the presence of plasma in the vicinity of the weld pool. Finally, the rate of transport of the vaporized alloying elements from the weld pool surface to the bulk gas phase depends on the nature of the boundary layer and the diffusivities of the vaporized species. The mechanism of vaporization depends on the relative contributions of these three steps in the overall rate of alloying element vaporization. A knowledge of the vaporization mechanism is essential in providing a basis for achieving a better control of the composition of the weldment.

The importance of the role of plasma is well documented in the literature. Weld properties are known to be influenced by the characteristics of the plasma formed during welding (7-9). Most of the previous work (10-18) on the characterization of plasma was undertaken to identify the species present in the welding arcs and to determine the arc temperature using emission spectroscopy. However, such information has been rather scarce for laser processing. Although emission spectroscopy is a potentially attractive technique for the monitoring of alloying element loss, the alloying element

vaporization rates have not been correlated with the emission spectroscopic data in the previous works which used emission spectroscopy during laser processing. Furthermore, the research on the extent of ionization of the plasma during pulsed laser welding of iron-based alloys is not available in the literature. In addition, the role of plasma on the vaporization kinetics is not well understood.

The quality of heat transfer calculations in the laser melted pool depends on the value of the absorption coefficient used in the computation. A significant part of the uncertainity in the prescription of the absorption coefficient is due to the attenuation of the beam energy by the plasma. The determination of the extent of absorption in the plasma would involve the temperature mapping of the plasma from which the number densities of electrons in the plasma can be determined. This in turn provides information about the absorption of $10.6\,\mu m$ carbon dioxide laser radiation by the plasma. A similar approach was taken in a recently reported study which involved temperature mapping in an argon plasma during laser processing of on Al-based alloys (19) using a multikilowatt laser in continuous wave mode. However, no such studies have been conducted on plasmas produced from stainless steel samples (which absorb the carbon dioxide laser radiation more than Al-based alloys) during pulsed laser welding.

The present study was undertaken to alleviate the lack of understanding of alloying element vaporization during welding and the nature and role of plasma during laser welding.

1.2 Statement of objectives

The overall objective of this research is to develop an improved fundamental understanding of vaporization and the role of plasma during laser welding in order to achieve a better control on the composition and the properties of the weld. More specifically, the objectives of this investigation are as follows:

(1) To study experimentally the alloying element vaporization from AISI 201 stainless steel as a function of the welding parameters in the continuous wave mode and to determine the mechanism of alloying element vaporization during laser welding of this steel.

(2) To determine the role of plasma on the vaporization kinetics.

(3) To characterize the plasma formed during pulsed laser welding of stainless steel by emission spectroscopy and to correlate spectroscopic data with the vaporization rates. This will enable one to monitor the alloying element loss in real-time during laser welding.

(4) To determine the three-dimensional plasma temperatures during pulsed laser welding of AISI 201 stainless steel from which the extent of attenuation of the laser beam by the plasma could be obtained.

(5) To demonstrate a technique for the determination of the composition of the base metal from the data obtained by emission spectroscopy.

1.3 Layout of the thesis

The thesis is divided into five chapters.

Chapter 1 deals with the introduction and the objectives of the present study and the thesis layout.

Chapter 2 is a critical review of the literature relevant to alloying element vaporization, plasma formation and plasma diagnostics using emission spectroscopy during welding.

Chapter 3 elaborates on the details of the experiments conducted to measure vaporization rates and weld pool temperature. In addition, details of the experiments conducted to determine the role of plasma on vaporization rates are also provided. The data acquisition techniques used for the characterization of plasma utilizing plasma diagnostic techniques by emission spectroscopy have been discussed.

Chapter 4 deals with the results and discussion of this study.

Finally, the conclusions of this investigation are presented in chapter 5 along with the suggestions for future work.

Chapter 2

LITERATURE REVIEW

2.1 Vaporization of alloying elements

The changes in the composition of the weldment during laser welding of many important engineering alloys are well documented in the literature (3,21-28). A 10 percent reduction in the magnesium content of the weldment was observed by Hetche et al. (21) during laser welding of Al-Mg and Al-Mg-Zn alloys. Vaporization of magnesium in these alloys led to the excessive porosity of the weldment. Blake and Mazumder (3) tried to minimize the Mg loss during laser welding of Al-Mg alloys by controlling plasma formation. This was performed by careful manipulation of experimental variables and the main gas jet in the shielding environment. Moon and Metzbower (22) found that about 20 percent of the magnesium was lost during laser welding of aluminum alloy 5456. Block Bolten and Eagar (28) had conducted experimental studies of alloy vaporization from aluminum and stainless steel weld pools in order to test a vaporization model based on thermodynamic data and the kinetic theory of gases. They concluded that the metal vaporization from the weld pool places a limit on the maximum temperature of the pool. More recently Khan and DebRoy (26) and Paul (27) have reported manganese losses from the laser weldments of AISI 202 and USS tenelon stainless steels, respectively. Figure 2 depicts the concentration of manganese in the base metal and the weld zone (determined by electron probe microanalysis) as a function of distance, which emphasizes the extent

of the manganese loss in the weldment. It is clear from these studies that there is a preferential loss of manganese and magnesium to a significant extent from high manganese stainless steels and Al-Mg alloys, respectively, during laser welding of these alloys.

It is well known that if the alloying element loss in the weldment is significant, the mechanical properties of the weld are impaired. A number of tests were conducted by the Aluminum Association (29) on aluminum-magnesium alloys containing up to 6 wt % magnesium, and their results indicated that the magnesium content decreased from 6 wt % to 3 wt % and the tensile strength decreased from 32 Kg-mm^{-2} to 20 Kg-mm^{-2}. Snow and Breinan (23) reported that the magnesium loss which occurred during laser welding of aluminum-magnesium alloys resulted in weldments of low tensile strength and excessive porosity. Similarly, during butt welding of thick (12.7 mm) plates of aluminum alloy 5456 containing 5.25 wt % magnesium by a high power (8kW, 10^6 watt/cm^2 power density) CO_2 laser, Moon and Metzbower (22) found that there was a significant degradation of the mechanical properties of the weldment due to the loss of magnesium. This is because the strength of these alloys is primarily achieved due to solid solution strengthening of magnesium in the aluminum matrix.

Denny and Metzbower (30) studied the effect of laser welding on the mechanical properties of high strength low alloy (HSLA) steels. They found some degradation of the mechanical properties, especially in the toughness of the weld metal, which was again attributed to the loss of manganese.

The vaporization of alloying elements during welding is a complex process which depends on the surface temperature distribution, the surface area of
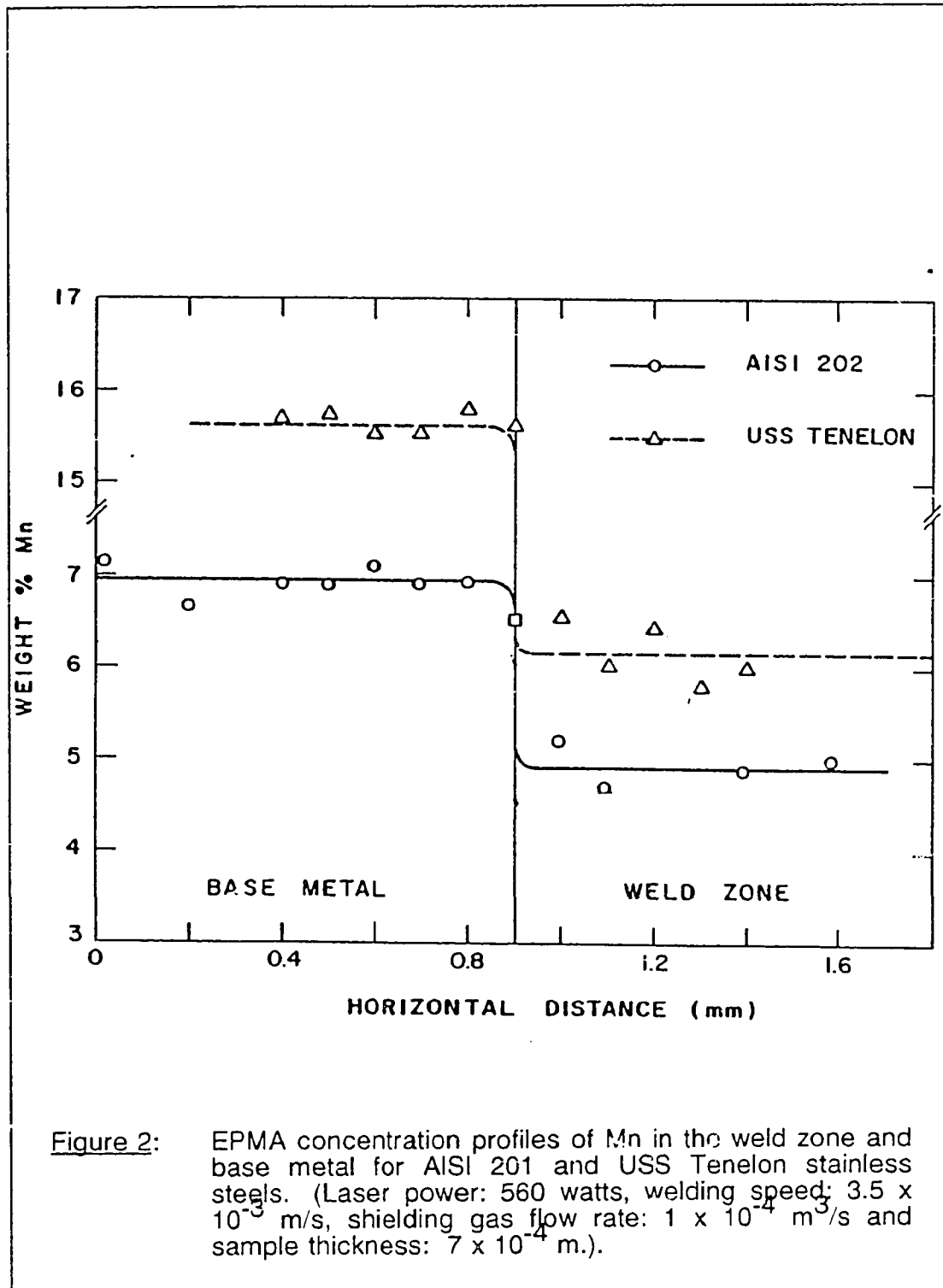
Figure 2: EPMA concentration profiles of Mn in the weld zone and base metal for AISI 201 and USS Tenelon stainless steels. (Laser power: 560 watts, welding speed: 3.5 x 10^{-3} m/s, shielding gas flow rate: 1 x 10^{-4} m^3/s and sample thickness: 7 x 10^{-4} m.).

the molten pool and various other factors (for an alloy of known composition). The overall vaporization process can be broadly subdivided into three steps. The first step involves the transport of the alloying elements from the interior to the surface of the weld pool aided by the fluid motion in the weld pool. Secondly, once the alloying element reaches the surface of the weld pool, the rate of vaporization is determined by the surface temperature distribution, local concentration of the alloying element, the extent of interfacial turbulence effects due to the surface active elements and by other factors such as the modification of the nature of the interface due to the presence of plasma in the vicinity of the weld pool. Finally, the rate of transport of the vaporized alloying elements from the weld pool surface to the bulk gas phase depends on the nature of the boundary layer and the diffusivities of the vaporized species. The mechanism of vaporization depends on the relative contributions of these three steps in the overall rate of alloying element vaporization. A knowledge of the vaporization mechanism is essential in providing a better control of the composition of the weldment. In this study, the mechanism of vaporization of alloying element loss during laser welding of AISI 201 stainless steel was determined. The role of the plasma and the surface active species (which are invariably present in most steels) on the vaporization kinetics is also assessed.

2.2 Laser induced plasma

When a laser of sufficient energy is focussed into a gaseous medium (10^9watts/cm^2) or onto a solid target (10^5watts/cm^2), a plasma is formed

(31). In recent years, plasma has been recognized as a fourth state of matter, apart from solid, liquid and gas. Just as the solid is characterized by a rigid, dense lattice structure, a liquid by a dense non-rigid fluid and a gas by a low density randomized collection of atoms or molecules, so a plasma is characterized by a collection of charged particles (ions and electrons) and also excited neutrals of low density (32). The plasma is a collection of charged particles which can range from a few percent to complete ionization. However, the net macroscopic charge of a plasma is zero. It is known that the incident laser beam is absorbed by the free electrons present in the laser induced plasma formed during laser welding (31).

Raizer (33) determined from his modeling efforts that the maintenance of plasma in ambient air requires about 2kW of well focussed light and that the estimated temperature of the resulting plasma is 18,000 K. Fowler and Smith (34) reported that for laser intensities in excess of about 10^7 watts/cm^2 the velocity of propagation of the boundary separating regions of low and high degree of ionization is supersonic. Such plasmas are referred to as laser supported detonation (LSD) waves. In contrast, at lower intensities, heating at the boundary occurs by electron and radiation diffusion and the boundary moves at a subsonic velocity. Such a plasma is referred to as a laser supported combustion (LSC) wave. Fowler and Smith's study provided considerable insight into the quantities of importance to the creation and maintenance of LSC waves at atmospheric pressure air and to the way in which the LSC waves act to impede the propagation of carbon dioxide laser radiation and the coupling of the latter to solid targets. As seen in Figure 3, the LSC wave extends into the surrounding air about 1 msec after the

appearance of a bright radiation zone, assumedly a surface material plasma, on the target surface. Complete separation of the air plasma and target occurs after about 5 msec, marking the completion of the LSC wave ignition process. Photographic measurements of the position of furthest propagation of the LSC wave front from the focal spot for a given incident power coupled with the knowledge of the dependence of the beam diameter on the distance from the focal spot permits the determination of the LSC wave maintenance threshold intensity (I_m in watts/cm^2) associated with the beam diameter at the point of furthest propagation. The LSC wave maintenance threshold intensity I_m was determined for beam diameters ranging from 0.007 to 0.5cm and while the measured value of I_m at the former diameter was in good agreement with Raizer's (33) prediction for plasmas in which thermal conduction was the principal energy loss channel, the measured variation of I_m with diameter indicated that this channel becomes less important at the larger diameters. Their results indicated that at larger diameters the ability of the laser radiation to create a plasma on the target surface is the limiting factor in determining I_i, the LSC wave ignition intensity, while at smaller diameters the capacity of the laser beam to permit this plasma to spread into the surrounding atmosphere is of greater importance. Spatially resolved measurements (by interferometric techniques) of the electron number density in a stationary LSC wave revealed detailed information of the plasma properties within the wave and was used to determine the nature of the interaction between the incident laser radiation and the plasma. It was determined that although radiation absorption through electron-ion collisions can attenuate the incident laser radiation by as much as 50 %, diminution of

the intensity at the beam focus is dominated by blooming of the beam caused by the latter propagating perpendicular to large electron density gradients in the plasma. Their work was conducted on continuous wave (CW) plasmas.

Pirri et al. (35) tried to explain the phenomenon of "enhanced thermal coupling" which occurs at high laser intensities when the effective absorptivity of the target is substantially greater than the intrinsic absorptivity of the target materials. The increase in the coupled energy which occurs with the onset of plasma formation above the surface, results from the energy transfer from the plasma that is significantly larger than direct energy transfer from direct infrared laser radiation on the target surface. They concluded that "enhanced thermal coupling" can be explained in terms of the energy transfer from the plasma ignited above the reflective metal surface, and that, at just above the plasma threshold, a strongly radiating LSC wave plasma is ignited that couples thermal energy into the target very effectively. When the laser intensity is increased and an LSD wave plasma forms, the energy transfer by radiation does not increase. The thermal coupling coefficient decreases dramatically. The local energy transfer (energy/area) coupled to the target may be less than 3 % of the laser fluence for aluminum targets at 10.6μm.

Weyl et al. (36) determined from their modeling efforts that the rapid breakdown in the metal vapor is not due to the occurence of an immediate avalanche (which would occur in the absence of inelastic processes excepting ionization) but due to ionization from excited states which are populated by inelastic collisions with electrons.

Minamida et al. (37) concluded that the heat energy of the plasma can be utilized, instead of being removed, by jetting the plasma control gas at various

t = 0 msec

t = 1 msec

t = 5 msec

t = 7 msec

t = 14 msec

t = 19 msec
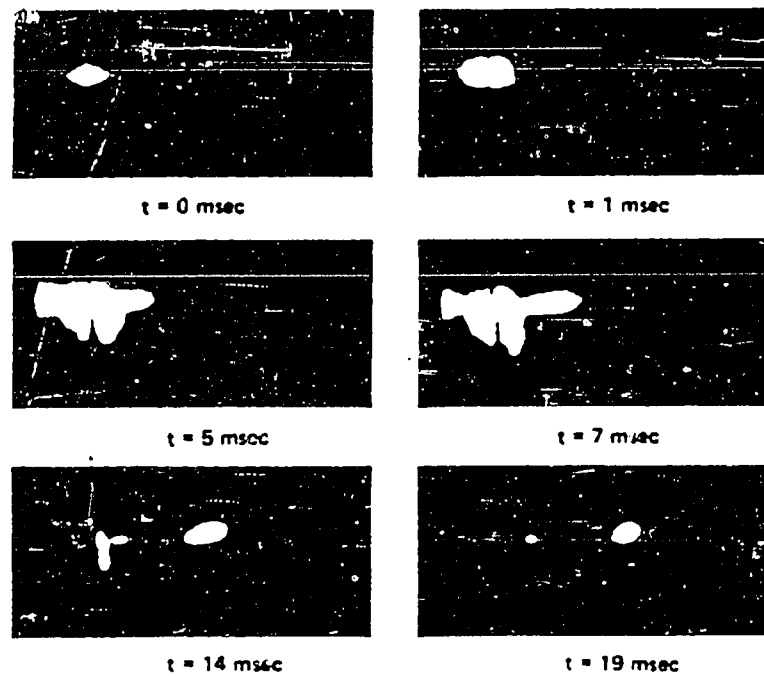
Figure 3:   LSC wave ignition and propagation at 6 kW incident power (from reference 34). The extent of target decoupling is evidenced by the disappearance of the hot spot on the steel target.

angles to the axis of the laser beam. Arnot and Albright (38) found from their study that the height of the blue plasma plumes and the red fluorescent vapor plumes is shorter when using helium shielding gas as opposed to argon shielding gas. This is due to the higher thermal conductivity of helium as compared to argon that draws the heat away from the plume and suppresses it size. Estill and Formisano (9) conducted experiments with plasma control during laser welding and found that plasma control techniques can not only be used to increase or decrease the depth of penetration in laser welds, but also eliminate or at least drastically reduce two types of porosity, i.e., microporosity (diameters of less than 0.04 cm detected by X-Ray) and root porosity (diameters of pores larger than 0.04 cm).

Dixon and Lewis (39) indicated that the laser-material interaction is initiated by the absorption of laser radiation at the material surface which results in an increase in temperature. Additionally, photoelectric and thermoelectric processes occur which yield an increase in electron density near the surface. They also pointed out the likelihood that the incident radiation is of sufficient energy density that it will vaporize surface asperities which will contribute material atoms, thermal electrons and ions to the near surface region. All of these processes serve to increase the electron, ion and neutral atom density (plasma) near the surface to the point where the laser radiation is absorbed by these particles. The heat input to the material is now complemented by the plasma. Dixon and Lewis correlated high speed movies of single pulse laser welds with optical emission from the plasma and the acoustic wave to study and model enhanced coupling. The movies and acoustic signals combined to support enhanced coupling through the development of a laser supported combustion wave from their study.

Beyer et al. (40) pointed out in their study that the critical intensity I_c for the development of a laser induced plasma during materials processing is some orders of magnitude lower than for air breakdown in ambient atmosphere. This is due to the evaporation of the solid. The ionization energy of a metal atom is considerably lower than the ionization energy of nitrogen or inert gas. This originates in plasma development below the intensity I_B of air breakdown. They concluded from their study that in the case of low plasma absorption the original beam geometry is changed by lensing effect of plasma. At intensities higher than 10^7 watts/cm^2 the target is completely enveloped by the plasma. Plasma detaches from the target and moves with detonation velocity towards the laser. The laser target interaction is interrupted until the plasma gets transparent again, based on rarefaction.

Matsunawa et al. (41) conducted experiments involving irradiation of a pulsed Nd:YAG laser beam on a titanium target in which provision was made to vary the pressure of air and argon atmosphere (used for shielding purposes) from 10 Pa (10^{-4} atm) to 3 x 10^5 Pa (3 atm). Spectroscopic measurements to characterize the plasma plume species revealed the presence of both excited neutral titanium atoms (Ti I) and singly ionized titanium ions (Ti II). They also indicated in their effort that the plume absorbs and scatters a part of the incident energy. However, the apparent absorption that accompanies light emission takes place only for a short period soon after the initiation of vaporization and the plume is weakly ionized during this short duration. The scattering of incident radiation becomes dominant after the light emission and it continues until the incident power is decreased to certain level (half the maximum power). The results of Matsunawa and Katayama (42) on

pulsed YAG laser materials processing have suggested that the control of plume as well as processing can be achieved by proper shaping of pulse wave form. Their spectroscopic measurements indicated that the emission of light was originated from the core part and its diameter corresponded to the final diameter of fusion nugget on target surface.

Lewis and Dixon (43) showed that plasma initiation and propagation during laser welding can be monitored by measuring the light intensity and sound intensity that is characteristic of a laser supported combustion wave. The techniques of high speed photography, microphone and light intensity measurements may lead to a method of real-time monitoring, at least in the Nd:YAG welding regime of average power up to 400 watts. Dixon and Lewis (44) concluded from another study that when the laser is optically coupled to the workpiece, significant current is emitted by the workpiece, current can be detected from the plasma, optical radiation emitted by the plasma is useful for monitoring purposes, and plasma generation can be monitored using microphones. The plasmas propagate as laser supported combustion waves and are expected to contribute significantly to heat input during welding. In another study, Dixon and Lewis (45) showed that more critical density plasmas are formed as the angle of incidence of the laser beam on the metal substrate (which was varied) approaches the normal. The radiation monitoring techniques which they used in this study provided data which correlated with penetration and thus are potential monitoring and control methods.

Miyamoto et al. (46) conducted experiments to optimize the gas-assisting parameters, and to reveal the role of the assist gas in controlling the plasma.

They found that the plasma formation is suppressed at assist gas pressures higher than a critical pressure P_p, P_p being slightly higher than the vapor pressure of the base metal. This is because the assist gas pressure forces the vapor in the cavity to flow away from the focussed beam. Under optimized gas-assisting conditions, helium, argon, nitrogen and carbon dioxide as the assist gas provided no appreciable difference in penetration depth. They also found that the photo-transistor which they had set at the side of welding station can monitor the behaviour of plasma removal and humping bead formation (unevenness of the weld pool surface) during gas-assisted welding in real-time.

Chennat and Albright (4) found from their emission spectroscopic evidence that during pulsed spot welding of AISI 1018 steel using a carbon dioxide laser, the plasma plume was found to contain excited and singly ionized iron under the conditions of their study (a power density of 3 to 8 x 10^5 watts/cm^2). Excited or ionized atoms of helium or argon gases which were used for shielding purposes were not found in the plasma. Arata et al. (47) tried to solve the problem of obstruction by the laser plasma, which is most severe in atmospheric laser welding, by means of vacuum laser welding. They found that below a few torr the laser plasma was almost completely suppressed, even at a welding speed of 15 cm/min. The penetration depth increased with decreasing pressure and also as the welding speed decreased.

2.3 Mechanism of formation of plasma

One can broadly classify the process of initiation and formation of a plasma under two mechanisms. First, on the basis of quantum mechanics, there is a finite probability of multiphoton absorption by a bound electron. The absorbed photon energy would be sufficient to ionize the atom, freeing the initial electron "seed." The second mechanism is cascade or avalanche breakdown. In this case, it is assumed that the initial free electron is available for photon absorption in the presence of an atom or ion. This process is called inverse Bremsstrahlung (free-free transitions) absorption. Multiphoton absorption probability can be shown to be low, especially at $10.6\mu m$ radiation which is the wavelength of the radiation of the carbon dioxide laser beam utilized in this study. For example, the ionization potential of iron is 7.87 ev and the energy of a $10.6\mu m$ photon is 0.118 ev. Thus, 67 photons need to be absorbed simultaneously at this wavelength, neglecting losses for ionization to occur in the cold gas environment. Experiments have shown that multiphoton absorption mechanism for the formation of ions is indeed negligible, especially at pressures near atmospheric. However, for the excitation of an atom wherein an electron at its normal energy level gets excited to a slightly higher level, multi-photon absorption is a probable mechanism. This is because the energy requirement for excitation is less than that for ionization.

In the avalanche or cascade breakdown mechanism, the first free electron, or, more exactly a large number of free electrons are necessary to initiate plasma and overcome loss mechanisms. On a metal surface, the plasma

starts from the free electrons existing at the evaporation threshold. This is because the free electrons form from the vaporization or thermionic emissions from the target. In the ideal case, these electrons oscillate with the electromagnetic field in the laser focal volume. The electron transfers kinetic energy to the atoms leading to an increased amount of energy in the random motion of the heavy particles. The random motion enhances the effective cross-section of the atom which facilitates inverse Bremsstrahlung (IB) absorption. IB absorption refers to a free electron absorbing the laser energy and, in the process, still remaining in its free state but increasing its kinetic energy. Therefore, an electron inside the interaction volume is accelerated by inverse Bremsstrahlung until its kinetic energy is sufficient to ionize an atom upon collision. The process results in two electrons which continue the process. From this point the density of electrons increases rapidly by an avalanche effect. The maximum electron density achievable is dependent on the laser power density and the corresponding energy loss mechanisms (31) such as electron diffusion, recombination and both elastic and inelastic collisions. Solution of particle rate equations has shown that for a laser power density greater than 10^6 watts/cm^2, the electron energy grows to a critical value in less than 10^{-8} sec. At a critical electron energy, ionization is dominant and an avalanche ionization process starts, with the result that a plasma development begins (40).

2.4 Emission spectroscopy

2.4.1 Introduction

When an atom is placed in a sufficiently strong electric field or is hit by a sufficiently swift electron (as in a discharge tube), or collided violently with another atom (as at high temperatures), it may have an electron displaced from the normal orbit (energy level) to an outer one. As the disturbed (unstable) electron falls to an orbit corresponding to a lower energy level, and ultimately to the normal orbit, it will radiate this acquired energy as a monochromatic light (48) consisting of photons.

Atomic spectra are principally concerned with the interchange of energy between the atom and electromagnetic radiation where the exchange in energy may be associated on the simplest pictoral model with a valence electron changing its orbit. Energy may be absorbed from the radiation field (absorption spectra) or may be added to it (emission spectra) (49). We will be dealing with the latter in this investigation. The actual change in energy (Δ E) between two energy levels in an atom is related to the frequency and wavelength of the radiation absorbed or emitted by the following equation (49):

$$\Delta E = E_4 - E_3 = h\nu_{43} = hc/\lambda \qquad [2]$$

where h is Planck's constant ($cm^{-1}sec$), ν_{43} is the frequency in hertz (sec^{-1}), E_4 is the energy (cm^{-1}) of the upper excited level of the electron and E_3 is the light energy (cm^{-1}) of the lower level of the electron, c is the velocity of light or electromagnetic radiation ($cm\ sec^{-1}$) and λ is the wavelength of

emission (cm). This transition from an upper energy level to a lower energy level is known as bound-bound transition, wherein the electron makes a transition from one bound state to another of lower energy. This can be understood from Figure 4 which shows the bound-bound transitions, wherein each of the transitions corresponds to a particular wavelength.

The study of plasmas using emission spectroscopy as a tool is known as spectroscopic plasma diagnostics. It enables us to obtain a large amount of information about the plasma such as the concentration of the species (semi-quantitatively), the electron temperatures, the number density of the electrons, the shape and the dimensions of the plasma without disturbing and perturbing it. This technique was utilized in the present study as it could be used to characterize the plasma by a non-contact method. However, the utilization of spectroscopic plasma diagnostics generally implies the existence of partial or complete local thermodynamic equilibrium (LTE) without which plasma characterization becomes unwieldy. Very often this limits the region of its application (50) to high electron densities (10^{14} to 10^{18} cm^{-3}). At higher electron densities (10^{20} cm^{-3}) the plasmas become optically thick in the visible and even in the ultraviolet, and the optical methods, which do not permit us to reach the deep layers, lose their advantage. Therefore, one of the main assumptions for the application of spectroscopic plasma diagnostics (apart from LTE) is that the plasma is optically thin.

2.4.2 Emission spectroscopy as applied to welding arcs

Most of the previous work utilizing emission spectroscopy for the characterization of the plasma formed during welding was undertaken to
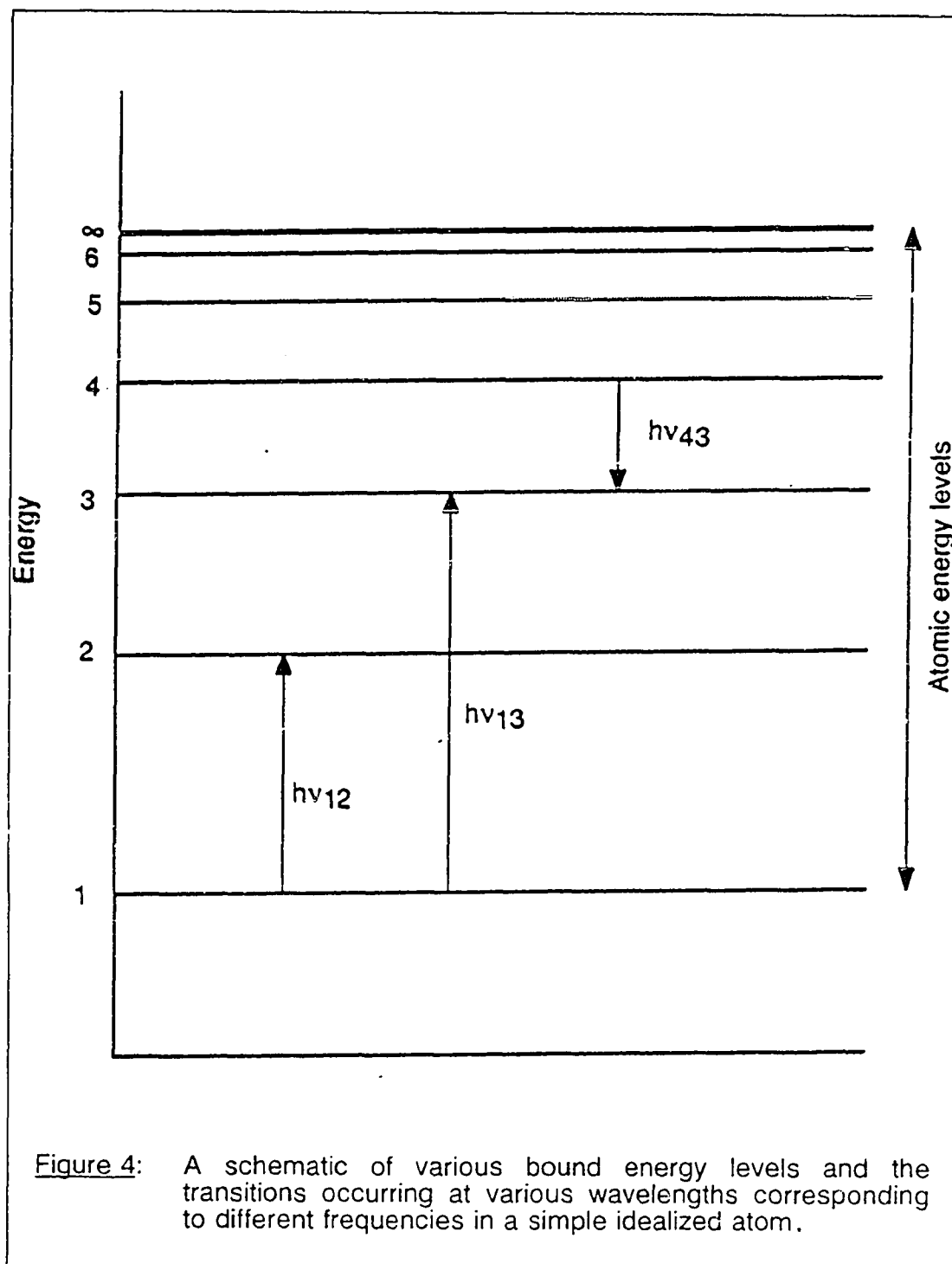
Figure 4:   A schematic of various bound energy levels and the transitions occurring at various wavelengths corresponding to different frequencies in a simple idealized atom.

identify the species present in the welding arcs and to determine the arc temperature during Gas Tungsten Arc (GTA) welding (10-18). Bennet and Mills (13) observed spectral lines from Mn, Fe, Cr and Al from spectroscopic studies of the arc during weldability studies on high manganese stainless steels. Shaw (12) had observed lines from Cr, Fe, Mn and Ar during GTA welding of 304 stainless steels. Glickstein (11) estimated the arc temperature to be 11,000 K near the cathode and 8,000 K toward the anode for a 100 ampere GTA welding arc with a 2 mm arc during welding of Ni-Cr-Fe alloy (alloy 600). Mills (17,18) demonstrated that the temperature of the welding arc was in the range of 5,000 - 6,000 K during GTA welding of 21Cr-6Ni-9Mn (weld current: 100 amperes, electrode gap: 0.06 inch) and 304L stainless steel. Metcalfe and Quigley (14) observed argon lines predominantly in the body of the arc while close to the workpiece (within a millimeter) the metal vapor lines, especially manganese lines dominate. These observations were noted during GTA welding of AISI 304L stainless steels.

Savitskii and Leskov (10) identified atomic and ionic lines for iron and manganese, in addition to finding lines of calcium, carbon and silicon during welding of standard melting (SM) and refined (ESR) high-strength steels. Key et al. (15) observed that in spectra of arcs on 304 stainless steel, manganese and chromium are the metal vapors which produce the most intense lines. Dunn et al. (16) used emission spectroscopy to study metal vapors in gas tungsten welding arcs in order to determine the effects of these vapors on arc properties and subsequently on weld bead configuration. They found from their emission spectra that in addition to the expected species (Fe, Mn and Cr), calcium and aluminum vapors were also detectable, although these

elements were present in the base plate only at very low concentrations. As a result of the previous work on the application of emission spectroscopy for the study of welding arcs produced during welding of iron-base alloys, the species present in the welding arcs and the arc temperature are now known. However, such information has been scarce for laser processing.

2.4.3 Emission spectroscopy as applied to laser produced plasmas

Emission spectroscopy has recently been used for the diagnostics of the laser produced plasmas. Adrain et al. (51) utilized emission spectroscopy to determine the electron temperatures and electron densities from line intensity and shape for different species from a metal vapor plasma produced due to the interaction of a Nd^{3+}:YAG laser beam with a mild steel component. For the pulsed spot laser welding of AISI 1018 steel, Chennat and Albright (4) detected the presence of excited and singly ionized iron atoms in the plasma, but did not find any evidence of excitation or ionization of helium or argon. From the analysis of emission spectroscopic data, Rockstroh and Mazumder (19) calculated electron temperatures in excess of 17,000 K in pure argon plasma and in the plasma produced by laser irradiation (7 kW) of aluminum targets in argon atmosphere. In the power density range from near plasma threshold to 5×10^7 watts/cm^2, Knudston et al. (20) determined the electron temperature to be about 8,000 K for laser produced aluminum plasmas.

2.4.4 Emission spectroscopy as applied to the study of role of surface active elements

One of the major problems during welding is the variability in the size and shape of the welds among various heats of the same material. With increasing automation in the industry, the trend is to produce clean steels and other alloys. However, minor variations in composition are common in alloys of different heats of the same nominal composition. This in turn leads to variable properties of the weldment in terms of their geometry and other properties. There is an abundance of literature (10,13,14,16,27,51) in the welding area on the variations in the weldability of the materials as a result of varying concentrations of minor amounts of surface active elements during both GTA welding and laser welding. However, there are a few studies (10,16) which involved determination of the effects of minor impurities on the amount of metal vapors (monitored by emission spectroscopy) during GTA welding. Savitskii and Leskov (10) studied the wavelength region between 240 nm and 250 nm and identified Ca, Fe, Mn, Si and C lines from arcs on high strength steels. They found that the introduction of an oxygen containing flux caused a decrease in the intensity of Ca, Fe and Mn lines and an increase in Si and C lines. Dunn et al. (16) found that the presence of sulfur in the base plate appears to promote evaporation of manganese and iron during GTA welding of different heats of 304L stainless steels. They also found that the addition of oxygen to the shielding gas results in a decrease in the concentration of calcium, manganese and aluminum vapor in the arc, and a dramatic increase in the concentration of tungsten vapor. This was attributed to the differences between vapor pressures of metals and their oxides.

Although some work has been conducted on the role of surface active elements on the vaporization of metal vapors during GTA welding, no work has yet been reported on the role of these elements on the vaporization of alloying elements during laser welding.

2.4.5 Line broadening effects

The properties of the plasma, viz., the number density of electrons and particle temperatures can also be determined from the measurement of spectral line broadening. The final profile of a spectral line has contributions from the physical and the instrumental factors. The former occurs by virtue of the physical conditions in the source of the excitation, i.e., before the interference from the spectroscope. The latter, i.e., the profile due to the instrumental factor is the pattern that results from the influence of the spectrographic equipment on a uniform intensity distributions. For the determination of the properties of the plasma, the physical profile is important. The physical profile stems from the contributions due to the Stark (pressure) and Doppler broadening. These broadening mechanisms compete and make the resolution of individual contributions difficult.

Stark broadening occurs when the ions are present in significant quantities, wherein the atom is also radiating in the presence of electric fields, which consequently perturb the normal energy levels by way of the Stark effect. Variations of the electric fields through the plasma result in a spread of the Stark levels from individual atoms and produce a statistical broadening of the spectral lines. Therefore, Stark broadening is essentially due to the forces exerted on the electrons by the neighbouring heavy particles. The measured

line width at half maximum is proportional to the electron number density, as given by the following equation (50):

$$N_e = C(N_e, T) \, \Delta\lambda_{1/2}^{3/2} \qquad [3]$$

where $\Delta\lambda_{1/2}^{3/2}$ is the total width of the profile at half-height, N_e is the electron density and the coefficient $C(N_e, T)$ is a factor which depends only slightly upon the electron density N_e and the temperature T and tabulated by Griem (53). This technique has been used successfully in systems where the hydrogen Balmer series H was resolvable (50,53).

Doppler broadening occurs due to the random motion of the radiating of emitting atoms. The measured line width at half maximum is proportional to the particle temperature as given by the following equation (54):

$$w_D = 7.16 \times 10^{-7} \lambda (T/M)^{1/2} \qquad [4]$$

where w_D is the width at half height of the line T is the electron temperature, M is the atomic weight and λ is the wavelength of the line in angstroms. Doppler broadening results in a Gaussian line profile which is difficult to resolve from the Stark effect.

The extent of wavelength broadening which could stem from Stark and Doppler effects is comparable to the instrumental line broadening in this study which is about 0.6 $^{\circ}$A when a 1200 lines/mm diffraction grating was used in the monochromator. Therefore, the available techniques of measuring electron temperatures and number densities from Doppler and Stark effects, respectively, were not utilized in the present study.

2.5 Summary

Although significant changes in the chemical composition and the properties of the weld metal due to alloying element loss were recognized in the earlier work, the emphasis in the past work was on the characterization of the final product and not on the fundamental mechanism of vaporization and the role of plasma on vaporization on which improved control of chemical composition and properties of the fabricated product can be based.

The importance of the role of plasma during welding is well documented. Although emission spectroscopy has been used to characterize the welding arcs during GTA welding, it has not been used extensively to characterize the laser plasma during laser welding. In addition, no attempt has been made in the earlier studies to correlate the alloying element vaporization rates with the emission spectroscopic data which could provide a capability of real-time monitoring of alloying element loss. This is especially useful in industrial environment wherein the emission spectroscopic data can be obtained real-time from the plasma during laser welding. In this study suitable sensors have been developed which will facilitate the monitoring of the laser welding process.

There is an abundance of literature on the effect of minor surface active elements such as sulfur and oxygen on the weld penetration during both GTA welding and laser welding. However, there is a lack of information on the role of these impurities on the vaporization behavior on which improved control of chemical composition and properties of the fabricated product can be based.

There is no information available in the literature on the plasma temperature, the extent of ionization and the extent of attenuation of the laser beam by the plasma produced during pulsed laser welding of high manganese stainless steels. A three-dimensional mapping of the plasma or the electron temperature will provide insight into the number density of electrons and the plasma domain. This information, in turn, will give an insight into the extent of attenuation of the laser beam by the plasma due to inverse Bremsstrahlung absorption.

Chapter 3

EXPERIMENTAL PROCEDURES

3.1 Vaporization during continuous wave mode laser welding

A carbon dioxide laser, Coherent Model # 525-1, capable of producing a maximum output power of 575 watts in the continuous wave mode was utilized. The laser beam was focussed onto the surface of the sample by a 12.7 cm focal length Zn-Se lens with an anti-reflection coating. Experiments were conducted with AISI 201 stainless steel samples typically of dimensions 4 cm long, 1.5 cm wide and 0.05 to 0.1 cm thick. These samples were placed on a remotely controlled, electrically operated table capable of providing linear speeds in the range of 0.1 to 5 cm/sec. Some of the later experiments were conducted by using a computer controlled table capable of providing motion in two mutually perpendicular directions along the horizontal plane, the maximum linear speeds attainable being about 6 cm/sec. The table on which the samples were clamped was placed inside a plexiglass box, which arrested any stray laser beam and provided a controlled atmosphere during laser welding. The controlled atmosphere was maintained by passing a shielding gas (helium or argon) through a copper nozzle mounted coaxially with the emerging laser beam. The gas flow rate was monitored by a flowmeter. Prior to the fabrication of the welds, the laser power was adjusted and measured with a power meter.

A portion of the vaporized material was collected as a condensate on the inner surface of a hollow, cylindrical, both-end-open quartz tube which was
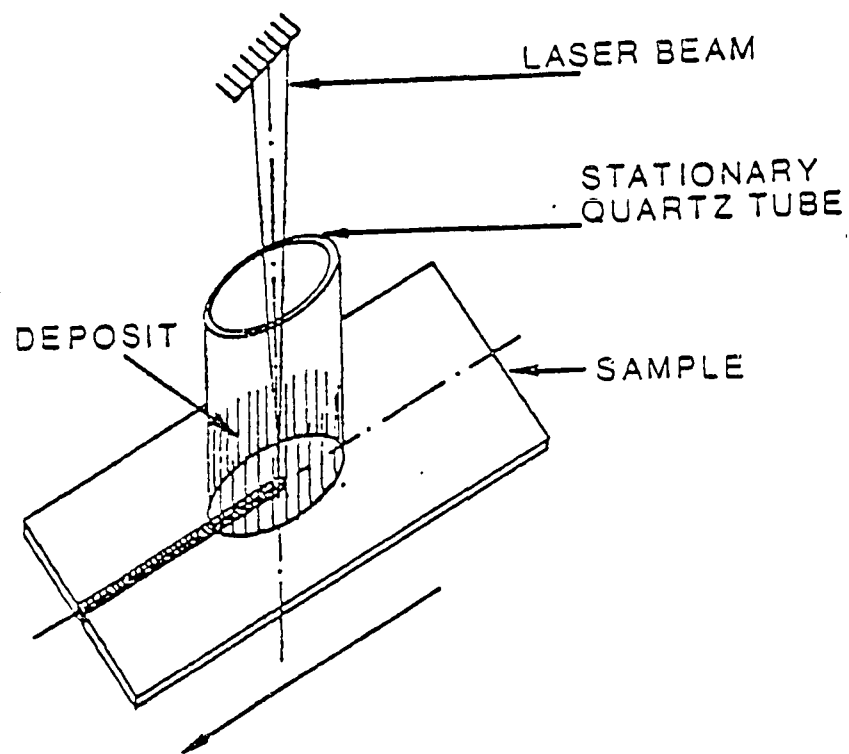
Figure 5: Schematic diagram showing the position of the quartz tube with respect to the laser beam for collecting part of the vaporized material.

held stationary and coaxial with the laser beam as shown in Figure 5. The composition of the condensate was determined by electron probe microanalysis (EPMA) and atomic absorption (AA) techniques. The compositions of the base metal and the weldment were determined by EPMA. Most of the experiments were conducted with a high manganese austenitic stainless steel (AISI 201). The chemical composition of the steel is presented in Table 1. It can be noted from the table that the contents of the alloying elements in this steel, viz., Cr, Mn and Ni are substantial. In addition, minor surface active impurities such as sulfur and oxygen are also present.

The sample was weighed accurately before and after welding and the vaporization rate was measured by dividing the difference in the weight of the sample with the total laser-solid interaction time. To minimize the errors in weighing the samples, several passes at different adjacent locations on the sample were made so as to ensure a sufficient loss of material from the samples. The vaporization rate was studied as a function of various welding parameters such as the laser power, welding speed, type of the shielding gas and its flow rate under both continuous wave mode laser welding. The width and the depth of the weld pool were determined by optical microscopy of the specimen after welding.

3.2 Role of plasma on the vaporization kinetics

It is a difficult task to determine the role of plasma on vaporization rate as plasma is invariably present above the weld pool and one cannot create conditions in which plasma is absent and present above the weld pool under

Table 1: Chemical composition of AISI 201 stainless steel.

Element	Wt %
Cr	16.34
Ni	4.87
C	0.073
Mn	7.15
Si	0.56
P	0.035
S	0.004
N	0.069
O	0.004
Al	0.003
Fe	Balance

identical welding conditions. Therefore, in this study, the role of plasma on the kinetics of vaporization rate was physically simulated by conducting isothermal experiments with pure copper both in the presence and absence of an argon plasma created in our laboratory. The experimental set-up for this study is shown in Figure 6. About 5 x 10^{-4} Kg of electrolytic grade copper (wt % Cu, 550 ppm O, 30 ppm S) was placed on an alumina substrate inside a long vycor tube which was filled with ultra high purity argon or helium at a predetermined pressure. The sample was heated by means of a two-color pyrometer through an optical grade window fitted at one end of the vycor tube. No condensation of vapors was observed on the window. The low pressure inert gas plasma was characterized by emission spectroscopy (55) in our laboratory. From the spectra obtained, it was found that the plasma contained both excited neutral and ionized argon species which is very much similar to the laser plasma observed during laser welding. The intensity of the various peaks of the spectra could be controlled by varying the input power (current) and the chamber pressure. At a predetermined plasma intensity, the temperature of the droplet was controlled by adjusting the position of the droplet with respect to the induction coil. The copper vaporization flux was determined from the weight loss of the sample, the surface area of the exposed copper droplet and the time for which the samples were maintained at a particular temperature (duration of the experiment).
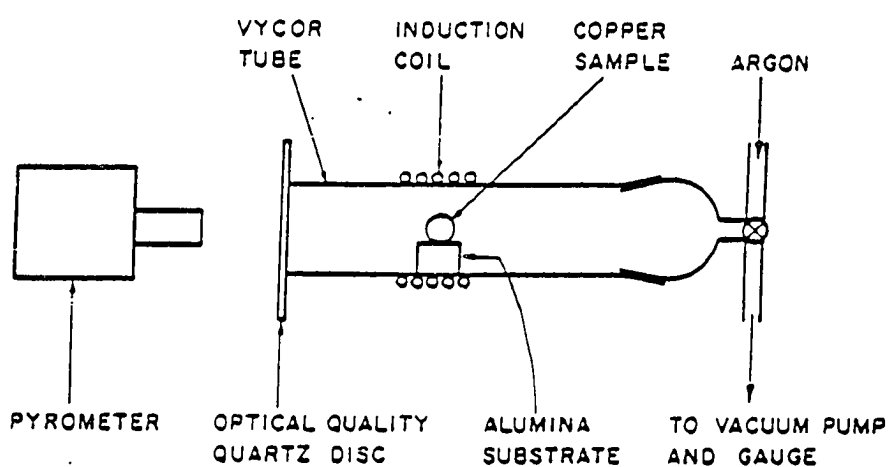
Figure 6:   Schematic diagram of the experimental set-up used for isothermal vaporization experiments with copper at reduced inert gas pressures.

3.3 Emission spectroscopic studies

3.3.1 Spectroscopic equipment

Figure 7 is a schematic diagram of the experimental set-up used for the emission spectroscopy studies. As can be seen from the figure, the radiation emitted from the plasma is focussed on the slit of a monochromator through a convex lens. The monochromator (Instrument SA Model HR 320), in turn, has a kinematically mounted diffraction grating in order to obtain a high resolution spectra. The optical multichannel analyzer assembly includes an intensified silicon intensified target detector (ISIT PAR Model 1254) which detects the emission from the plasma at the exit slit of the monochromator which, in turn, splits the radiation from the plasma into different wavelengths. The detector, in turn, was connected through an ISIT detector controller (PAR Model 1216) to the console of the optical multichannel analyzer (OMA). Some of the earlier experiments were conducted with OMA II while some of the later experiments were conducted with OMA III, the latter being equipped with more sophisticated and versatile software than the former.

The two-dimensional vidicon detector is a silicon intensified target (ISIT) detector, 500 by 512 pixels. The pixels are 25 by 3 micrometers with a total active area of 12.2 mm by 12.5 mm. The monochromator is utilized in a spectrograph configuration. Thus the two dimensions of the detector correspond to the spatial extent of the entrance slit length (parallel to the plasma domain) and the spectral spread of the diffraction grating (the total window of the wavelength observed). For the majority of the experiments in this investigation, a 1200 lines/mm holographic diffraction grating was used. This results in a resolution of 0.5 to 0.6 Angstroms at the detector face.

LASER
BEAM

MONOCHROMATOR

OPTICAL
MULTICHANNEL
ANALYZER

CONTROLLED ATMOSPHERE
WELDING CHAMBER

Figure 7:   Schematic diagram of the experimental set-up used for the
emission spectroscopy studies.
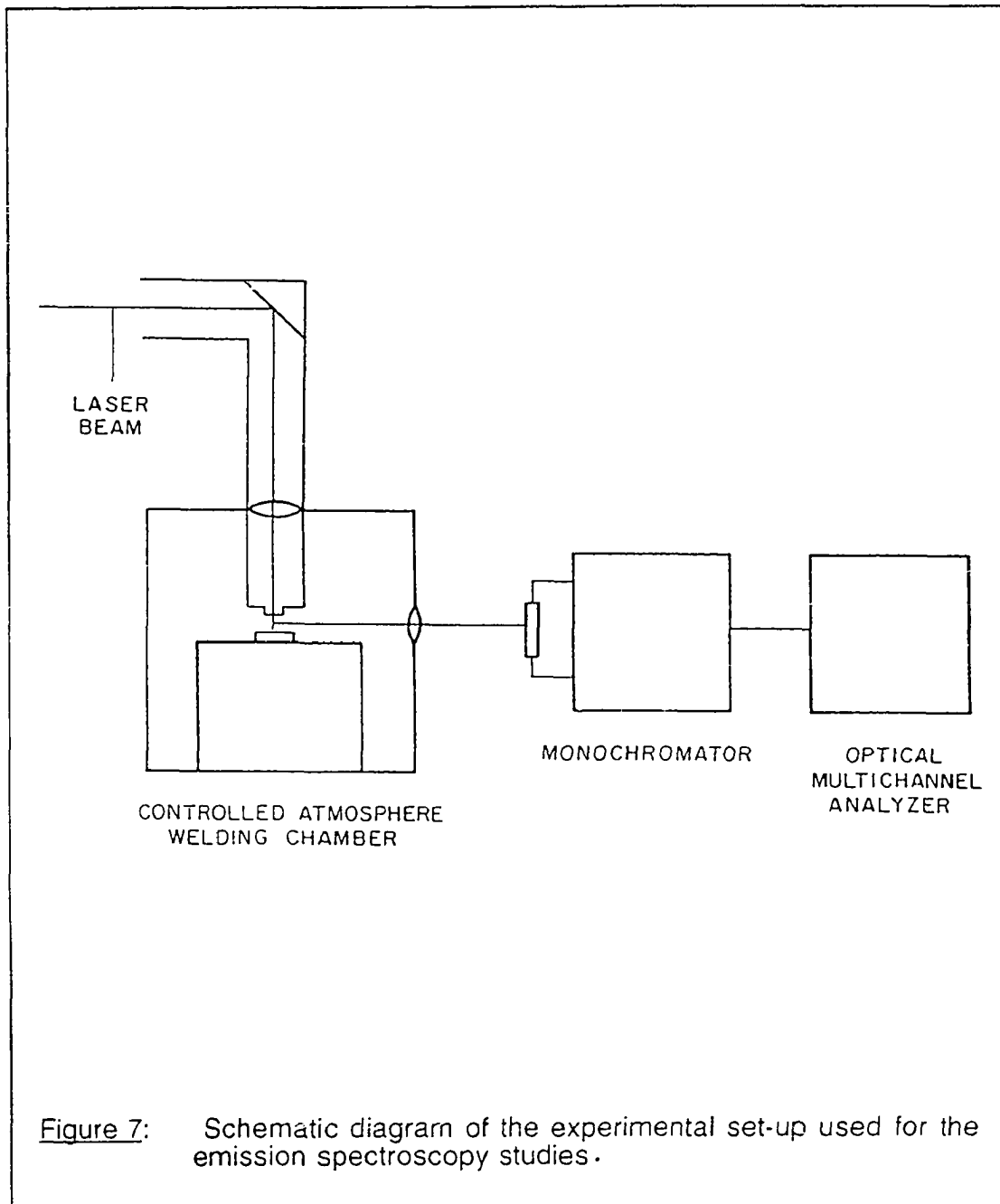
3.3.2 Data acquisition for process parameter study

The monochromator was first calibrated using an argon lamp (ORIEL Model 6030) such that each channel corresponded to a particular wavelength. The data were collected over multiple scans per axial location to increase the signal to noise ratio. Intensities of the peaks were calculated by subtracting the background noise from the observed intensities. The intensities of major peaks of Fe, Mn and Cr were monitored as a function of laser energy, welding speed, shielding gas flow rate and composition. The total vaporization rates were also calculated from weight loss measurements under these conditions. In all the studies involving emission spectroscopy the laser was operated in the pulsed mode. In all the experiments involving the variation of the process parameters, the monochromator slit was placed vertical and a 1200 lines/mm diffraction grating was used. A 2.5 mm high band at the center of the 12.5 mm x 12.5 mm square ISIT target was monitored in order to avoid peripheral effects due to aberrations to prevent increased linewidth and, thus, reduced resolution (56).

3.3.3 Data acquisition for the minor element effect study

Since all commercial alloys contain several chemical species in low concentrations, the effects of sulfur and oxygen were studied with ultrapure iron (less than 10 ppm total impurities). Samples were doped with sulfur and oxygen in a high temperature furnace using H_2/H_2S and CO/CO_2 mixtures, respectively. The temperatures and gas compositions utilised for doping were determined on the basis of available thermodynamic data (57,58) and

the values of these parameters are presented in Table 2. The values of wt % S and wt % O reported in the table correspond to the amount of these impurities present in equilibrium with iron at the relevant temperatures (57,58) at which the experiements were carried out. The oxidized iron samples were prepared by heating specimens in a muffle furnace at 873 K for about two hours. A 600 lines/mm diffraction grating was used for the emission spectroscopic studies of the doped, oxidized and undoped iron samples. The oxygen-doped, sulfur-doped and the oxidized samples were treated separately with the laser beam under conditions identical to the ultrapure iron sample which was used as a control. The emission spectra and the vaporization rates of the doped and the oxidized samples were compared with those for the ultra pure iron samples. The electron temperatures of the plasma were also determined from the emission spectra.

3.3.4 Data acquisition for the determination of the plasma temperature distribution.

For experiments involving the plasma temperature distribution, the entrance slit of the monochromator was placed horizontally. The plasma event in all cases is vertical. In order to minimize the effects of buoyancy, the plasma was imaged onto the horizontal slit as shown in Figure 8. By dividing the detector spatial dimension into N individual tracks, the entrance slit and, hence, the plasma radial dimension, is effectively divided into N elements. The minimum number of pixels in a given track was five. Therefore, each track had a width of five pixels. This dimension is the means of calculating the radial dimension of the plasma volume. For example, five elements out of

Table 2: Experimental conditions used for doping sulfur and oxygen into ultrapure iron samples (time of experiment = 3 hours).

	Temperature (K)	H_2S/H_2 (Molar Ratio)	CO_2/CO (Molar Ratio)	Wt %i
Sulfur Doping	1273	5.45×10^{-3}	-	0.013
Oxygen Doping	1603	-	0.171	0.002

Figure 8: The experimental arrangement used for the determination of plasma temperature distribution.
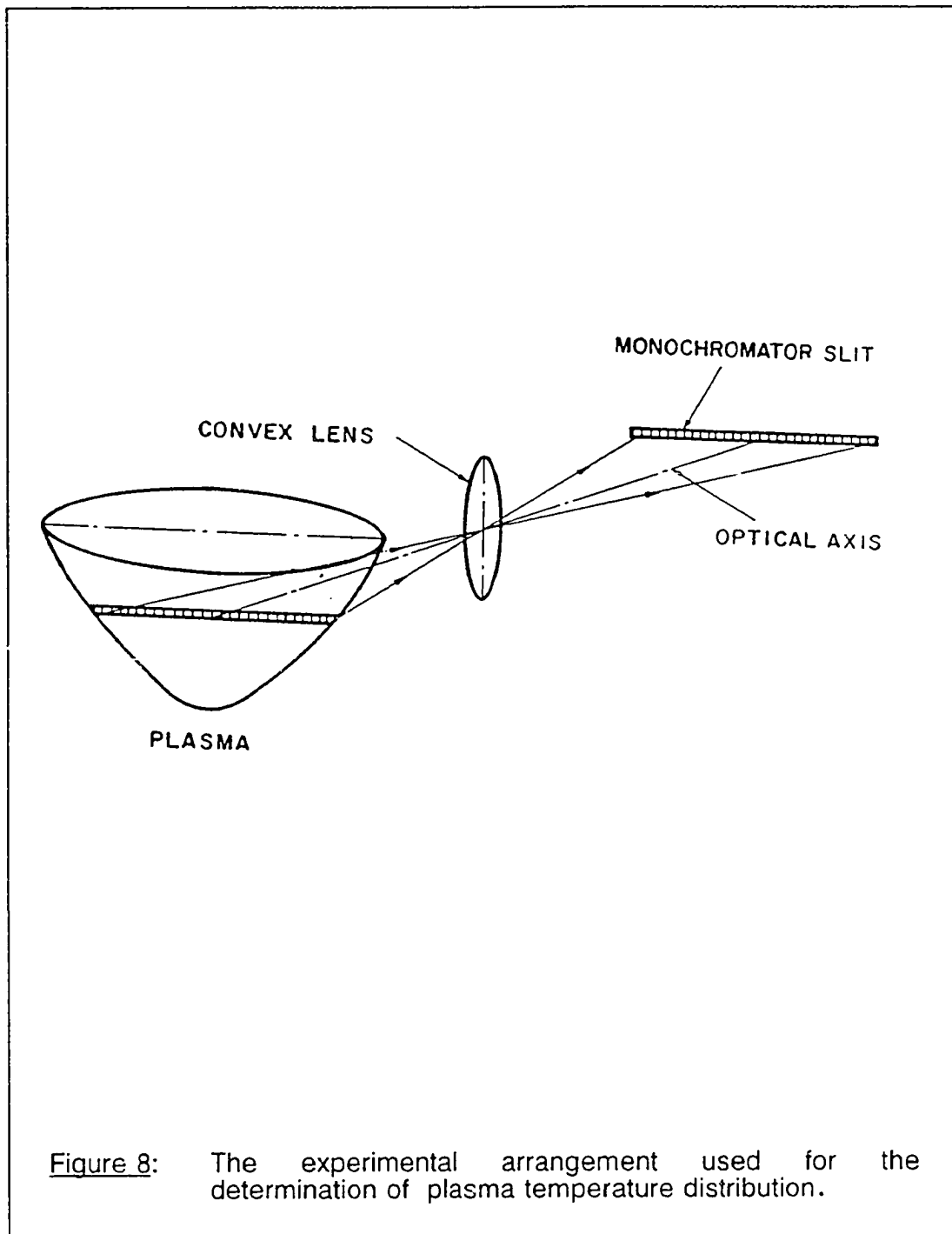
500 elements correspond to the radial increment. Since 500 pixels or elements of the detector corresponds to 12.2 mm, the radial increment at the detector is 5/500 x 12.2 mm = 0.122 mm.

In order to calculate the magnification of the monochromator, one follows the guidelines of Levner and Thevenson (59) who found that the magnification of the monochromator will be about 1.1 times. Thus the radial increment at the entrance slit is 0.122/1.1 mm = 0.111 mm. The actual radial increment at the plasma is the value divided by the magnification of the optical system (convex lens in this case). The optical magnification is v/u, where v and u are the distances in cms from the lens to the entrance slit of the monochromator and the plasma, respectively. Therefore, the actual increment at the plasma is 0.111/(v/u) cms. Efforts were taken to ensure that the size of the plasma image was less than the total sensitized region of the detector. The axial increment is somewhat easier to calculate being equal to the slit width divided by the optical magnification. Thus for a 10 μm slit width, the axial dimension is 0.01/(v/u) mm.

Once the detector has been divided into N tracks, each track is spectrally spread across the other detector dimension which corresponds to wavelength. The OMA is now ready for multi-track scanning and the experimental intensities of two manganese peaks from the plasma were collected for various tracks.

The samples used for this study were AISI 201 stainless steel samples of dimensions 0.09 m length, 0.04 m width and 0.0025 m thickness. The longer and wider samples used for this study, as compared to the samples used for process parameter study, is because the total time needed for the OMA to

obtain the data in multi-track mode is about 7 seconds. Therefore, the laser-solid interactions time has to be more than 7 seconds to ensure the existence of plasma throughout the scans at a welding speed of about 5 mm/sec. The data were collected in multi-scan mode to increase the signal to noise ratio and the background radiation was subtracted from the data.

Once the data are collected at a particular horizontal location of the plasma, the monochromator and the convex lens were moved at various vertical locations by a computer controlled table. Thus, the horizontally placed entrance slit of the monochromator scans the various thin horizontal slices of the plasma. From this data, one obtains an overall three-dimensional temperature profile of the plasma. The slit is moved vertically up and down till it is unable to detect the two manganese peaks which were monitored in these experiments. This enabled the location of the two vertical boundaries of the plasma domain. The plasma was also centered with respect to the entrance slit by horizontal adjustment of the slit and the convex lens assembly. The distance between the lens and the entrance slit was adjusted such that a well focussed image of the plasma was obtained.

The calibration for these experiments was conducted by using a combination of neon and argon lamps which exhibit peaks in the range of 5250 to 5500 $^{\circ}$A range. This range was selected because the two manganese peaks which were monitored are observed at 5341.06 $^{\circ}$A and 5377.64 $^{\circ}$A, respectively. The shielding gas used for all these experiments was helium and the laser was operated in the pulsed mode.

Chapter 4

RESULTS AND DISCUSSION

4.1 Vaporization studies

4.1.1 Mechanism of vaporization

In many well-defined flow systems, the gas phase mass transfer rates can be estimated from the appropriate mass transfer correlations available in the literature. In laser welding, inherent complexities such as the presence of excited neutral atoms and ionized species in the plasma and their interactions with the laser beam preclude the application of the existing mass transfer correlations. Therefore, the role of the gas phase mass transfer in the overall vaporization rate was based on the results of a series of critical experiments (86). The examination of the role of transport in the liquid phase was based on the computed fluid flow field (27).

Transport of alloying elements in weld pools is affected by the circulation of molten metal resulting from the spatial variation of surface tension due to the existence of a strong surface tension gradient at the surface of the weld pool. The velocity vector plot of the flow pattern in the weld pool obtained by the simultaneous solutions of the equations of change (27) revealed that the weld pool surface can be renewed about two hundred times in the time period required for the laser beam to scan a distance equal to the weld pool width at a welding speed of about 0.5 cm/sec. Therefore, the liquid phase is considered very well mixed and the transport in the liquid phase does not inhibit vaporization.

An additional evidence of rapid liquid phase mass transport was obtained by Khan (60) whose secondary ion mass spectrometric studies did not indicate the existence of a concentration variation near the surface of the weld pool characteristic of liquid phase mass transfer controlled vaporization.

If the gas phase mass transfer is the rate controlling step in the overall vaporization process, the diffusivities of the vaporizing species (e.g., manganese) in the shielding gas (e.g., helium) should have an effect on the vaporization rate. Furthermore, since the flow rate of the shielding gas influences the mass transfer coefficient, its change is also expected to have an influence on the rate if the rate is gas phase mass transfer controlled. The diffusivities of manganese and iron in helium is about four times that in argon or nitrogen (86). With this in view, the rates of vaporization of alloying elements from AISI 201 stainless steel were experimentally measured using various shielding gases and flow rates (86). It was noted that the vaporization rate is insensitive to changes in the diffusivity of the vaporizing species and the flow rate indicating that the gas phase mass transfer step does not contribute significantly to the overall vaporization rate during continuous wave mode laser welding.

4.1.2 Vaporization at the weld pool surface

From the discussions in the previous sections, it is clear that the resistances offered by the liquid phase and gas phase transports in the overall vaporization of alloying elements are insignificant and the slowest step is the vaporization reaction at the weld pool surface. An expression for local vaporization flux on the weld pool surface at low pressure can be given by the following equation (28):

$$J_i(T) = 44.34 \; P_i(T) \, / \, (M_i T)^{0.5} \qquad\qquad [5]$$

where $J_i(T)$ is the flux of species i in moles/$(cm^2 sec.)$, $P_i(T)$ is the partial pressure of species i over the alloy (at the relevant temperature) in atm., M_i is the molecular weight of the species i in gms/mole and T is the temperature in Kelvin.

The vaporization rate for a component i can be obtained by integrating the local vaporization fluxes given by equation [5] over the weld pool surface. The overall vaporization rate is obtained by adding the individual vaporization rates of the various vaporizing species. The surface temperature profiles obtained from the solution of the equations of change were used to calculate the total vaporization rate given by the following equation:

$$\dot{v} = \sum \int_0^r 2\pi J_i(T) \, r \, dr \qquad\qquad [6]$$

where v is the total vaporization rate in moles/sec for a species i and r is the radial distance from the center of the weld pool.

Vaporization rates of various alloying elements were computed as a function of the radial distance. For these calculations, equilibrium vapor pressures over pure liquid iron, manganese, chromium and nickel were obtained from the literature and the data are presented in appendix A. The partial pressure values over the stainless steel appearing in equation [5] were obtained by multiplying the equilibrium vapor pressure values with the mole fractions of the corresponding elements. The temperature distribution obtained numerically at various laser powers (27) are presented in Figure 9. Using the temperature distribution at the surface of the weld pool when 500
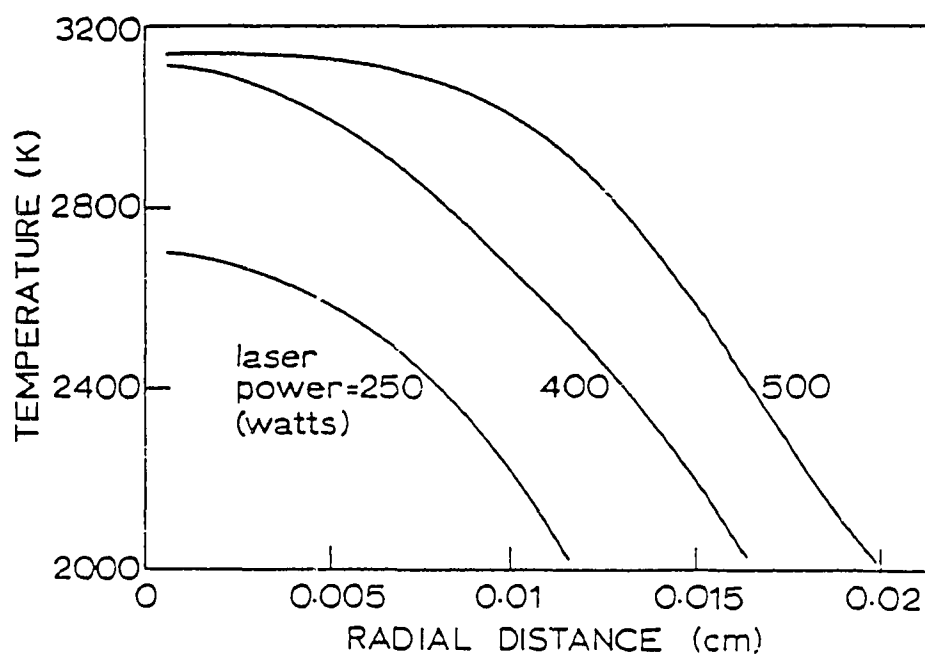
Figure 9: Radial variation of temperature at various laser powers (from reference 27).

watts of laser power was used, the computed values of the vaporization flux are presented in Figure 10 as a function of the distance from the axis of the laser beam. Similar calculations were performed for welding at various other laser powers. These calculated rates along with the experimentally observed vaporization rates (all elements taken together) are plotted as a function of laser power in Figure 11. It is observed from this figure that the theoretically calculated vaporization rates are substantially higher than the vaporization rates determined experimentally. However, in these calculations the effect of plasma (which is inevitably present above the weld pool during laser welding) was ignored.

4.1.3 Effect of plasma on the vaporization rate

To determine the effect of plasma, vaporization rates of pure copper samples were determined under reduced pressure with and without the presence of plasma. The results of these experiments are plotted in Figure 12. In experiments with plasma, the plasma intensity was maintained constant by keeping the coil configuration, coil current and the chamber pressure of argon (210 μm Hg) constant (55) at all temperatures. It is observed from this figure that the vaporization flux is decreased significantly when plasma is present. The reduction in the vaporization rate of copper is compatible with the enhanced condensation of copper vapors due to a space charge effect (88) shown schematically in Figure 13. The ionized and excited copper and argon atoms shown in this figure were detected in the plasma by emission spectroscopy (55). In view of the high mobility of the electrons

Figure 10: Vaporization flux of alloying element calculated from the Langmuir-Knudsen equation (equation [5]).
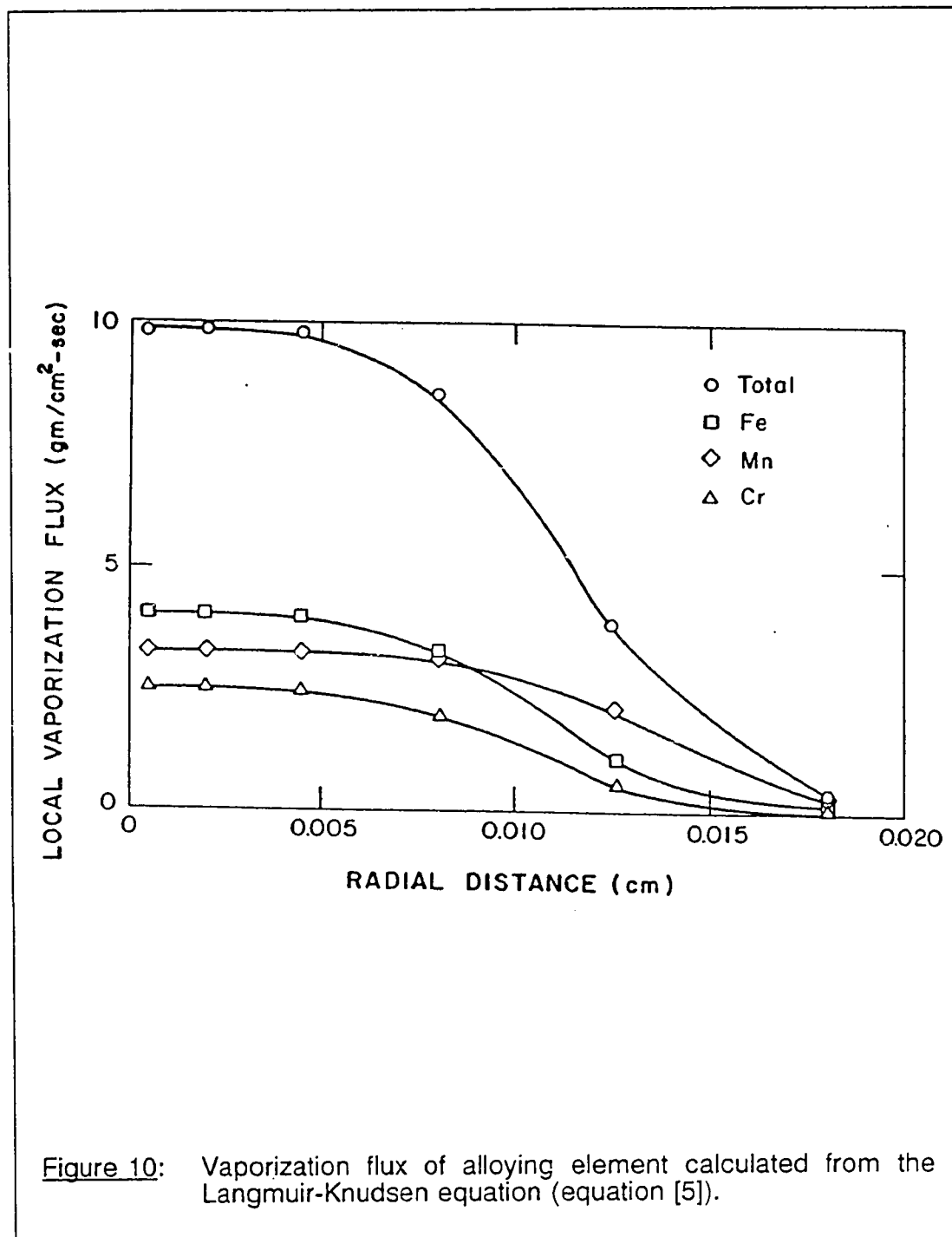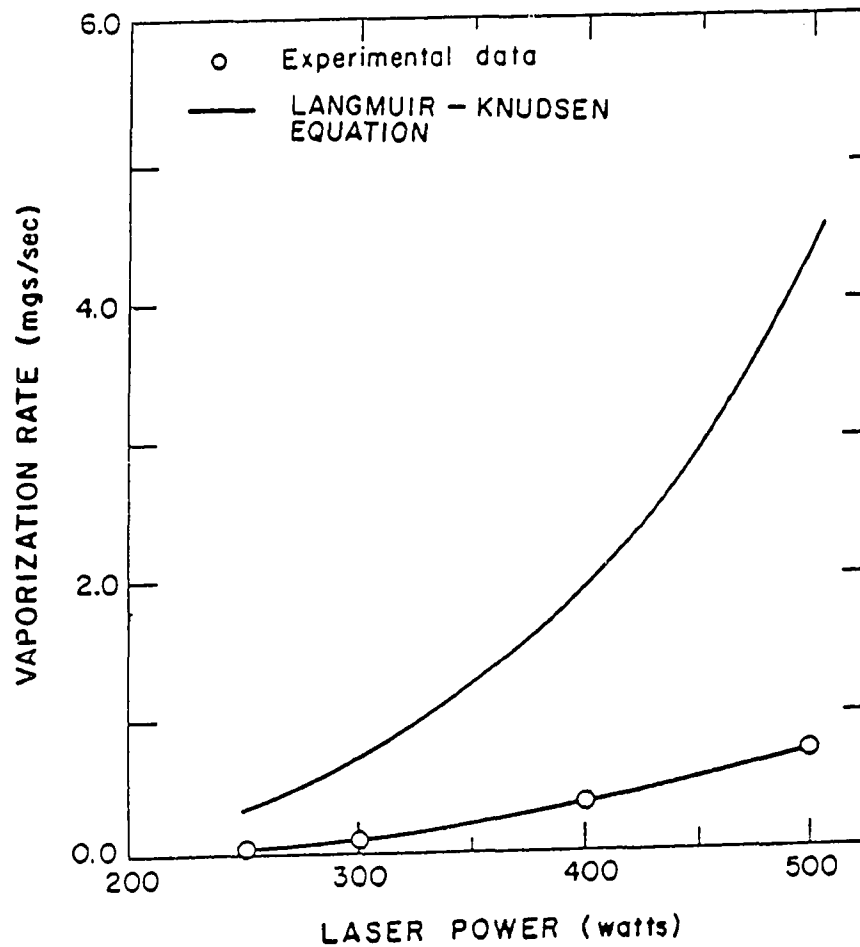
Figure 11: Comparison of experimental vaporization rates with the calculated vaporization rates using equation [6] at various laser powers. (Welding speed: 3.5 x 10⁻³ m/s, Shielding gas flow rate = 1x10⁻⁴ m³/s and Sample thickness: 7 x 10⁻⁴ m.).
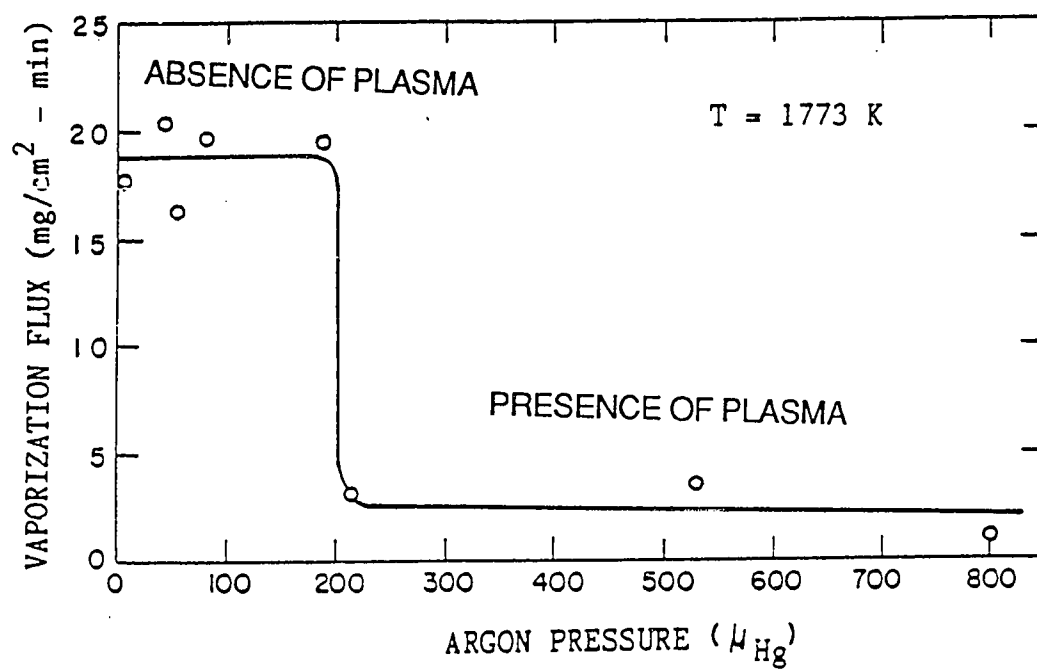
Figure 12: Vaporization flux of copper in the presence and absence of an argon plasma.
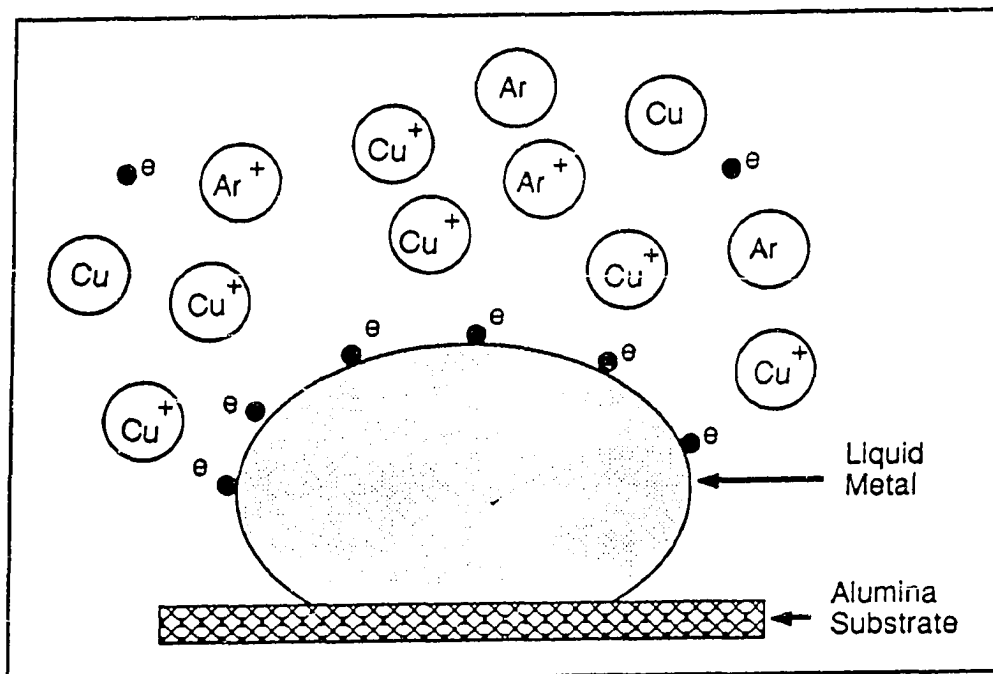
Figure 13: A schematic diagram of the space charge effect (from reference 88).

among the various charged species in the system, the region in close proximity of the copper surface is densely populated with positively charged copper and argon ions. Furthermore, the surface of the metal drop becomes negatively charged since the electrons strike the metal surface at a higher flux compared to that of ions (88). The attraction between the positively charged ions and the negatively charged droplets leads to higher condensation rates. The comparatively high condensation rate, in turn, results in the reduction of the vaporization rate when plasma is present. This phenomenon is important in understanding the fundamentals of alloying element vaporization in presence of plasma.

It should be noted that under the conditions of these experiments, the vaporization rate was indeed controlled by the intrinsic vaporization at the liquid surface and the decrease in the vaporization rate observed in Figure 12 is a true effect of the presence of plasma, and is not influenced by the effect of gas phase mass transfer. Since the molecular diffusivity is inversely proportional to pressure, the diffusivity of the copper vapors in the inert gas was enhanced by several orders of magnitude over the diffusivity at atmospheric pressure. This results in a significant increase in the gas phase mass transport rates. Figure 14 represents the variation of the vaporization rate as a function of pressure in the reaction chamber when either argon or helium was used as the atmosphere above the copper droplet at 1773K.

In all these experiments, the pressure was maintained sufficiently low to avoid the formation of plasma. It is clear that the vaporization rate is not a strong function of either the pressure or the type of gas used. These data confirm that the vaporization from the pure copper droplet was not controlled by mass

Figure 14: Variation of vaporization flux of copper as a function of chamber presssure in the absence of plasma under various gases.
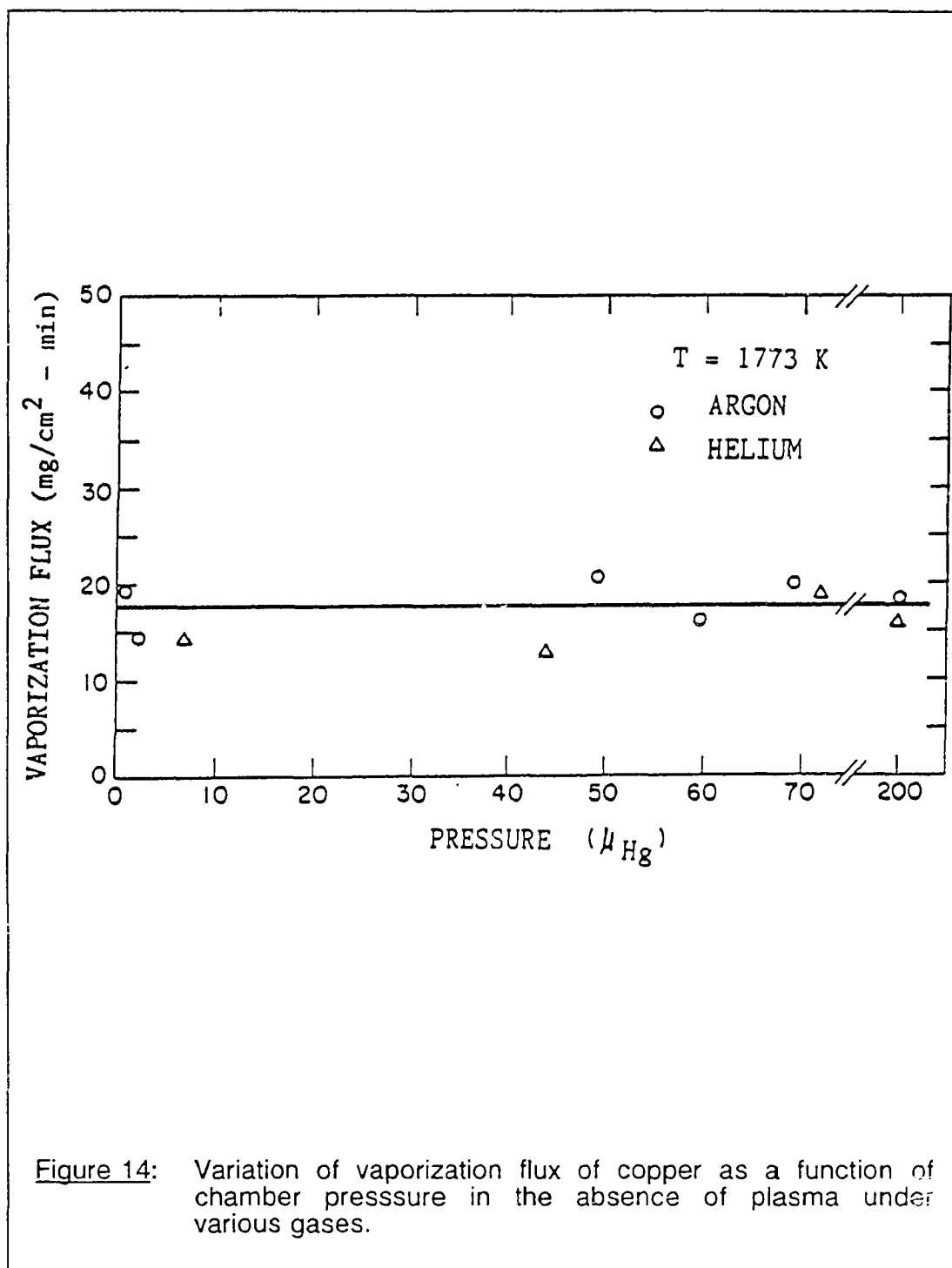
transfer in the gas phase and the rate was controlled by intrinsic vaporization at the surface.

4.1.4 Effect of process parameters on the vaporization rate of AISI 201 stainless steels

Figure 15(a) depicts the variation of vaporization rate as a function of laser power during laser welding of AISI 201 stainless steel samples. It is clear that there is an increase in the vaporization rate with rise in laser power. For an increase in laser power from 300 watts to 500 watts, there is a four fold increase in the vaporization rate. One of the main contributors to this increase is the threefold increase in the weld pool surface area (which can be calculated from the increase in the weld bead width from Figure 15(b).) with the increase in the laser power from 300 watts to 500 watts. Another factor which could contribute to the increased vaporization rate is the posssible increase in the weld pool temperature at higher laser power which could in turn lead to a significant increase in the vapor pressure. For example, in case of manganese, a 3 percent increase in weld pool temperature from about 3000 K can increase the vapor pressure by about 7 percent. The significant increase of the vapor pressure also in turn contributes to the higher vaporization rate according to equation [5].

The effect of welding speed on the vaporization rate was studied by measuring the vaporization rate at various welding speeds while maintaining a constant laser power. Figure 16(a) depicts this effect. It is observed that within the range of welding speeds studied, the vaporization rate does not change significantly. Figure 16(b) reveals that the weld bead width, and

Figure 15: Vaporization rate and weld bead width vs laser power for AISI 201 stainless steel. (Welding speed: 5×10^{-3} m/s, Sample thickness: 7×10^{-4} m and He shielding gas flow rate: 1×10^{-4} m^3/s)
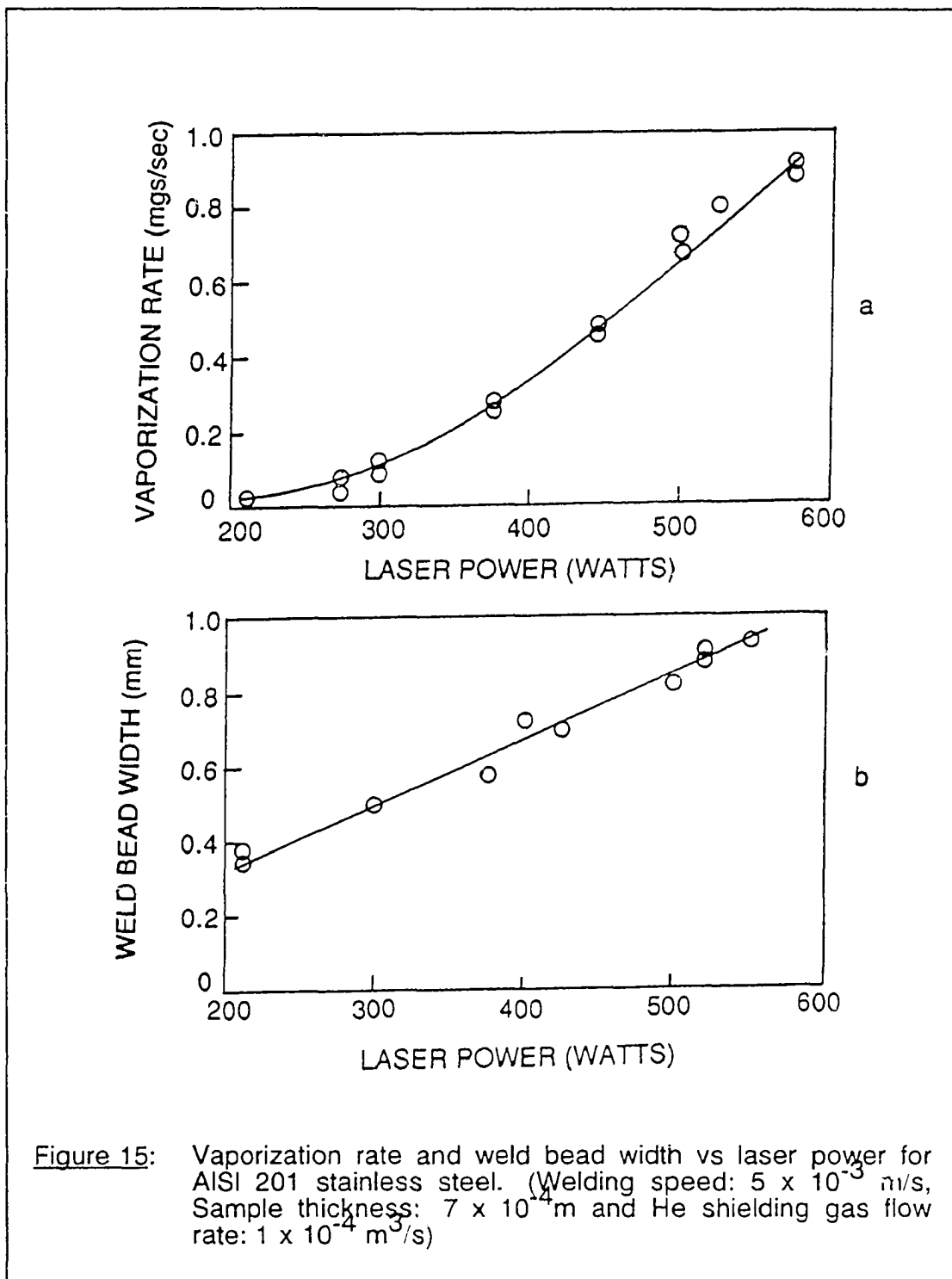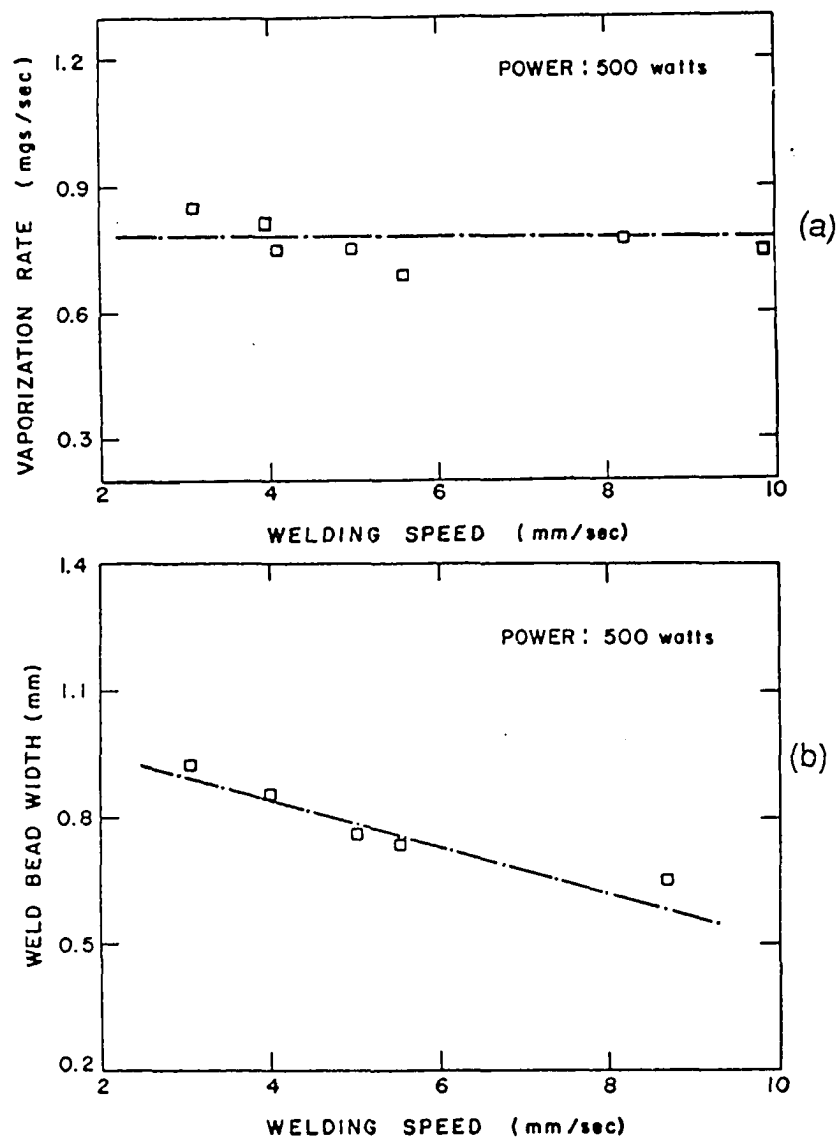
Figure 16: (a) Vaporization rate and (b) weld bead width vs welding speed for AISI 201 stainless steel. (Laser power: 500 watts, Sample thickness: 7×10^{-4} m and He shielding gas flow rate: 1×10^{-4} m^3/s.).

hence the surface area available for vaporization, decreases at higher welding speeds. This is because at higher welding speeds, there is a decreased amount of laser-solid interaction time which gives rise to decreased amount of overall weight loss of the sample. However, when one takes the ratio of the weight loss of the sample to the laser-solid interaction time which is represented by the vaporization rate, one notices that the ratio remains constant as the weight loss and the time, vary in a compensating fashion. Another factor which is responsible for the constant vaporization rate, even though the weld bead width decreases at higher welding speeds, is the fact that at higher speeds the volume of the molten zone could be higher due to increased undercooling effects. This higher volume of molten zone from which vaporization occurs could lead to the constant vaporization rate shown in Figure 16(a).

The weight loss measurements and the total laser-solid interaction time provide information about the overall vaporization rate. But in order to determine the vaporization rates of individual alloying elements, it is necessary to determine the composition of the vaporized materials collected on the inner surface of a quartz tube during laser welding experiments. The relative quantities of different elements obtained from the Atomic Absorption analysis of the vapor condensate are presented in Table 3. It is clear that iron, manganese and chromium are the most dominantly vaporizing materials. It will be shown subsequently that these compositions are also of paramount importance for the estimation of weld pool temperatures.

During the course of this study, EPMA data were also collected on the base metal and the weldment. In addition, the volume of the weld zone or the

Table 3: Relative quantities of various elements in the vapor deposit.

Laser power = 500 watts

Welding speed = 4×10^{-3} m/s

Helium flow rate = 1×10^{-4} m^3/s

Sample thickness = 7×10^{-4} m

n_{Fe}/n_{Mn}	n_{Cr}/n_{Mn}	n_{Ni}/n_{Mn}
1.29	0.49	0.044

solidified region was determined from the average area of cross section of the solidified zone and the length of the specimen. The composition of the different elements in the solidified region can be calculated from a knowledge of the overall vaporization rate, the composition of the vaporized material and the volume of the solidified region by simple mass balance. Table 4 shows the calculated change in the composition of the solidified region obtained by mass balances. It is clear that there is a considerable loss of manganese in the weld zone. However, the changes in composition of Ni, Cr and Fe when compared to the initial composition of these elements in the base metal are not very significant. Figure 17 shows the experimentally determined composition profile of Fe, Mn and Cr obtained from electron probe micro-analysis technique both in the base metal and the weld zone. It is clear that inspite of a small degree of scatter in the data, the concentration of manganese in the weld zone is lower than the corresponding concentration in the base metal by about 2.2 wt % which is in fair agreement with the calculated change in manganese concentration as reported in Table 4. The good agreement achieved between the calculated and the measured concentration of manganese demonstrates the consistency of the measured values of vaporization rate, composition of the vaporized material, dimensions of the solidified region and the concentration profile measurements utilizing the electron probe microanalysis technique.

4.1.5 Selective vaporization as an indicator of pool temperature

The local vaporization flux of different elements at low pressure can be calculated from equation [5] as indicated in earlier section. If one takes the

Table 4: Expected changes in the weld pool composition.

Volume of the molten zone $= 6.39 \times 10^{-8}$ m^3
Total weight loss $= 4.6 \times 10^{-5}$ Kg

Element	Concentration in wt %		
	Initial wt %	Expected wt %	Change (Δwt %)
Fe	72.27	74.55	+ 2.28
Mn	6.26	3.73	-2.53
Cr	16.15	16.04	- 0.11
Ni	4.41	4.67	+ 0.26
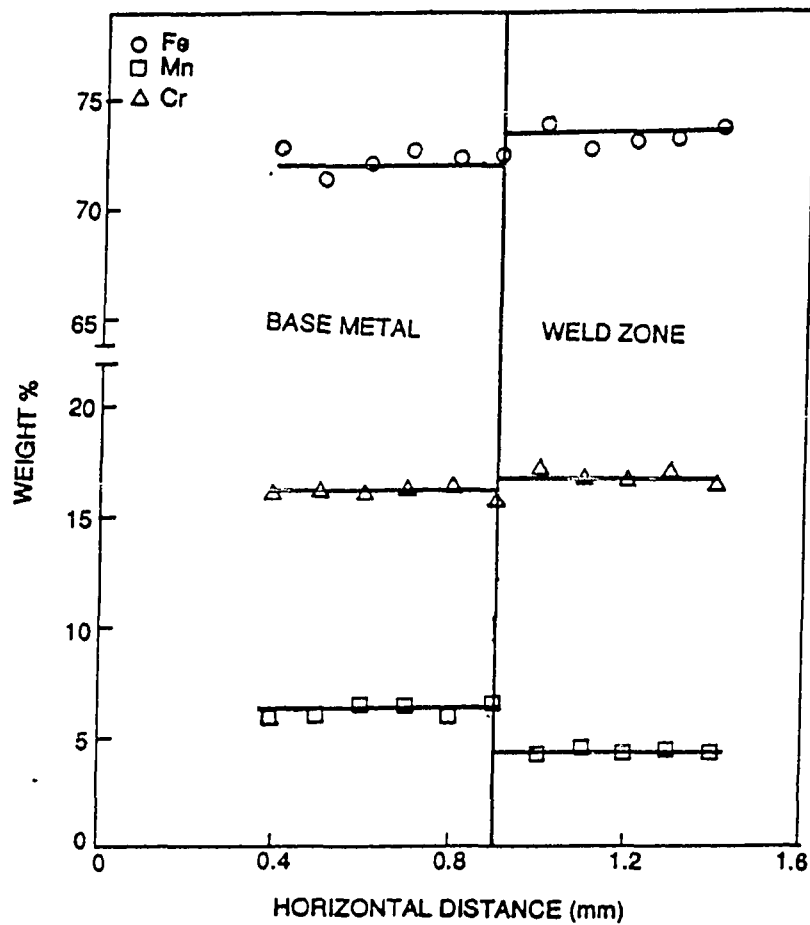
Figure 17:   Concentration profile of alloying elements in the weld zone and base metal. (Laser power: 500 watts, Welding speed: 5 x 10^{-3} m/s, Sample thickness: 7 x 10^{-3} m and He shielding gas flow rate: 1 x 10^{-4} m^3/s.).

ratio of vaporization fluxes of two pairs of elements i and j, the following equation is obtained:

$$J_i/J_j = (P_i/P_j)(M_j/M_i)^{0.5} \qquad [7]$$

The equilibrium partial pressure (P_i) of an element (i) over the molten pool depends upon the composition of the molten pool and the temperature. The partial pressure values of different elements can be calculated from the thermodynamic data available in the literature (see appendix A). The calculated values of the equilibrium partial pressures of different elements over liquid AISI 201 stainless steel assuming ideal solution behaviour at 2500 K and 3000 K are presented in Table 5. It is observed from the calculated values that the extent of variation of the equilibrium partial pressures resulting from the change in temperature is different for different elements. Since the vaporization rates of the individual elements are proportional to their respective equilibrium partial pressures, the ratio of the vaporization rates of any two elements can be a strong function of temperature. Alternatively, for a given composition of the molten pool, if the ratio of the vaporization rates of two elements is known, the pool temperature can be determined (26).

The calculated values of partial pressures were used in equation [7] to calculate the ratio of the vaporization rates of iron and manganese as a function of temperature. The calculated values of the ratio are plotted as a function of temperature in Figure 18(a). It is observed that the ratio of the rates is a strong function of temperature. If the experimentally determined value of J_{Fe}/J_{Mn}, presented in Table 3 on page 61 is utilized to determine the pool temperature from this figure, the temperature is found to be 3150 K.

Table 5: Partial pressure of the alloying elements over AISI 201 stainless steel (for reference see appendix A).

Element	Concentration	Temperature	
	wt %	2500 K (N/m^2)	3000 K (N/m^2)
Fe	70.89	2180	37236
Mn	7.15	150905	51448
Cr	16.34	1352	22689
Ni	4.87	74	1507
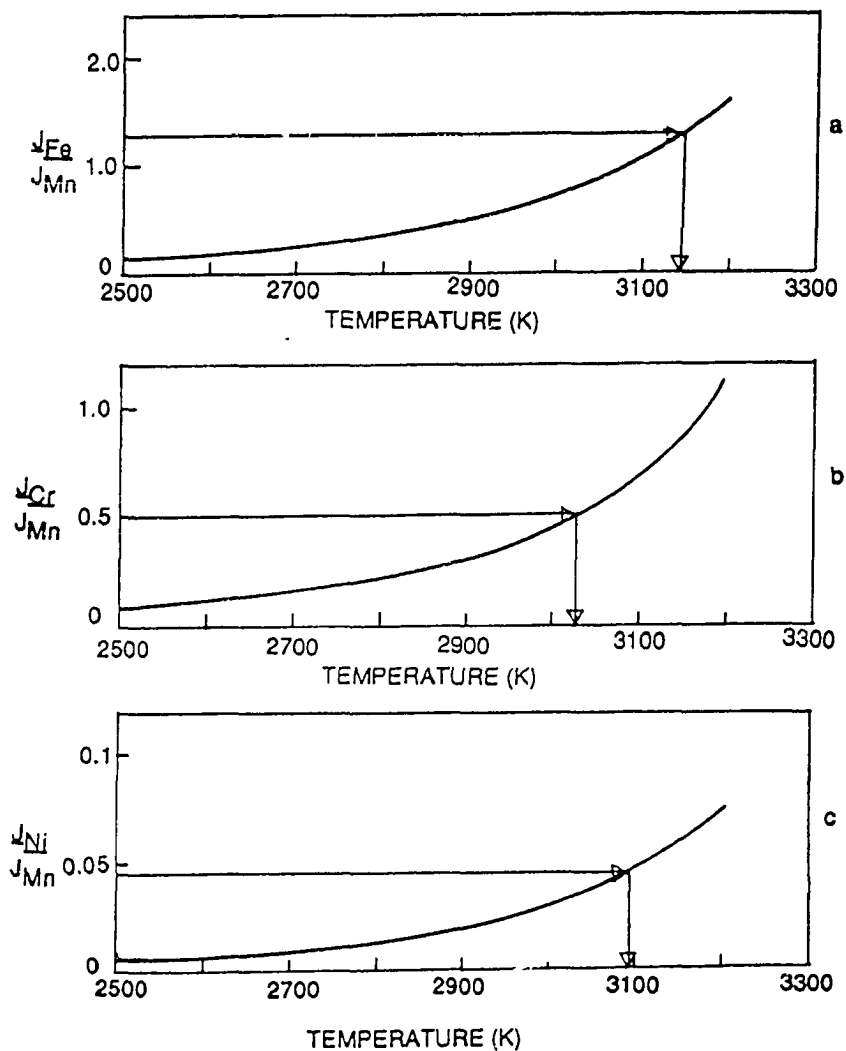
Figure 18:   The ratio of the calculated vaporization rates of (a) iron and manganese and (b) chromium and manganese and (c) nickel and manganese as a function of temperature.

Since there is a significant temperature gradient at the weld pool surface, the calculated temperature can be regarded as an effective vaporization temperature. Furthermore, since the vaporization rate increases strongly with the increase in temperature, the effective temperature may be expected to be close to the highest temperature value in the molten metal pool. This novel technique of weld pool temperature determination was demonstrated by Khan (26) for AISI 201 stainless steels and by Paul (27) for USS Tenelon stainless steels.

The computed flux ratio vs. temperature plot for chromium-manganese and nickel-manganese are in Figure 18(b) and Figure 18(c). Again, the measured values of the ratio of the rates of vaporization of different element pairs listed in Table 3 on page 61 were used for the calculation of pool temperature. The calculated values of pool temperature obtained from Figure 18(b) and Figure 18(c) were 3025 K and 3095 K for the flux ratios of the binary pairs Cr-Mn and Ni-Mn, respectively. These values are in fair agreement with the temperature calculated using the experimentally determined value of J_{Fe}/J_{Mn}. An interesting observation of these findings is that the selection of different element pairs leads to roughly similar values of the pool temperature. It is also to be noted that these experimentally determined weld pool temperatures are in good agreement with the temperatures predicted by Paul and DebRoy (89) in their mathematical model developed for conduction mode laser welding involving solutions of equations of change. They determined peak temperatues of about 3135 K on the weld pool surface. Since the vaporization rate increases strongly with the increase in temperature, the effective temperature determined from selective

vaporization technique may be expected to be close to the highest temperature value in the molten metal pool.

The equilibrium partial pressures of different elements needed for the construction of Figure 18 on page 67 were calculated assuming that the elements in the molten pool behave ideally. As the weld pool temperature is very high, it is anticipated that the ideal solution approach assumed for these calculations does not lead to significant inaccuracies. Khan and DebRoy (26) had determined the weld pool temperature using selective vaporization technique during laser welding of AISI 202 stainless steel. They found that the maximum error in the weld pool temperatures determined assuming ideal solution approach instead of non-ideal solution approach was about 3 %.

The effects of laser power and welding speed on the effective weld pool temperature determined by the above discussed techniques were determined. Figure 19(a) depicts the variation of the effective weld pool temperature as a function of the laser power.

It can be noted that there is a slight increase in the pool temperature with laser power. The welding speed does not have a significant effect on the weld pool temperature as shown in Figure 19(b).

4.2 Emission spectroscopic studies of the plasma

All studies involving plasma diagnostics were conducted with the laser being operated in the pulsed mode.
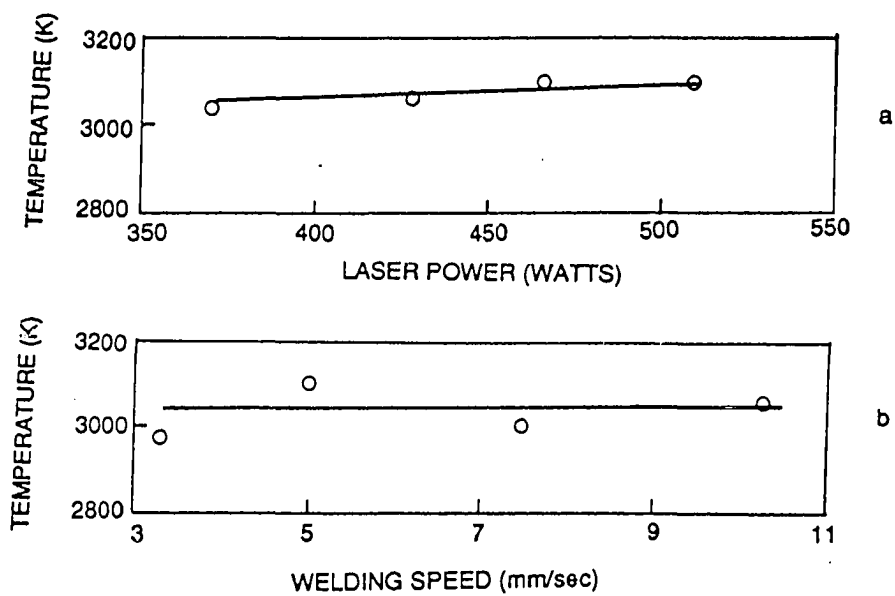
Figure 19: Effective weld pool temperature calculated on the basis of the ratio of the vaporization rates of a pair of alloying elements as a function of (a) laser power and (b) welding speed.

4.2.1 Typical spectrum

Figure 20 is a typical spectrum obtained from the plasma during laser welding of AISI 201 stainless steel. The intensity of each of the peaks (65), I_{qp}, is related to the number density of the species (ions or excited neutral atoms) in the upper energy level q, n_{aq}, the probability of transition from the upper energy level q to a lower energy level p, A_{qp}, the frequency of the emission, v, and the depth of the source, d, and is given by:

$$I_{qp} = d \, A_{qp} \, n_{aq} \, h \, v / (4\pi)$$ [8]

The number density of the species in the upper energy level q, n_{aq} is related to the number density of the species in the ground state by the Boltzmann equation:

$$n_{aq} = n_0 \, g_q \, (e^{(-E_q/kT)})/g_0$$ [9]

where n_0 is the number density of the species at the ground state, g_q is the degeneracy of the upper energy level, g_0 is the degeneracy of the ground state, E_q is the upper energy level, k is the Boltzmann constant and T is the absolute temperature. It follows from equations [8] and [9] that the intensity of emission at a particular frequency is dependent upon the number density of a species at the ground state, the depth of the plasma domain and the absolute temperature, the other terms in equations [8] and [9] being constant for a given frequency of emission. Therefore, the intensity of a peak is related to the concentration of the species at the ground state, which in turn is influenced by the vaporization rate of the species. Furthermore, the wavelength of emission from a given element is a character of both the upper

Figure 20: A typical spectrum of the plasma produced during laser welding of AISI 201 stainless steel. (He gas flow rate = 1.33 x10⁻⁵ m³/s, speed = 0.005 m/s, current = 35 mA, pulse length = 0.003 s, frequency = 100 Hz).
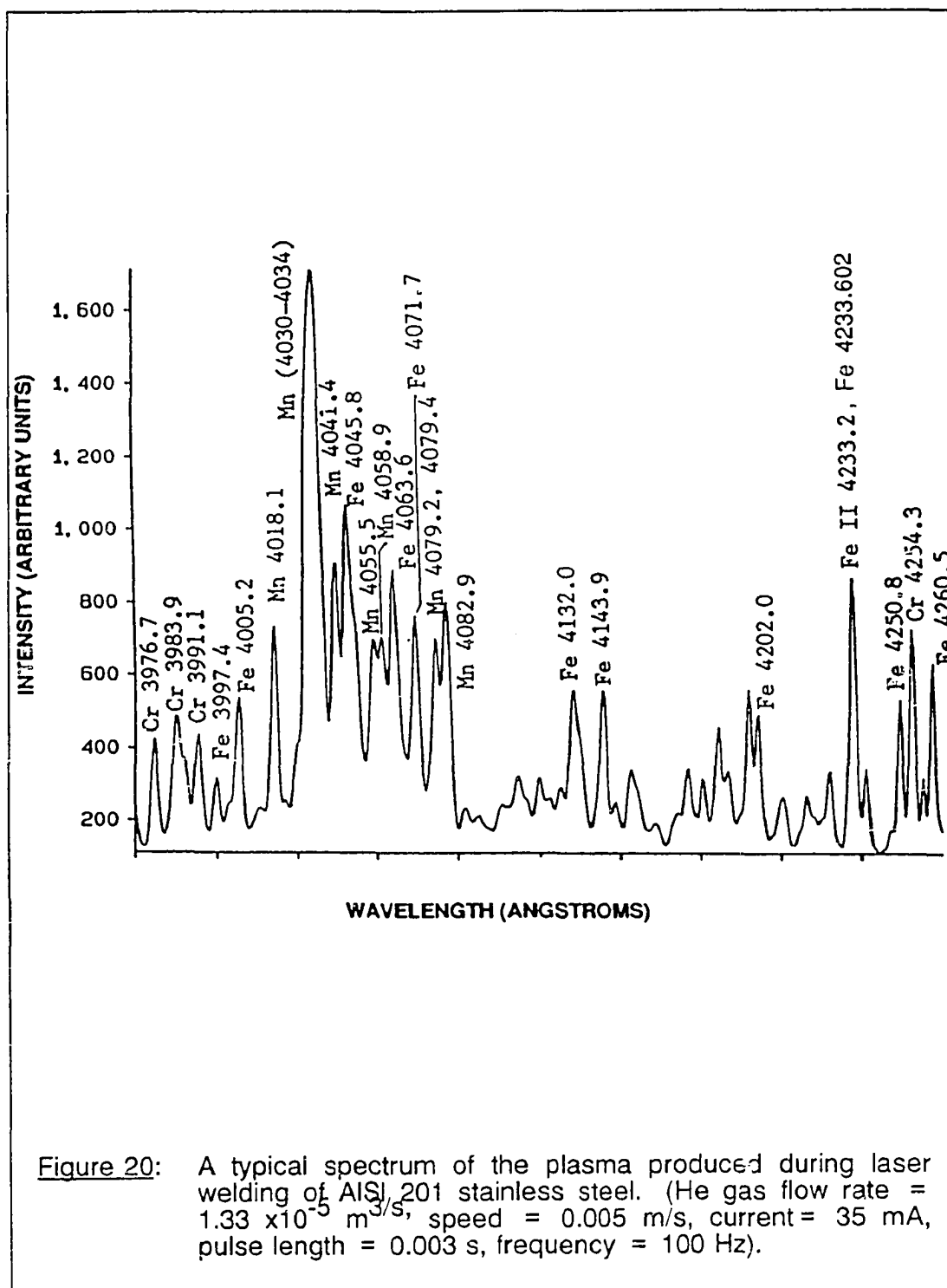
and the lower energy levels and indicates the state in which the species are present (excited neutral or ionized). From the spectrum in Figure 20 on page 72, iron, manganese and chromium were identified in the plasma primarily in their excited neutral states by comparing the wavelengths of various emissions with those given in standard tables (66). However, a peak corresponding to a singly ionized iron ion is observed at a wavelength of 4233.17 angstroms although overlapping with excited neutral emissions of iron in close proximity of this wavelength as indicated in the spectrum. In the wavelength range of the spectrum, this is the only known peak (66) corresponding to ionized state of iron. The first ionization potential for manganese and chromium is slightly lower than that for iron. However, in the wavelength range studied, no peak corresponding to ionized state of manganese exists. Although there is a peak corresponding to ionized chromium at a wavelength of 4012.7 angstroms, its intensity is rather "low" and the peak does not appear in the spectrum. Ionization of iron is documented in the literature (4) during spot welding of AISI 1018 steel in pulsed mode in the power density range similar to the present study. Furthermore, no peak corresponding to helium was detected. It should be noted that helium has a higher first ionization potential (24.5 ev) as compared to iron (7.9 ev), Cr (6.8 ev) or Mn (7.4 ev). The dominance of iron and manganese in the plasma is consistent with the composition of the vaporized species determined by vapor deposition technique shown in Table 3 on page 61. It is observed that iron and manganese were the most dominant metal vapors followed by chromium. Nickel was present at a very low concentration.

4.2.2 Laser energy

It was pointed out in the earlier section that the intensity of a peak at a particular wavelength is related to the number density of atoms in the ground state which in turn is influenced by the rate of vaporization of an alloying element during welding. The relation between the intensity of a peak and the rate of vaporization is demonstrated from the results of the experiments presented in Figure 21(a) and Figure 21(b). It is observed that the increase in the vaporization rate with the laser energy is accompanied by a concomitant increase in the intensities of several major peaks of iron, manganese and chromium. However, the correlation between the vaporization rate and the intensities of the peaks is only valid for a constant welding speed, shielding gas flow rate and composition as these parameters affect the amount of plasma present above the weld pool. Under the experimental conditions of the present study, the aspect ratio of the weld pool is closely related to the laser energy (Figure 21(c)) and to the intensity of the peaks (Figure 21(a)). These results indicate that under the conditions of the present study one can monitor the variation in the vaporization rates and the weld pool size from the changes in the intensities of the peaks in the spectrum. In other words, under a constant shielding gas composition, shielding gas flow rate and welding speed, sensors in the form of intensities have been developed to observe the changes in the vaporization rates and the weld pool size.

Figure 21: (a) Intensities of the major peaks of Cr, Mn and Fe (b) Vaporization rate and (c) Depth and Depth/Width ratio,as a function of laser energy. (Welding speed = 0.005 m/s, current = 35 mA, pulse length = 0.003 s, frequency = 100 Hz.)
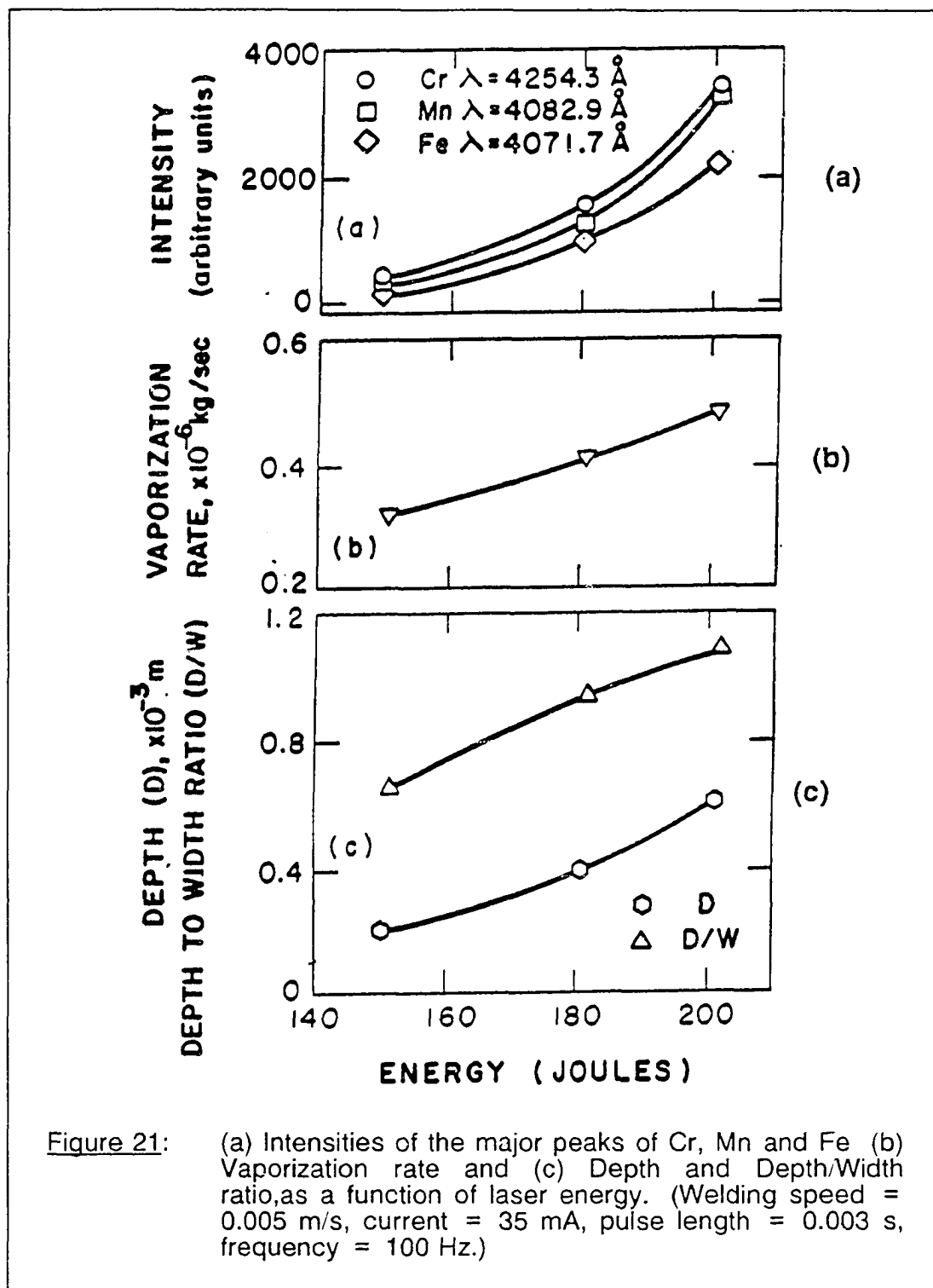
4.2.3 Welding speed

Figure 22(a) depicts the variation of the intensities of Mn, Fe and Cr peaks with the welding speed. The intensities of the peaks decrease at higher welding speeds due to a decreased heat input and a shorter beam interaction time resulting in a decrease in the amount of plasma formed. The slight decrease in the weld pool size at higher welding speeds as shown in Figure 22(b) is also due to a decrease in the beam interaction time. This indicates that the variation in the weld pool size can be detected from the changes in the intensities of the peaks as the two variables, viz., intensity and the weld pool size exhibit similar response to the changes in the welding speed under constant laser power, shielding gas flow rate and composition.

Figure 22(c) depicts the variation of the vaporization rate with the welding speed. The slight increase in the vaporization rate at higher welding speeds is because of the decreased amount of plasma present at these speeds leading to less of the laser beam being obstructed by the plasma.

4.2.4 Shielding gas flow rate

Figure 23(a) depicts the variation of the intensities of the major peaks with the change in the helium gas flow rate. The decreased intensities at higher flow rates could be attributed to relatively more plasma being blown away at high flow rates. Miller (90) determined that the electron temperature is not sensitive to the shielding gas flow rate, thus indicating that the slight variations in these intensities shown in Figure 23(a) could be due to the changes in n_0 (measure of vaporization rate) and d, the depth of source (equations [8] and
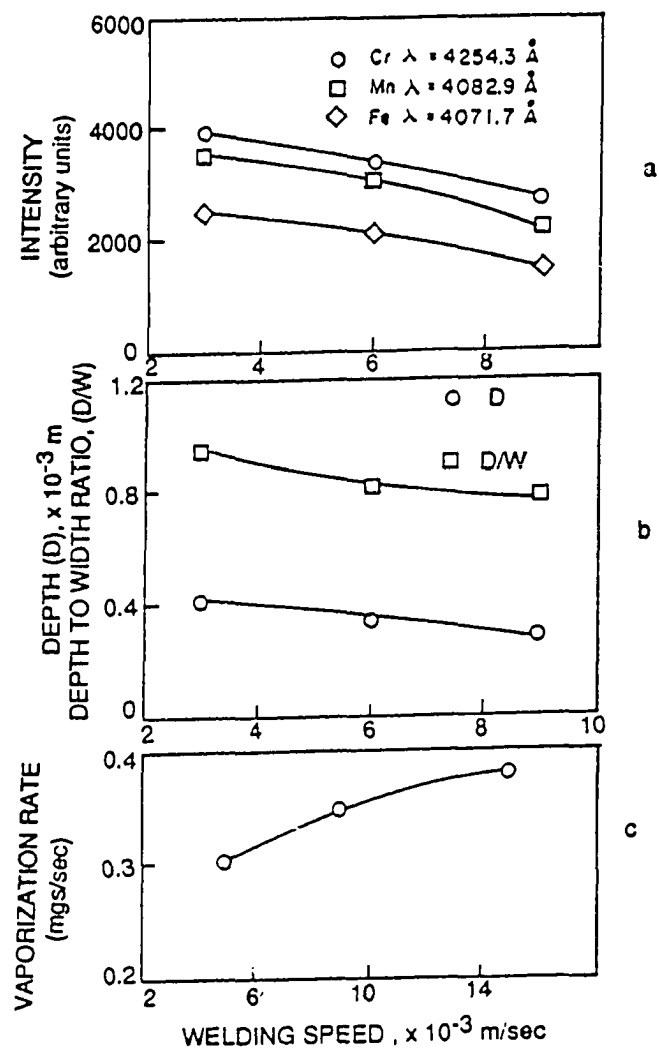
Figure 22:   (a) Intensities of the major peaks of Cr, Mn and Fe and
(b) Depth and Depth/Width Ratio and (c) Vaporization
rate as a   function of welding speed. (He gas flow rate
= 3.33 x 10^{-5} m^3/s, current = 35 mA, pulse length =
0.003 s, frequency = 100 Hz).

Figure 23: (a) Intensities of the major peaks of Cr, Mn and Fe (b) Depth, Width and Depth/Width Ratio and (c) Vaporization rate as a function of helium shielding gas flow rate. (welding speed = 5 x 10^{-3} m/s, current = 35 mA, pulse length = 0.003 s, frequency = 100 Hz).
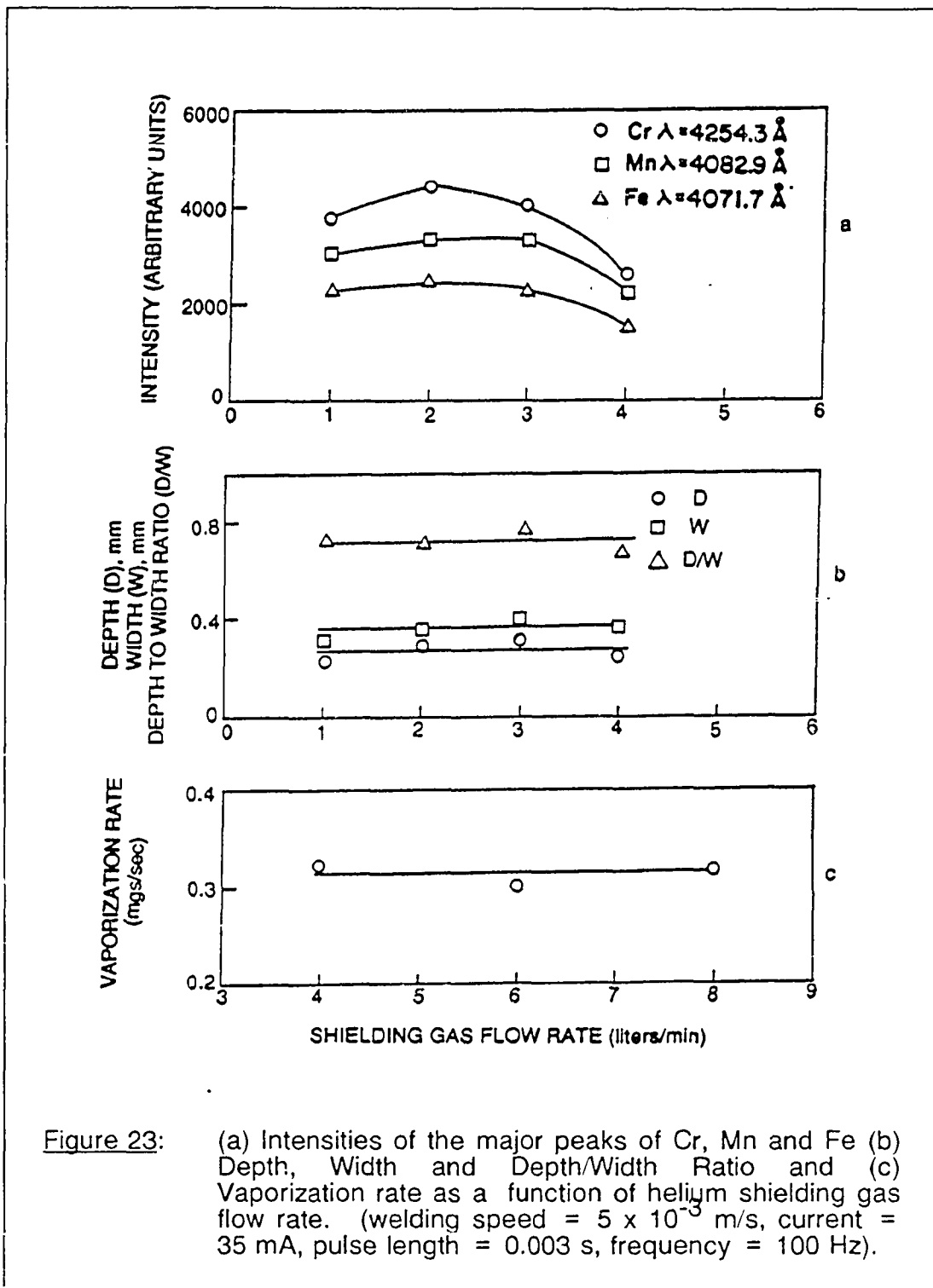
[9]) and not the electron temperature. However, the depth, width and the depth/width ratio are not very much affected by the gas flow rates as shown in Figure 23(b). From Figure 23(c) which depicts the vaporization rate as a function of gas flow rate, the vaporization rate is found to be insensitive to gas flow rate indicating that the changes in the intensities at higher flow rates are not significant enough to affect the laser-solid interaction.

4.2.5   Shielding gas composition

Figure 24(a) depicts the variation of the intensities of Mn, Fe and Cr peaks with the shielding gas composition. It is clear that the intensities of the peaks decrease with the increase in the concentration of helium in the shielding gas. Miller (90) determined that the electron temperature is insensitive to variations in the shielding gas composition from his emission spectroscopic studies during pulsed laser welding of AISI 201 stainless steels. Therefore, the increased intensities observed when argon was used as a shielding gas could be attributed to an increase in d, the depth of source and not the electron temperature (equations [8] and [9]). The increased depth of source in case of argon is because argon has a lower thermal conductivity than helium which, in turn, leads to increased heat retention in case of argon. This, in turn, leads to the formation of more plasma and, hence, higher intensities of the emissions from the species present in the plasma.

In order to examine the relation between the amount of plasma and the weld pool shape, the depth, width and the depth/width ratio were plotted as a function of the shielding gas composition in Figure 24(b). The beneficial effect of helium in the shielding gas is clearly observed from this figure. The
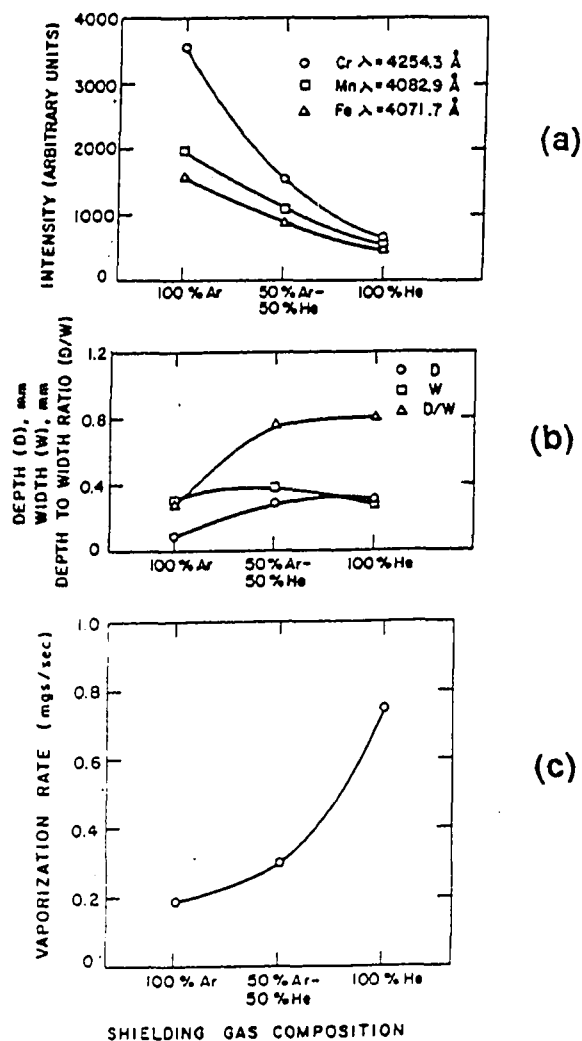
Figure 24:   (a) Intensities of the major peaks of Cr, Mn and Fe (b) Depth, Width and Depth/Width Ratio and (c) Vaporization rate as a function of the shielding gas composition. (Gas flow rate = 3.33 x 10⁻⁵ m³/s, current = 35 mA, welding speed = 0.005 m/s, pulse length = 0.003 s, frequency = 100 Hz).

increased penetration is due to a decrease in the amount of plasma. This is consistent with the decreased obstruction of the laser beam by the plasma. Although the weld bead width does not change significantly with the change in the shielding gas composition, the depth of penetration is found to be higher in case of helium as compared to argon. Higher weld penetration observed in helium is consistent with the increased vaporization rate as depicted in Figure 24(c). Furthermore, it is interesting to note that although the vaporization rate is lower in case of argon, relatively more of the vaporized species get excited leading to increased intensity of the peaks when argon is used for shielding purposes. Therefore, although n_O in equation [9] which is a measure of the vaporization rate is lower in case of argon, the increase in the depth of source more than compensates for the decrease in n_O, resulting in a net increase in the intensities (Figure 24(a)).

4.2.6   Plasma temperature determination by the slope method

An average plasma or electron temperature can be determined from a given spectrum by a technique well documented in most books on plasma diagnostics (65) and used recently by Knudston et al. (20) for laser produced aluminum plasmas. The following equation (20,67) was used to determine an average plasma temperature:

$$\ln\left[\frac{\varepsilon_{qp}}{g_q A_{qp} v}\right] = \ln(N/Z) - E_q/kT \qquad [10]$$

where, v is the frequency, E_q and g_q are the energy and the degeneracy of the upper energy level, respectively, A_{qp} is the transition probability, k is the Boltzmann constant, T is the absolute temperature, ε_{qp} is the intensity (area

under each peak), N is the total number density and Z is the partition function. The values of g_q, A_{qp} and E_q at various wavelengths of iron peaks were taken from the work of Fuhr et al. (68). The slope of the left handside of equation (10) versus the upper energy level E_q is a measure of the plasma temperature.

One of the main assumptions for utilizing the above equation is the existence of local thermal equilibrium (LTE). A gaseous system in complete thermal equilibrium is characterized by the following conditions (65):

1) The velocity distribution of all kinds of free particles (molecules, atoms, ions and electrons) in all energy levels satisfy Maxwell's equation.

2) For each separate kind of particle, the relative population of energy levels conform to Boltzmann's distribution law.

3) Ionization of atoms, molecules and radicals is described with Saha's equation and dissociation of molecules and radicals with the general equation for chemical equilibria.

4) Radiation density is consistent with Planck's law.

In a non-homogeneous source such as a laser-produced plasma, it has become customary to consider each element of volume separately and to denote the equilibrium conditions as local thermal equilibrium (LTE).

Figure 25 depicts the spectrum obtained from the plasma produced during laser welding of ultrapure iron samples. This spectrum was collected by placing the monochromator slit vertical, i.e., parallel to the laser beam impingement axis. Figure 26 represents a plot of left hand side of equation [10] versus inverse of temperature for the spectrum obtained from the pure iron sample (from Figure 25) and the slope of the line was obtained from

Figure 25: A typical spectrum of the plasma produced during laser welding of ultrapure iron sample. (He gas flow rate = 3.33 x 10⁻⁶ m³/s, welding speed = 0.005 m/s, current = 35 mA, pulse length = 0.003 s, frequency = 100 Hz.)
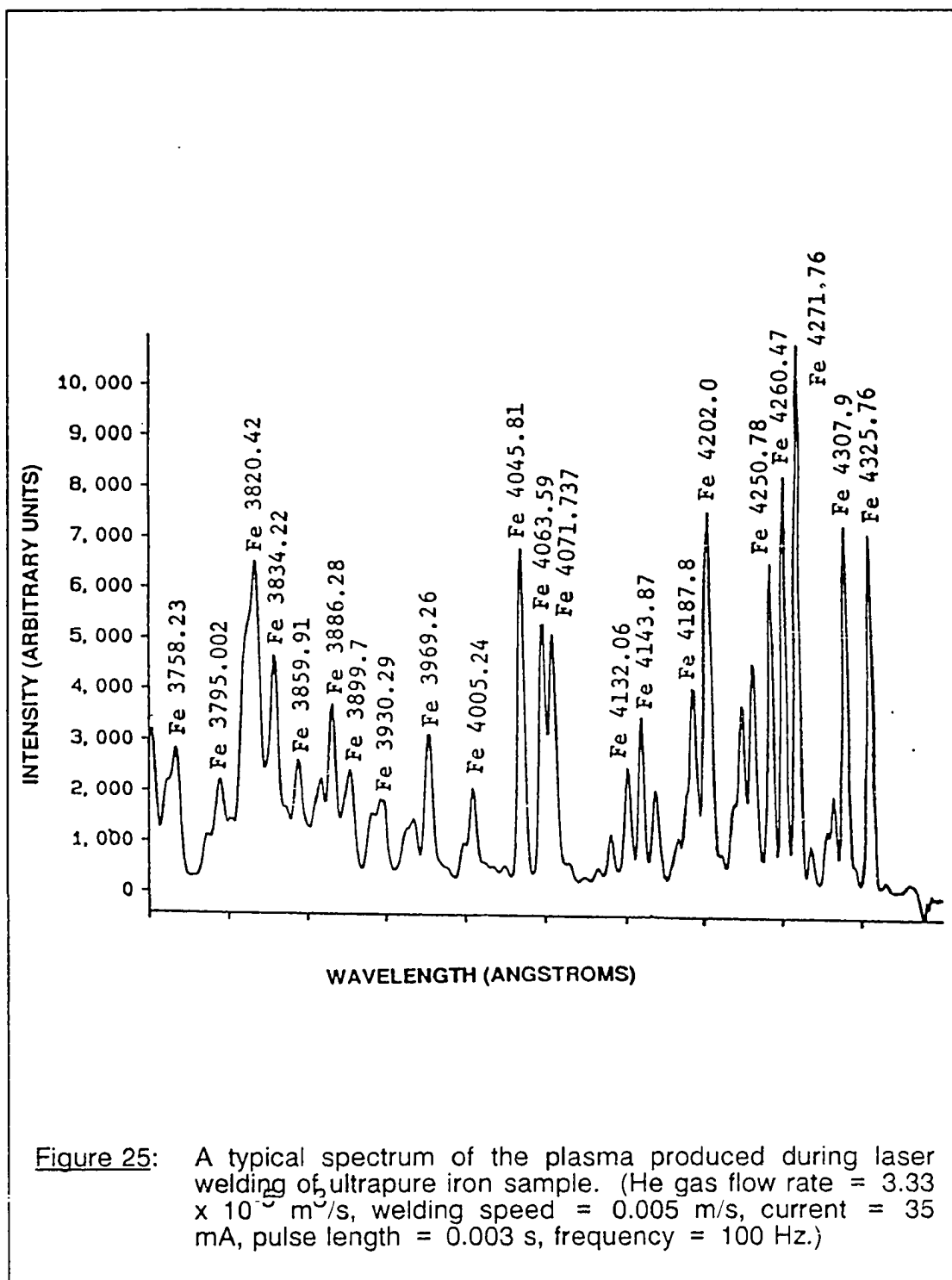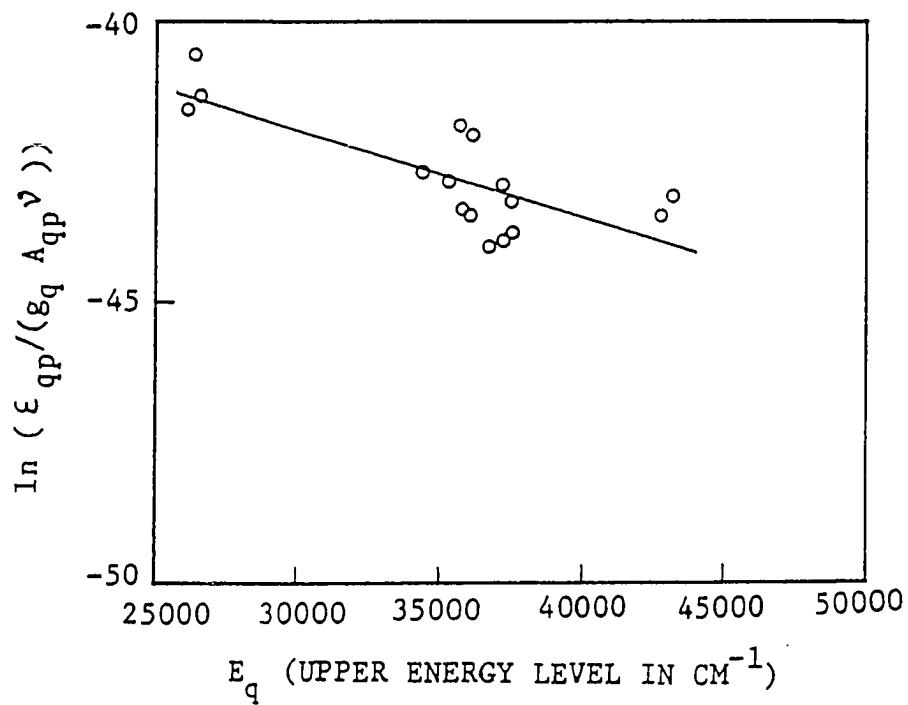
Figure 26: A plot of left-hand side of equation [10] versus the upper energy level E_q used for determination of the plasma temperature.

linear regression of sixteen data points. It was found that the plasma temperature corresponding to the spectrum of Figure 25 on page 83 was 9400 K. Some of the wavelengths of iron peaks in Figure 25 on page 83 were neglected on the basis of interferences from two peaks in close proximity with each other. The average axial temperature for iron samples which were oxidized and for the samples that were doped with sulfur or oxygen was determined to be roughly 8,000 K (Table 6).

The error in the temperature values indicated in Table 6 arise from the uncertainties in the tabulated values of transition probabilities (68) and also due to self-absorption effects and are discussed in appendix B. Self-absorption (65) occurs when radiation generated in the interior of a source is subject to absorption on its passage to the outside. The absorption occurs by atoms of the same kind as those causing the emission. In the iron plasma investigated in this study, self-absorption effects are significant. These effects could also contribute to the non-linearity of the Boltzmann plot (Figure 26) and the errors in the temperature values due to the non-linearity are discussed in appendix B. Self-absorption effects are normally known to increase the temperature of the plasma (87). Therefore it is more likely that the actual temperature of the plasma might be closer to the lower end of the range of temperatures indicated in Table 6 for each of the systems.

4.2.7   Plasma temperature determination by the two line method

This technique used for the determination of radial plasma temperature distribution (92) involves identification of two suitable wavelengths of a single thermometric element in the plasma. Several restrictions must be satifisfied

Table 6: Electron temperatures during laser welding of various samples. (Helium flow rate = 3.33 x 10^{-5} m^3/s, welding speed 0.005 m/s, current = 35 mA, pulse length = 0.003 s, frequency = 100 Hz.)

System	Temperature (K)
Fe	9406^{+3870}_{-2159}
Fe-S	7995^{+2826}_{-1655}
Fe-O	8040^{+2882}_{-1678}
FeO	7995^{+2844}_{-1661}

for the reliable determination of the plasma temperature distribution. These include a requirement (65) of close proximity of the wavelengths of the two peaks selected, and a significant difference in the upper energy levels of these emissions (at least of the order of kT). These and other necessary criteria (65) were satisfied by the two manganese peaks corresponding to wavelengths 5377.00 and 5341.06 angstroms, respectively. These two peaks have been used by Mills (17,18) for the determination of arc temperatures during GTA welding of high manganese stainless steels. The intensities of these two peaks were determined experimentally at different lateral regions of the plasma at a mid height horizontal plane by placing the monochromator slit horizontal. The experimentally observed intensities along the line of sight were then averaged and reduced to ten data points by taking the average of two intensities symmetric about the center. These values are plotted in Figure 27 for both the manganese peaks which were monitored. The experimental intensities at the center for both the manganese peaks are lower at the center due to the self-absorption effects wherein the emissions from the center get absorbed on their way out of the plasma, leading to a lowering of the intensities.

It is important to realize that these intensities measured experimentally are the integrated intensities measured along the line of sight or the direction of observation (Figure 28) and are denoted mathematically as follows:

$$I(y) = 2 \int_{y}^{R} \frac{J(r) \, r \, dr}{(r^2 - y^2)^{1/2}}$$

[11]
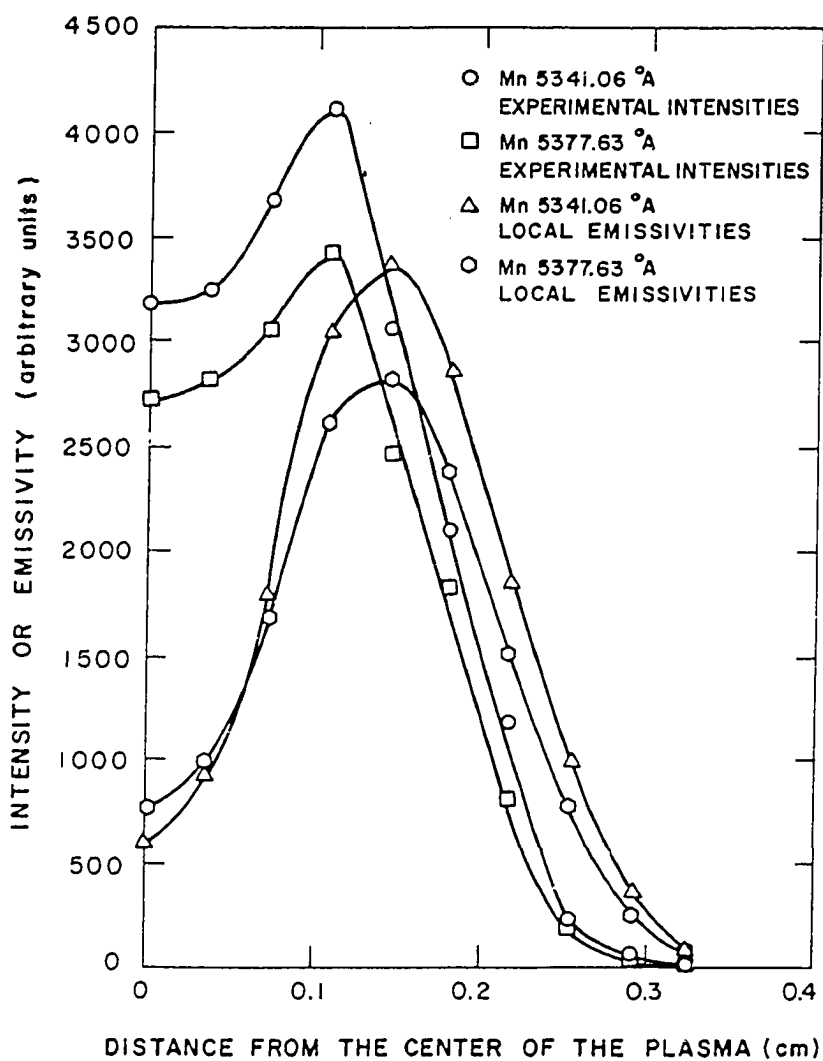
Figure 27: Plot of the experimental intensities and the local emissivities at various radial locations for the two manganese peaks at 5377.63 and 5341.06 angstroms. (He gas flow rate = 3.33 x 10⁻⁵ m³/s, welding speed = 0.005 m/s, current = 35 mA, pulse length = 0.003 s, frequency = 100 Hz).
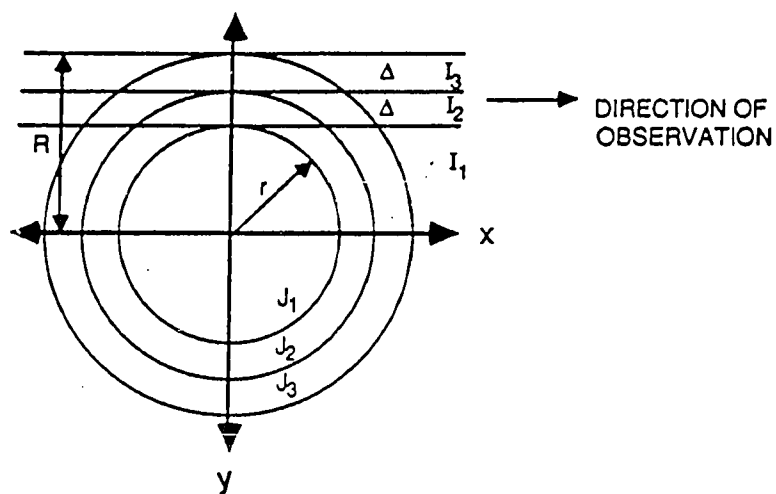
Figure 28: A schematic of the geometric relations existing between the integrated line of sight intensities, I(y) and the radial local emissivities J(r).

where I(y) is the integrated experimental intensity at distance y from the center of the plasma, J(r) is the local emissivity at distance r from the center of the plasma.

However, for temperature measurements utilizing this method, one needs the local emissivities which can be calculated by inverting or deconvoluting the experimental integrated intensities by a procedure known as Abel transformation (69) which gives rise to the following expression:

$$J(r) = -\frac{1}{\pi} \int_r^R \frac{I'(y) \, dy}{(y^2 - r^2)^{1/2}} \qquad [12]$$

The Abel transformation yields the local emissivities [J(r)] from the observed integral intensities by a deconvolution scheme. The transformation was carried out by a numerical scheme based on Barr's technique (69) with the help of a computer program given in Appendix C. The computed local emissivities are plotted in Figure 27 on page 88 for both the manganese peaks. The trend of these plots for the experimentally observed intensities and the inverted emissivities is similar to that observed by Olsen (70) in his studies on argon plasma. The values of local emissivities of the two manganese peaks at each radial location were used for the determination of the radial distribution of the plasma temperature. The plasma was assumed to be optically thin. It will be demonstrated subsequently that this assumption is reasonable in view of the weak nature of the plasma. The following equation was used for the calculation of radial distribution of electron temperature assuming local thermodynamic equilibrium:

$$T = \frac{5040 \, (V_a - V_b)}{\log\left[\frac{(gA)_a}{(gA)_b}\right] - \log\left[\frac{\lambda_a}{\lambda_b}\right] - \log\left[\frac{J_a}{J_b}\right]} \qquad [13]$$

where V is the excitation potential in eV, A is the transition probability, g is the statistical weight or the degeneracy, is the wavelength, J is the local emissivity, and the subscripts a and b refer to Mn peaks at Mn 5377.63 and 5341.06°A wavelengths. The data used for the calculations (71) are presented in Table 7. Figure 29 depicts the computed plasma temperature distribution as a function of radial distance.

The distance between the lens and the monochromator slit was adjusted to accommodate the entire image of the plasma on the slit and the two regions near the boundaries of the plasma were matched with the first and the last track of the sensitized region of the detector. The width of the plasma domain was then determined from the dimension of the sensitized region of the detector and the magnification due to the convex lens and was found to be about 0.65 cm. It is observed that the plasma temperature varies from about 8,100 K at the center to about 6,500 K at the periphery. The possible errors in the temperature values are fairly large and are discussed in Appendix B. Another source of error in the temperature values could be attributed to the self-absorption effects which, through their influence on the intensities, indirectly affect the temperatures determined from these intensities. The temperatures obtained from this analysis are within the range of plasma temperatures calculated theoretically by Pirri et al. (72) who found that the laser plasmas typically reach temperatures of 5000 to 20000 K. Rockstroh and Mazumder (19) determined peak temperatures of about 17,000 K and about 10,000 K near the end of their plasma core for their laser produced aluminum-argon plasmas. The relatively high electron temperatures

Table 7: Data used for the calculation of the plasma temperature distribution using equation [13] (from reference 71).

Wavelength of the peak. (^{o} A)	Transition probability ($\times 10^8$ s^{-1})	Statistical weight	Upper excitation potential (eV)	Subscript
5377.63	0.42	4	6.148	a
5341.06	0.014	8	4.435	b
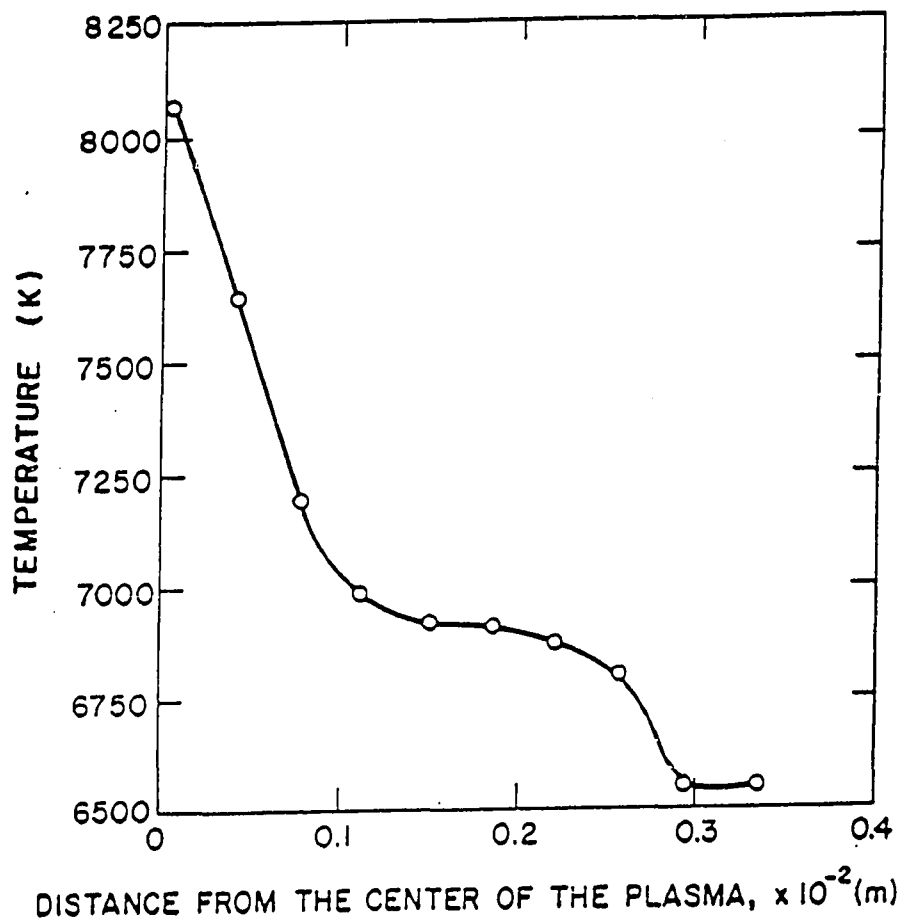
Figure 29:   Plasma temperature distribution as a function of radial distance obtained from the local emissivities after Abel inversion. (He gas flow rate = 3.33 x 10⁻⁵ m³/s, welding speed = 0.005 m/s, current = 35 mA, pulse length = 0.003 s, frequency = 100 Hz).

are consistent with the use of high laser power in the kilowatt range used in their study.

4.2.8 Number density of electrons in the plasma

A formalism used by Dunn and Eagar (73) was adopted for the calculation of the number density of electrons in the plasma. For a reaction of an atom forming an ion and an electron, i.e., Atom = Ion + Electron, the number densities of ions, electrons and neutral atoms are given by Saha's equation (74):

$$\frac{n_e \, n_i}{n_a} = \frac{Z_e \, Z_i \, (2\pi m_e kT)^{3/2} \, e^{(-V/kT)}}{Z_a \, h^3}$$

[14]

where n_e, n_i and n_a are particle number densities of electrons, ions and neutral atoms respectively, T is the absolute temperature, V is the ionization potential, m_e is the rest mass of electrons, k is the Boltzmann's constant and h is the Planck's constant. In equation [14], the internal partition functions, Z_e, Z_i and Z_a are given by:

$$Z = \sum_j g_j \, e^{-u_j/kT}$$

[15]

where g_i is the degeneracy or statistical weight corresponding to the energy level u_i. For a monatomic gas

$$g = 2S + 1$$

[16]

where S is the vector sum of the spin numbers. The partition functions were calculated from the data given in NBS tables of atomic energy levels compiled by Moore (75). The details of the calculation scheme used for the determination of partition functions of manganese, iron and chromium are given in appendix D. The partition functions for helium in its atomic and ionic states are 1 and 2, respectively (75). The degeneracy of electrons was taken as equal to 2. The number densities of the ions, electrons and atoms were obtained by solving equation [14] along with equations [17] and [18] which represent the equations of quasi-neutrality of charge and the ideal gas behavior respectively. Furthermore, kinetic equilibrium ($T_e = T_i = T_a = T$) was assumed for the calculation scheme.

$$n_e = n_i \qquad\qquad [17]$$

$$n_e + n_i + n_a = 7.34 \times 10^{27}/T \qquad\qquad [18]$$

The number densities of ions or electrons of the pure species, viz., Fe, Cr, Mn and He present in the plasma were calculated at various temperatures. A computer program which was developed for performing these calculations is presented in Appendix C. The results from this program are presented in Figure 30 which demonstrates the variation of number densities of as a function of temperature. The number density of electrons in pure chromium plasma is the maximum because chromium has the lowest ionization potential when compared to iron, manganese and helium.

The total electron density n_e in the plasma produced during laser welding of AISI 201 stainless steel can be determined by multiplying the individual electron densities of Fe, Mn, Cr and He with their respective mole
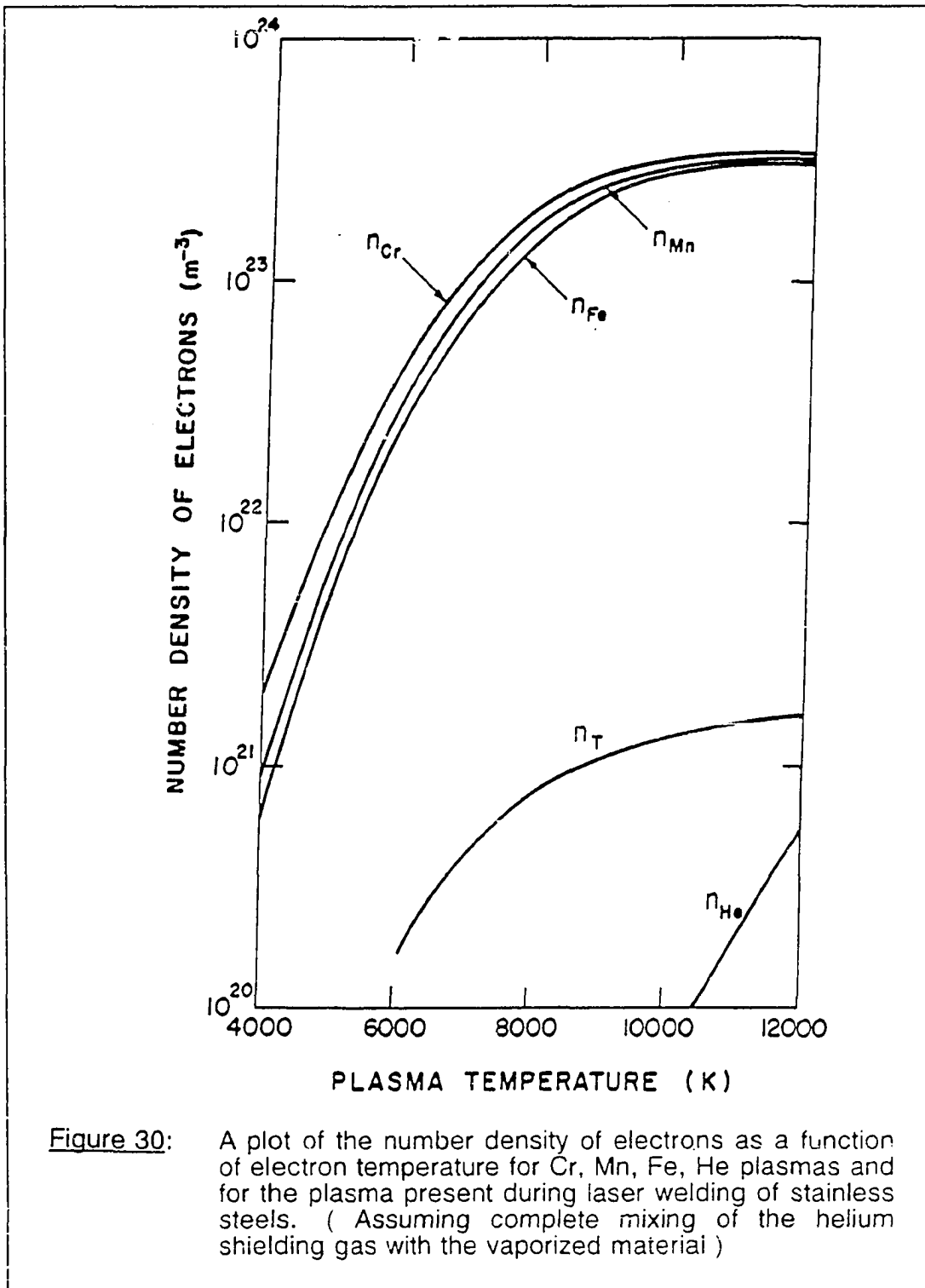
Figure 30: A plot of the number density of electrons as a function of electron temperature for Cr, Mn, Fe, He plasmas and for the plasma present during laser welding of stainless steels. (Assuming complete mixing of the helium shielding gas with the vaporized material)

fractions and summing up the individual weighted electron density values and is given by the following equation:

$$n_e^{Total} = n_e^{Mn} C_{Mn} + n_e^{Fe} C_{Fe} + n_e^{Cr} C_{Cr} + n_e^{He} C_{He} \qquad [19]$$

As a first approximation, complete mixing of the shielding gas with the vaporized material was assumed to determine the composition of the various species in the domain of calculation. This assumption will be relaxed later on in this study wherein the concentration profile of the species, viz., Mn, Fe and Cr will be determined. The calculated values of the mole fraction of the various species used for the computation are presented in Table 8.

A plot of the number density of electrons in the plasma as a function of electron temperature is presented in Figure 30 on page 96. From the average plasma temperature of about 7,000 K, the total number density of electrons and the total number density of atoms in the plasma were determined to be about $4.4 \times 10^{20}/m^3$ and $1.05 \times 10^{24}/m^3$, respectively. The proportion of ionized species at 7,000 K expressed as a percentage of the total number density of all species was found to be about 0.042 %. The low value of ionization is consistent with the dominance of excited neutral atoms in the plasma (Figure 20 on page 72). This indicates that the plasma is fairly weak and the assumption of an optically thin plasma is justified.

4.2.9 Calculation of the absorption of the laser beam

In this section, first the experimental results pertaining to the three dimensional distribution of electron temperature in the plasma will be discussed. The three-dimensional temperature profile determination includes

Table 8: Plasma composition used for the calculation of number density.

Vaporization rate = 0.35×10^{-6} Kg/s

Helium gas flow rate (at 298 K and 1 atm.) = 3.33×10^{-5} m^3/s

J_{Fe}/J_{Mn} (Molar ratio) = 1.16

J_{Cr}/J_{Mn} (Molar ratio) = 0.30

Element	Mole %
Fe	0.2011
Mn	0.1733
Cr	0.0512
He	99.574

acquisition of spectral data over the whole domain of the plasma which in turn will provide electron temperature data in both radial and axial locations of the plasma. The number density of electrons in the plasma corresponding to pure plasmas can be determined from the electron temperatures. In order to determine the actual number density of electrons in the plasma, a knowledge of velocity profiles and in turn, concentration profiles is necessary. From the number density of electrons corresponding to pure plasmas and the concentration profiles of each of the species present in the plasma, the actual number density of electrons contributed from all the species viz., Mn, Fe, Cr and He can be calculated using equation [19] presented in the preceeding section. The temperature and the actual number density data together can be utilized to determine the absorption coefficient of the laser beam by the plasma.

The temperature profile at each horizontal location of the plasma was obtained by first collecting the intensities of two manganese peaks, viz., 5341.06 $^{\circ}$A and 5377.63 $^{\circ}$A in a multi-track and a multi-scan operation mode of the optical multichannel analyzer (OMA 3). The multi-scan mode was used with data collection over eight scans in order to obtain a time-averaged reading of the intensities as the intensity of the plasma produced during pulsed laser welding (due to the on-time and the off-time present during pulsing) is time dependent. Typical multi-track and multi-scan data are shown in Figure 31. The peaks marked as A and B in the figure correspond to the Mn 5341.06 $^{\circ}$A and Mn 5377.63 $^{\circ}$A, respectively. One can obtain the two boundaries of the plasma from this figure by noting the track locations at which the intensities of these peaks become negligible as compared to the
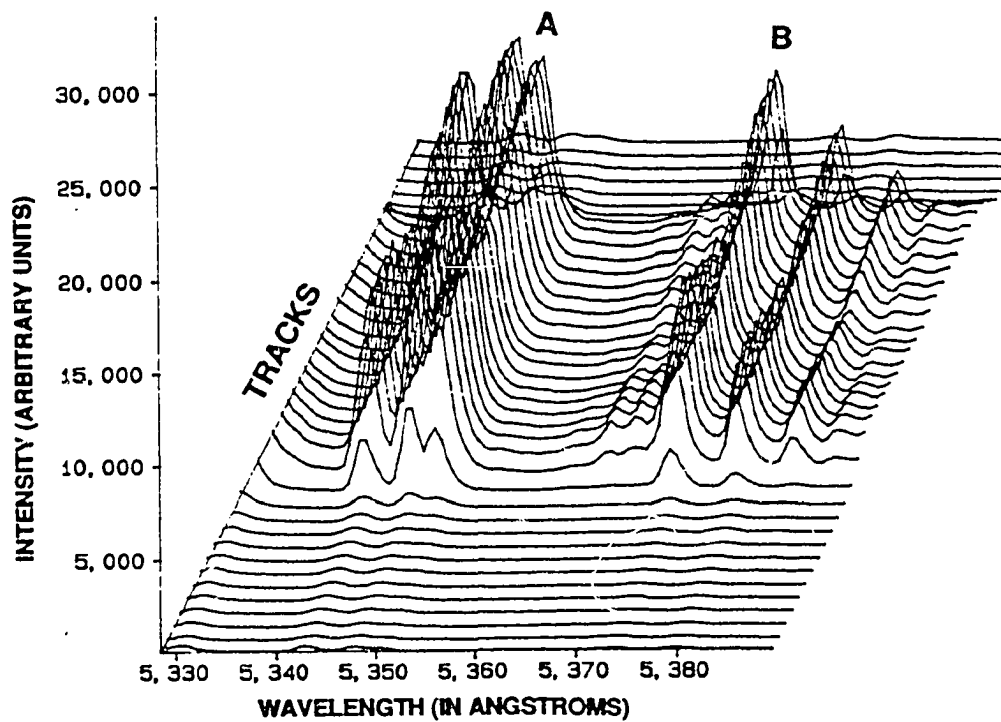
Figure 31: Typical multitrack data set obtained from the plasma during laser welding of AISI 201 stainless steel at a horizontal section in the plasma, 11.88 mm above the weld pool. (He gas flow rate = 6.66 x 10^{-5} m^3/s, welding speed = 0.005 m/s, current = 45 mA, pulse length = 0.003 s, frequency = 100 Hz.)

highest intensities obtained in between the two boundaries. One can also note from Figure 31 that the two intensities at the center of the plasma are lower than those in their immediate vicinity away from the center. This can be attributed to self-absorption effects (65) wherein the intensity of the radiations emitted at the center or the interior of the plasma is subject to absorption by the surrounding plasma leading to an attenuation of the intensities of the peaks.

Once the data were collected at a given horizontal location, the monochromator slit was moved vertically in small increments at various levels in the plasma and the corresponding intensities were collected. These intensities were deconvoluted by using the well known Abel transformation to obtain the local emissivities at various radial locations. The vertical boundaries of the plasma were identified by moving the monochromator slit till a clearly resolved spectra could not be obtained. Figure 32 depicts the three-dimensional temperature profile obtained from the plasma.

Several interesting observations can be made from Figure 32. First, the maximum half-domain of the plasma is about 4.8 mm and therefore the total domain over which the plasma extends in the radial direction is 9.6 mm. It is clear that the plasma domain is much larger than the width of the weld pool which is about 0.5 mm. The plasma is therefore completely enveloping the weld pool. Another observation is that the plasma extends to about 14.52 mm in the axial direction. This indicates that the laser beam on its way to the substrate encounters the plasma much before it reaches the sample and hence would begin to get affected by the plasma much above the weld pool. It is clear that the axial temperature (at the center of the plasma where $r = 0$
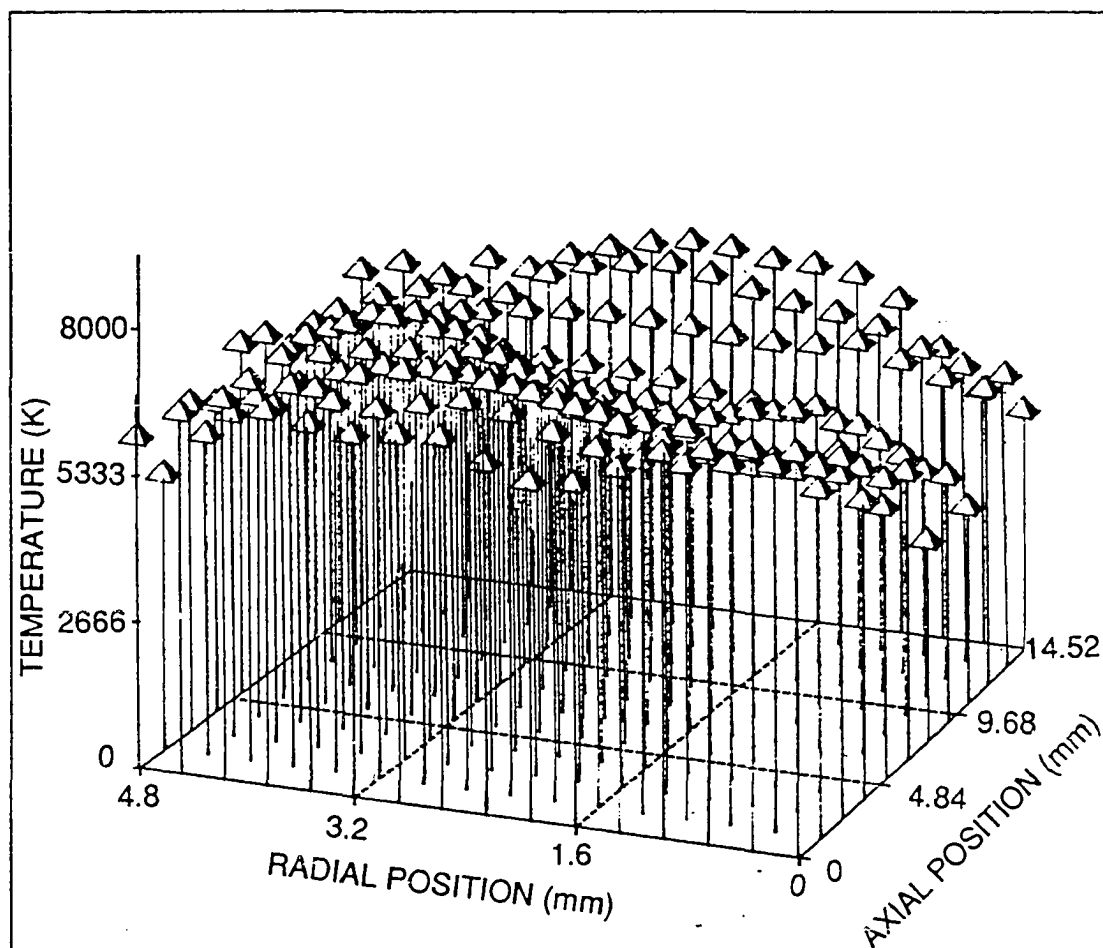
Figure 32:   A typical three dimensional temperature profile obtained
from the plasma produced during laser welding of AISI
201 stainless steel. (He gas flow rate = 6.66 x 10^{-5}
m^3/s, welding speed = 0.005 m/s, current = 45 mA,
pulse length = 0.003 s, frequency = 100 Hz.)

mm) is highest in regions just above the weld pool. In general, the temperature profile at a given vertical plane indicates that the axial temperature is not always the highest as compared to other radial locations of the plasma at that particular height though one would expect a higher temperature at the center than at the periphery. This again could be attributed to self-absorption effects wherein the lower temperature at the center reflects the decreased intensities at the center as discussed with reference to Figure 31 on page 100. As discussed in Appendix C, the average errors in these electron temperature values are +22 % and -15 % for the upper and lower limits, respectively. It should also be noted that the radial temperature distribution at various axial locations do not follow similar trends. This could be because of the self-absorption effects which is different in various regions of the plasma. In addition, the temperature values vary within a wide range, from 4657 K to 7272 K as seen from Figure 32 on page 102.

In order to determine the absorption coefficient of the laser beam, the axial temperatures at various vertical locations of the plasma are required. These axial temperatures of the plasma are considered for the absorption calculations as the axis of the laser beam impinging on the substrate is at the center of the plasma. These values are presented in Table 9 at various vertical locations of the plasma in increments of 0.1125 mm after relevant interpolation from the experimentally determined data. In addition, the number density of electrons contributed from pure Mn, Fe, Cr and He plasmas corresponding to the various temperatures are also presented in this table. These number density values were determined from Figure 30 on page

Table 9: Electron temperatures and number density of electrons contributed from pure Mn, Fe, Cr and He plasmas at various regions of the plasma.

Temp. (K)	Distance above the weld pool. (mm)	Number density of electrons in pure Mn plasma (cm^{-3})	Number density of electrons in pure Fe plasma (cm^{-3})	Number density of electrons in pure Cr plasma (cm^{-3})	Number density of electrons in pure He plasma (cm^{-3})
7272	0	0.136×10^{18}	0.111×10^{18}	0.164×10^{18}	0.234×10^{12}
7221	0.1125	0.131×10^{18}	0.107×10^{17}	0.159×10^{18}	0.204×10^{12}
7170	0.2250	0.126×10^{18}	0.102×10^{18}	0.154×10^{18}	0.176×10^{12}
7118	0.3375	0.122×10^{18}	0.982×10^{17}	0.149×10^{18}	0.153×10^{12}
7067	0.4500	0.117×10^{18}	0.941×10^{17}	0.144×10^{18}	0.132×10^{12}
7016	0.5625	0.113×10^{18}	0.901×10^{17}	0.139×10^{17}	0.113×10^{12}
6965	0.6750	0.108×10^{18}	0.862×10^{17}	0.135×10^{18}	0.975×10^{11}
6913	0.7875	0.104×10^{18}	0.823×10^{17}	0.130×10^{18}	0.836×10^{11}
6862	0.9000	0.998×10^{17}	0.786×10^{17}	0.125×10^{18}	0.715×10^{11}
6813	1.0125	0.958×10^{17}	0.751×10^{17}	0.120×10^{18}	0.615×10^{11}
6765	1.2375	0.919×10^{17}	0.717×10^{17}	0.116×10^{18}	0.528×10^{11}

96 at various temperatures for different species present in the plasma. Several interesting observations can be made from Table 9. First, the axial temperature is highest in the regions close to the weld pool. Secondly, for any given axial temperature at a particular distance above the weld pool, the electron concentration is the highest for chromium as it has the lowest ionization potential as compared to iron, manganese and helium. It is important to realize that the number density of electrons contributed from various elements in the plasma listed in Table 9 corresponds to a hypothetical case of a single species plasma. However, the plasma produced during laser welding of stainless steels is a combination of all these pure species, viz., Mn, Fe, Cr and He present in different proportions. Therefore, a knowledge of the local concentration of each of these species is necessary in order to compute the number density of electrons available from all these species.

In order to determine the total number density of electrons in the plasma produced from AISI 201 stainless steel at various locations of the plasma, a knowledge of the mole fractions of Fe, Mn, Cr and He at these locations is necessary. A mathematical model was developed to determine the concentration profiles of Cr, Mn and Fe by taking into account the transport of these species by convection and diffusion. A prerequisite for the model is an apriori knowledge of the velocity profile of the helium gas at various regions of the plasma. The velocity profiles were determined by utilizing the FLUENT software package which is a general purpose computer program for modeling fluid flow. FLUENT (76) uses a finite difference numerical procedure to solve the fundamental equations governing fluid flow namely the Navier-Stokes equations (77). A schematic diagram of the

geometrical configuration of the physical system is presented in Figure 33. As can be observed from the figure, the helium gas jet is coming out from a circular nozzle and is impinging on the weld pool and the region surrounding it. The velocity profiles of the helium gas jet in the region below the nozzle and above the specimen are important for the determination of the concentration profiles. The velocity of the helium gas at the nozzle was calculated from the volumetric flow rate (6.66×10^{-5} m^3/s) of the helium shielding gas and the area of the nozzle.

The velocity profile obtained from the FLUENT software for the case of a helium gas jet impinging on a flat plate is presented in Figure 34. One can clearly observe from this profile that the velocity near the weld pool is much smaller than the inlet gas jet velocity at the nozzle (about 530 cm/s). Such a velocity profile was used to determine the concentration profile using a finite difference model. The model essentially determines the distribution of the species vaporizing at the weld pool surface in the plasma domain. It takes into account the convective (due to the velocity of the impinging helium gas jet) and diffusive (due to the interdiffusivity of the vaporizing species in the helium gas) fluxes.

The following is the mass conservation equation utilized for a given species (91):

$$U \frac{\delta C_i}{\delta x} + V \frac{\delta C_i}{\delta y} = D_{i\text{-He}} \left(\frac{1}{x} \frac{\delta}{\delta x} \left(x \frac{\delta C_i}{\delta x} \right) + \frac{\delta^2 C_i}{\delta x^2} \right) + R_i \qquad [21]$$
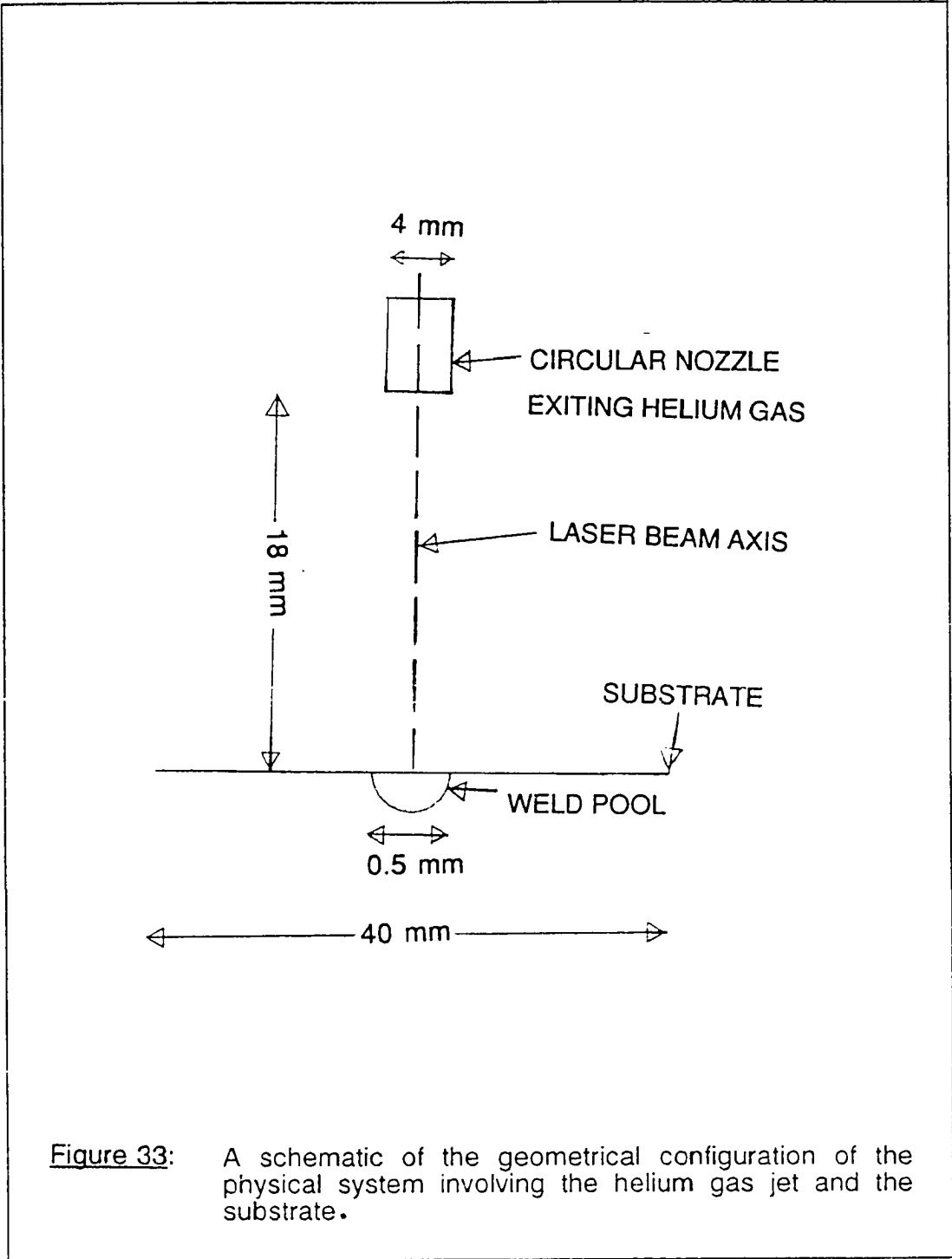
Figure 33: A schematic of the geometrical configuration of the physical system involving the helium gas jet and the substrate.
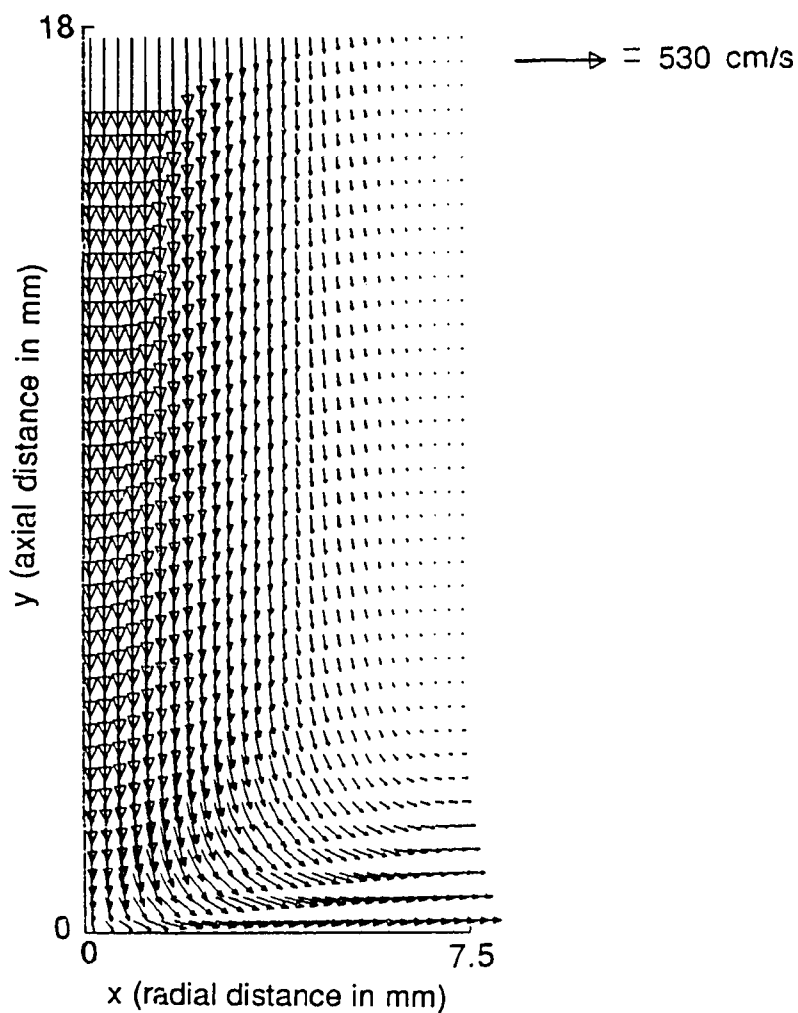
Figure 34: Typical velocity profiles of helium present in the plasma due to the helium gas jet impinging on the substrate.. (He gas flow rate = 6.66 x 10^{-5} m^3 s, radius of the nozzle through which gas flows = 0.2 cms.)

where C_i is the concentration of species i, R_i is the source term and $D_{i\text{-He}}$ is the interdiffusivity of species i in helium gas. The equation was solved using the velocity fields presented in Figure 34 on page 108. The distribution of the vaporized material from the weld pool due to both convective and diffusive fluxes were determined from this model with the appropriate boundary conditions. The details of this model are provided in Appendix E with the relevant boundary conditions. The computer program was run for Fe, Mn and Cr, and their respective concentration profiles in moles/cm^3 determined at various locations in the plasma are presented in Figure 35. It is clear that near the surface of the weld pool the concentrations of Fe, Mn and Cr were significant, while away from the pool the concentration of each species was much smaller. The total concentration of the species at the weld pool surface was calculated from the partial pressure of the vaporizing species and the calculated boundary layer temperature of about 2670 K using the ideal gas behaviour. The concentration of helium at various regions of the plasma can then be obtained by subtracting the concentrations of Fe, Mn and Cr (obtained at various locations from the results of the computer program) from the total concentration of all the species computed from ideal gas behavior. The mole fractions of Fe, Mn, Cr and He were then obtained at axial locations of the plasma in vertical increments above the weld pool and are tabulated in Table 10 at various vertical locations in the plasma along with the axial plasma temperatures at these points.

The axial temperatures and concentrations are of importance in the calculation of the absorption of the laser beam because the laser beam passes through these axial regions on its way to the substrate. It can be
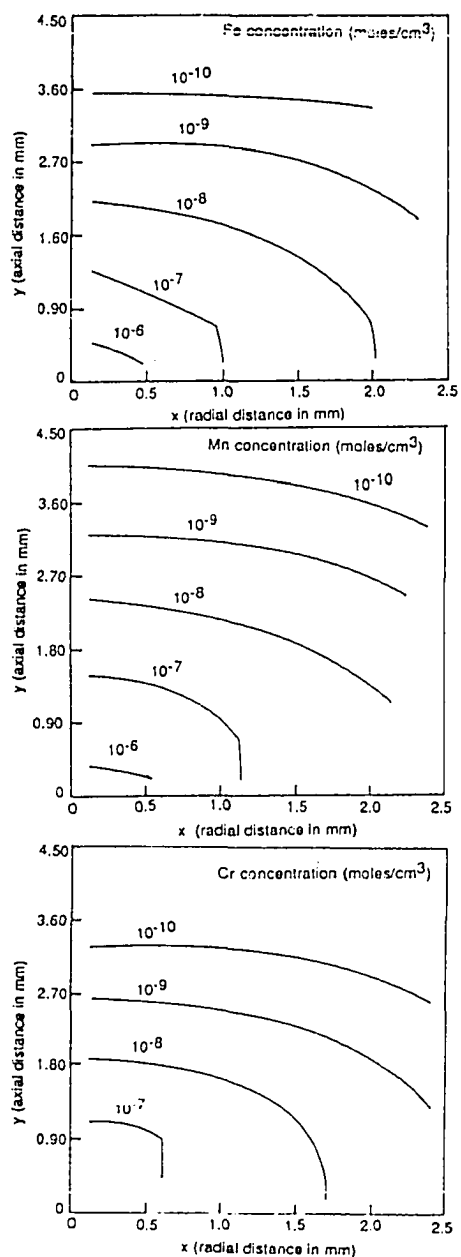
Figure 35:   Typical concentration profiles of iron, manganese and chromium in mole fraction obtained from the velocity profile of helium gas.

Table 10: Concentration of Fe, Mn, Cr and He in mole fractions at various locations of plasma corresponding to various axial temperature values.

Temp. (K)	Distance above the weld pool (mm)	Concn. of Mn (mole fraction)	Concn. of Fe (mole fraction)	Concn. of Cr (mole fraction)	Concn. of He (mole fraction)
7272	0	0.4616	0.3347	0.2036	0
7221	0.1125	0.3487	0.2490	0.1554	0.2469
7170	0.2250	0.2690	0.1853	0.1195	0.4262
7118	0.3375	0.1992	0.1335	0.0837	0.5836
7067	0.4500	0.1479	0.1014	0.0631	0.6876
7016	0.5625	0.1076	0.0727	0.0478	0.7719
6965	0.6750	0.0817	0.0548	0.0318	0.8316
6913	0.7875	0.0618	0.0398	0.0229	0.8755
6862	0.9000	0.0463	0.0305	0.0177	0.9055
6813	1.0125	0.0359	0.0235	0.0126	0.9280
6765	1.2375	0.0269	0.0183	0.0092	0.9456

noted from Table 10 that close to the weld pool not only is the electron temperature highest but also the concentration of metallic species, viz., Mn, Fe and Cr is also the highest. However, as one moves away from the weld pool, the concentration of these metallic species decreases significantly while the concentration of helium increases. The overall number density of electrons in the plasma can be obtained by multiplying the number density of electrons of pure Fe, Mn, Cr and He listed in Table 9 on page 104 with their respective mole fractions listed in Table 10 on page 111 and summing up these values (using equation [19]). From Table 11 which depicts the average number density of of electrons and electron temperatures in various regions of the plasma, it is clear that as one moves away from the weld pool, the average number density of electrons decreases.

The absorption of the laser beam in the plasma is essentially due to the free-free electron or the inverse Bremsstrahlung absorption. The ions and the atoms in the plasma do not absorb the laser beam because the probability of the multiphoton (laser beam) absorption by the bound electrons in these species is very low. Therefore, from the number density of electrons in the plasma determined at various temperatures as shown in the earlier section, one can then calculate the spectral coefficient of the actual Bremsstrahlung absorption by the free electrons in the various regions of the plasma by the following equation (78):

$$K_v = \frac{3.69 \times 10^8 \, Z^2 \, N_e \, N_+ \, T^{-0.5}}{v^3} \qquad [22]$$

where Z = atomic charge, T = electron temperature, N_+ = number density of ions (cm^{-3}) which is equal to N_e, the number density of electrons (cm^{-3}).

Table 11: Average number density of electrons and electron temperatures in various regions of the plasma.

Region of the plasma (mm)	Average electron temperature (K)	Average number density (cm^{-3})
0 - 0.1125	7246	81.151x10^{17}
0.1125 - 0.2250	7195	8.418x10^{16}
0.2250 - 0.3375	7144	6.062x10^{16}
0.3375 - 0.4500	7092	4.293x10^{16}
0.4500 - 0.5625	7041	3.067x10^{16}
0.5625 - 0.6750	6990	2.160x10^{16}
0.6750 - 0.7875	6939	1.527x10^{16}
0.7875 - 0.9000	6887	1.096x10^{16}
0.9000 - 1.0125	6837	7.975x10^{15}
1.0125 - 1.2375	6789	5.784x10^{15}

the constant value in equation [22], i.e., 3.69×10^8 has the unit $cm^5K^{1/2}s^{-3}$ and v = frequency of laser radiation (s^{-1}). As only singly charged ions are being considered in the plasma, one can take Z as equal to one. In addition, after incorporating the electroneutrality equation which requires that the number density of electrons be equal to the number density of ions and incorporating the frequency of the $10.6 \mu m$ carbon dioxide laser radiation, one obtains the following simplified equation:

$$K_v = 162.8 \times 10^{-34} (N_e)^2/(T)^{1/2} \qquad [23]$$

The absorption coefficient was calculated at different vertical regions of the plasma and is tabulated in Table 12. The extent of attenuation of the laser beam by the plasma due to the Bremsstrahlung absorption can be determined from the following equation:

$$I_j = I_{j-1} * exp(-K_v^{j-1} * \Delta Y) \qquad [24]$$

where I_{j-1} is the intensity of the laser beam emerging out of the plasma, I_j is the intensity of the laser beam entering the region of plasma under consideration, K_v^{j-1} is the absorption coefficient of the region of the plasma under consideration and Δy is the relevant plasma domain under consideration (Figure 36).

However, one has to determine the extent of attenuation of the laser beam intensity over various regions of the plasma as each region of the plasma has a different value of K_v. This can be understood from Figure 36 which illustrates the various regions of the plasma through which the laser beam passes and gets attenuated. The overall percentage laser beam intensity can be obtained from the following relation:

Table 12: Absorption coefficient values in various regions of the plasma.

Region of the plasma (mm)	Absorption coefficient (cm^{-1})
0 - 0.1125	2.535
0.1125 - 0.2250	1.360
0.2250 - 0.3375	0.708
0.3375 - 0.4500	0.356
0.4500 - 0.5625	0.182
0.5625 - 0.6750	0.091
0.6750 - 0.7875	4.558×10^{-2}
0.7875 - 0.9000	2.355×10^{-2}
0.9000 - 1.0125	1.252×10^{-2}
1.0125 - 1.2375	6.609×10^{-3}

Incident laser beam

I_o

I_1

I_{j-1}

I_j

I_n

Material

Figure 3G: Schematic of the various regions of the plasma contributing to the attenuation of the laser beam.
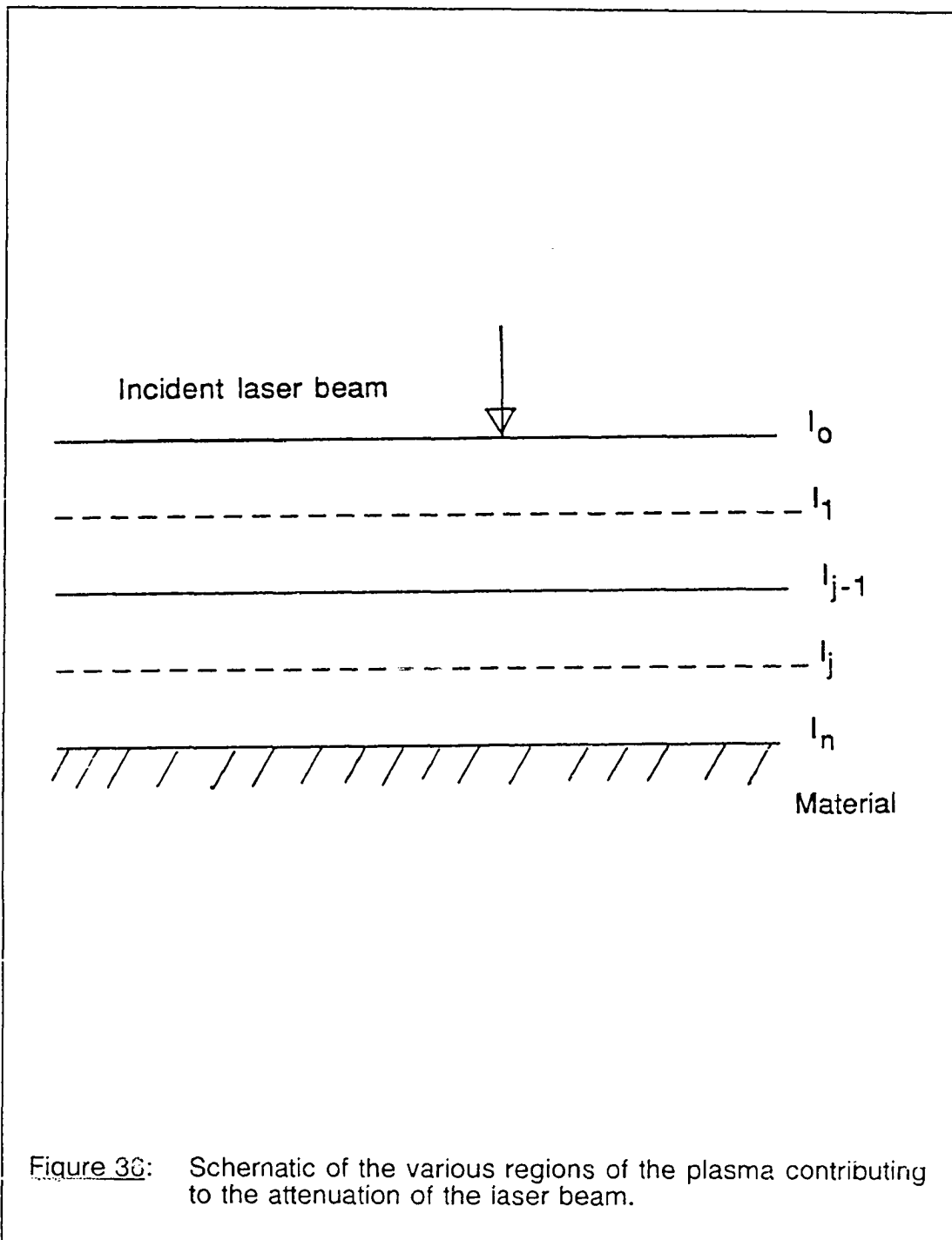
$$\% \text{ laser intensity absorbed} = \frac{(I_o - I_n) \times 100}{I_o}$$

<div align="right">[25]</div>

The percentage plasma intensity absorbed from these calculation was found to be about 5.8 %. Therefore, it is clear that the plasma produced during pulsed mode laser welding of AISI 201 stainless steels does indeed act as a hindrance to the laser-solid interaction by absorbing the laser intensity by Bremsstrahlung or free-free electron absorption. However, the percentage absorption by the laser beam is not considerable because of the effective shielding by the helium gas jet during laser welding.

4.2.10   Role of minor impurities

4.2.10.1   Role of sulfur and oxygen

Data on vaporization rates indicate that the rate of vaporization of iron from samples doped with sulfur was higher than that for the pure iron samples as can be observed from Figure 37. Since sulfur is known to be adsorbed preferentially at the surface, the presence of sulfur leads to an increase in the absorption of the laser beam and consequently higher vaporization rate. This increase in the absorptivity has been observed experimentally by Khan (60). Minor amounts of surface active elements such as sulfur and oxygen present in the base metal can have a significant effect on the vaporization rate and the chemical composition of the weldment. In extreme cases, this can lead to the lack of reproducibility in the composition of the weldments formed from base materials containing various amounts of surface active impurities.
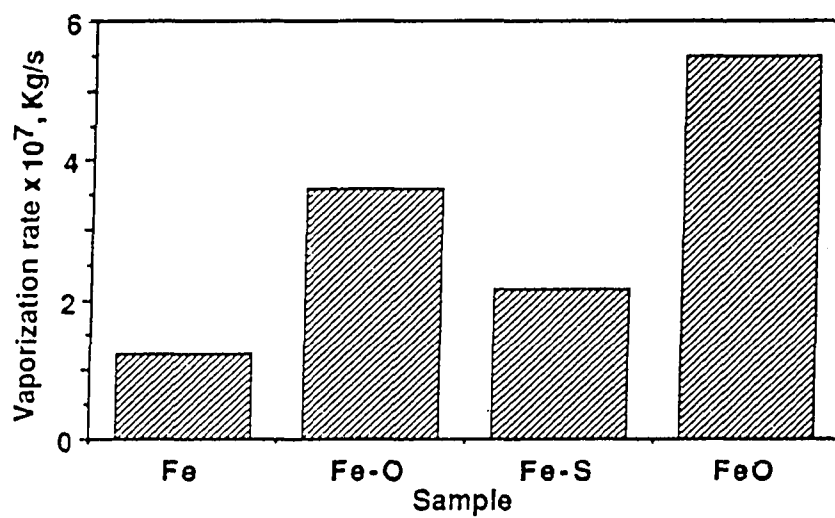
Figure 37: Bar graph showing the increase in the vaporization rate of or iron corresponding to ultrapure iron samples, sulfur doped, oxygen doped and oxidized iron samples.

Figure 38 depicts the spectrum obtained from the plasma produced during laser welding of an iron sample doped with sulfur (0.013 wt %). On comparing this spectrum with that obtained from the plasma produced from an ultra pure iron sample under similar conditions of welding (Figure 25 on page 83 and Figure 38), it is observed that the addition of sulfur increases the intensities of the iron peaks. The increase in the intensity of the iron peaks resulting from the presence of sulfur in the alloy was also observed by Savitskii and Leskov (6) and Dunn et al. (12) for the arc welding of commercial alloys. Emission spectra were also obtained from the plasma produced during laser welding of iron samples doped with oxygen and oxidized iron samples. Figure 39 depicts the variation of the intensities of the major peaks of iron (observed in Figure 25 on page 83) for various iron samples.

It is clear that the presence of surface active elements such as sulfur and oxygen increases the intensities of the major iron peaks. The increased vaporization rate from the doped and the oxidized samples (observed in Figure 37 on page 118) results in an increase in the number density of atoms in the ground state (n_o). The number density of atoms at the upper excited energy level (n_{aq}) also increases according to the Boltzmann distribution (equation 8). This, in turn, contributed to the higher intensity of emission (equation 7) observed in spectra obtained from Fe-S, Fe-O and oxidized iron samples. It is to be noted that the increased intensity is not significantly contributed by changes in the electron temperatures in the plasma for various samples as can be noted from Table 6 on page 86. The temperatures of the plasma for the sulfur-doped, oxygen-doped and the oxidized samples were

Figure 38: A typical spectrum of the plasma produced during laser welding of ultra pure iron sample doped with sulfur. (He gas flow rate = 3.33 x 10^-5 m^3/s, welding speed = 0.005 m/s, current = 35 mA, pulse length = 0.003 s, frequency = 100 Hz, sample thickness = 2 x 10^-3 m).

80000

60000

Intensity (arbitrary units)

40000

20000

0

4045.81   4202.0   4271.76

Wavelength (angstroms)

■ Fe
▨ Fe-O
■ Fe-S
▨ FeO

Figure 39:   Bar graph showing the various intensities of the major peaks of iron obtained from the emission spectra corresponding to various iron samples. (He gas flow rate = 3.33 x 10^{-5} m^3/s, welding speed = 0.005 m/s, current = 35 mA, pulse length = 0.003 s, frequency = 100 Hz, sample thickness = 2 x 10^{-3} m).

determined by the technique described in section 4.2.7 from their respective emission spectra. The increase in the vaporization rate and the intensities of iron peaks for the doped and oxidized samples can be easily attributed to the increased absorptivity of these samples giving rise to an increase in the surface area and the temperature distribution in the weld pool resulting in the increased vaporization rate. However, it is difficult to determine from the welding data if the changes in the vaporization rate due to the presence of surface active elements in the base metal is attributable exclusively to changes in weld pool surface area and temperature distribution or is contributed by additional interfacial effects due to the presence of these elements. In either case, the primary interfacial effect of sulfur cannot be easily separated from the secondary effects of sulfur manifested in changes in surface area and temperature distribution. To determine the true interfacial effect of sulfur on the metal vaporization rate, a series of experiments were designed by Sahoo (79) where iron and copper drops doped with oxygen or sulfur were allowed to vaporize isothermally both in the presence and the absence of a low pressure argon plasma. The rates were compared with the rate of vaporization of ultrapure metal drops under appropriate conditions. Sahoo's experiments revealed that the presence of oxygen and sulfur in the samples increased the vaporization rate of copper. This effect is consistent with interfacial turbulence phenomena which occur when a surface active element is present (63).

Experiments performed by Langmuir on the evaporation of ether from water illustrate this phenomenon (63). When talc was scattered on the surface of water, the particles exhibited abrupt local movements. This is

because the eddies in the water facilitate segregation of ether to the surface which gives rise to a local surface tension decrease. At the same time, the eddies from the ambient atmosphere remove the ether, thereby raising the surface tension as shown in Figure 40. At any given instant the interface consists of areas of relatively low and relatively high surface tensions. The spatial variation of interfacial tension causes local flow and surface fluctuations exhibited by the motion of the talc particles. These local movements of the interface increase surface area and the rate of vaporization. The oxygen and sulfur present in the copper samples result in interfacial turbulences and lead to enhanced vaporization rates of copper. The same effect could be attributed to the increased vaporization rate of iron for samples doped with sulfur or oxygen (during laser welding experiments) apart from absorptivity considerations.

4.2.11   Use of emission spectroscopy to determine the composition of the base metal

The emission spectra obtained from the plasma can also be utilized to determine the composition of the base metal apart from providing an insight into the temperature and the composition of the species present in the plasma. In this section, a technique to determine the composition of manganese in high manganese stainless steel will be presented. This technique, which can in turn be adapted to other alloys, falls under the broad field of quantitative spectrochemical analysis. In spectrochemical analysis, emission spectra of atoms and ions are used for detecting and determining the concentration of elements. In order to determine the concentrations of the elements in various samples, "intensities" of spectral lines are evaluated.

Figure 40: Figure showing the local variation in the surface tension on the surface of a fluid with a surface active element in it giving rise to interfacial turbulence phenomena (from reference 63).
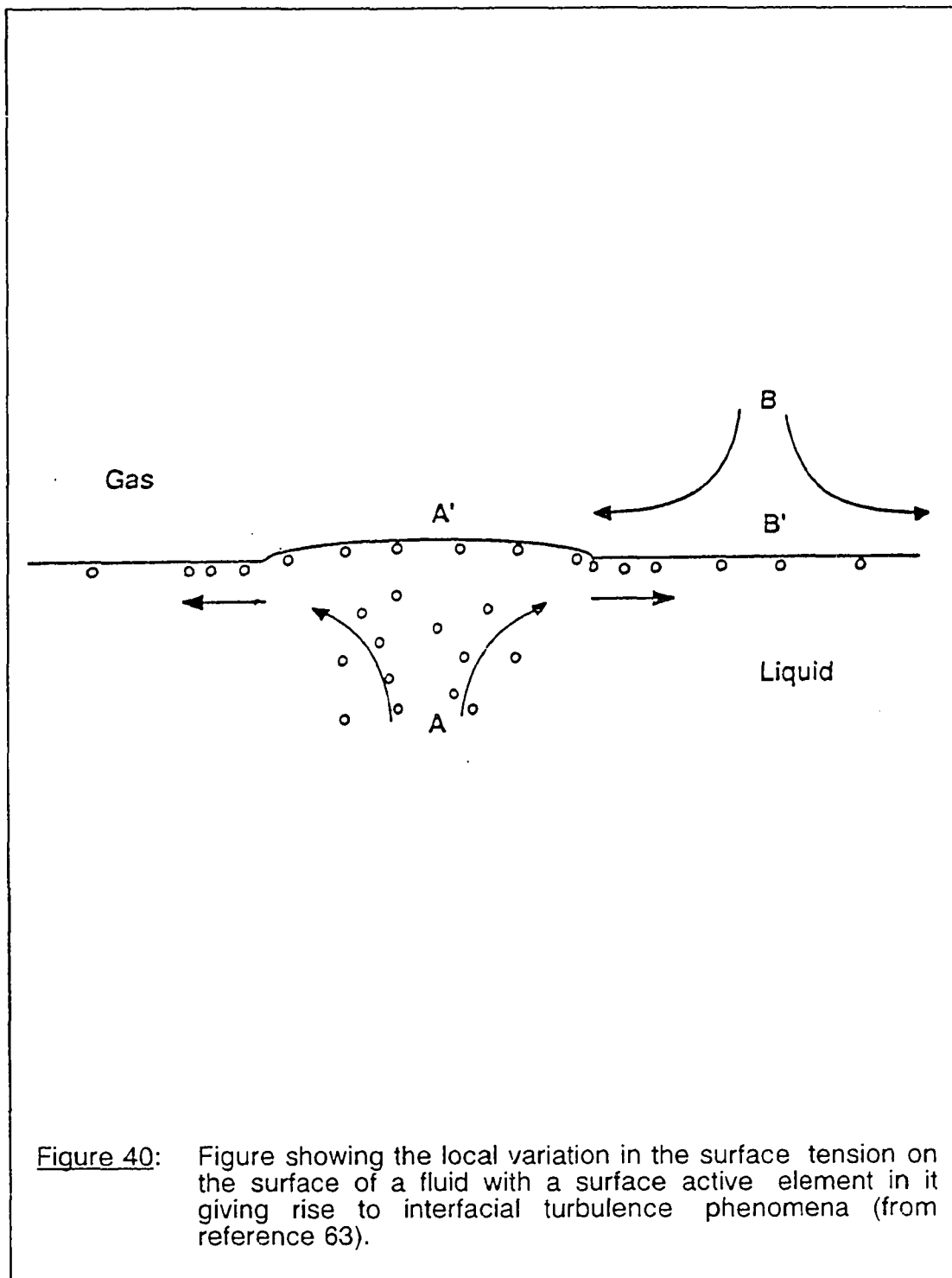
Schrenk (80), in his review on historical development of high-energy excitation sources for analytical emission spectroscopy, has listed several sources of energy used for the excitation of a sample to be analyzed including sparks, arcs, lasers and plasmas. The use of lasers as excitation sources for spectroscopic purposes was investigated by Brech and Cross (81). They, however, limited the use of the laser to vaporizing the sample and then used a spark source for excitation purposes. Belle and Johnson (82) conducted an in-depth composition profile analysis of various alloys using optical emission glow discharge spectrography. Cremers (83) has used laser-induced breakdown spectroscopy (LIBS) to provide a rapid analysis of metals at distances between 0.5 m and 2.4 m from the focussing lens and light-collection optics. The laser sparks were generated with the use of pulses from a Nd:YAG laser, and the spark light was collected by the use of a fiber optic cable. They reported that although other types of lasers generating pulses of comparable power could be used for LIBS, an exception maybe the pulsed carbon dioxide laser, because of the high reflectivity of metal surfaces at the $10.6\mu m$ wavelength of this laser. In this study, the use of a pulsed carbon dioxide laser for the analysis of the base metal composition is demonstrated.

In order to accurately determine the unknown composition of an alloy, a working or calibration curve is needed which relates the information from the spectral emissions from the plasma produced due to the laser-solid interaction with the known compositions of a series of alloys. The spectral intensities from an unknown alloy can then be interpolated onto this calibration curve to read off the composition of the unknown alloy (65,84). The basis of

quantitative spectrochemical analysis is a simple, empirical relationship between the content G of an element in the sample and the intensity I of a spectral line in the source of excitation. This relationship is usually expressed by the Scheibe-Lomakin equation (65) as follows:

$$I = K * G^m \qquad [26]$$

The above equation is based on the assumption that, in principle, intensity is proportional to concentration . The deviations from this proportionality, primarily that caused by self-absorption (65), are taken into account by the exponent m. Equation [26] can be represented as follows:

$$\log(I) = m \log(G) + \log(K) \qquad [27]$$

The resulting plot of log(I) versus log(G) is commonly referred to as the working curve. Generally, intensity I is not measured absolutely but is taken as the intensity ratio of the analysis line and a suitable reference line. The concept of an "internal standard" is important to understand while performing quantitative laser spectrochemical analysis. An internal standard (84) can be a weak line of a major constituent of the sample, that is present in all the standard samples at a constant concentration level. In practice, an internal standard whose concentration is constant produces a spectral emission (reference) line whose intensity is compared with the intensity of a spectral (analysis) line of the element whose concentration is desired. The intensity ratio of the analysis and the reference line should be insensitive to changes in the excitation conditions. For the lines to meet this requirement, both should be either atom lines or ion lines (65). Moroever, their excitation potentials

should be equal. This, however, holds true only if the ionization energies of the internal standard and the analysis element are also alike. In addition, the concentration of the reference element should be fairly constant in all the alloys used for the construction of the calibration curve. For the determination of manganese concentration in high-temperature alloys, Dilworth (85) had utilized the Mn II 2933.06 $^{\circ}$A emission as the analysis line and Cr II 3379.82 $^{\circ}$A emission as the reference line and obtained a reliable working curve for their studies. In the high manganese stainless steels used in the present study, iron has been selected as the internal standard as its composition remains fairly constant and as it is the major constituent in both AISI 201 and USS tenelon stainless steels used for obtaining the calibration curve. The element whose concentration we wish to monitor in these studies is manganese. It is thus possible to obtain an intensity ratio rather than a single spectral line intensity. It is basic to the concept of an internal standard to consider that any factor that affects the intensity of the internal standard spectral line (Fe) has a similar effect on the intensity of the unknown spectral line (Mn). In order to develop an equation which uses the intensities and concentrations of both iron and manganese peaks one has to first write the Scheibe-Lomakin equation for both these emissions as follows:

$$I_{Mn} = K_{Mn} * G_{Mn}^{m} \tag{28}$$

where I_{Mn} is the intensity of a manganese emission, K_{Mn} and m are constants and G_{Mn} is the weight percent of manganese.

$$I_{Fe} = K_{Fe} * G_{Fe}^{m} \tag{29}$$

where I_{Fe} is the intensity of an iron emission, K_{Fe} and m are constants and G_{Fe} is the weight percent of iron. On taking the ratios of equations [28] and [29], one obtains the following equation:

$$I_{Mn}/I_{Fe} = (K_{Mn}/K_{Fe})^x (G_{Mn}/G_{Fe})^m \qquad [30]$$

Taking logarithms on both sides of equation [30], one obtains the following equation:

$$\log\left[\frac{I_{Mn}}{I_{Fe}}\right] = \log\left[\frac{K_{Mn}}{K_{Fe}}\right] + m\log\left[\frac{G_{Mn}}{G_{Fe}}\right] \qquad [31]$$

In this study, from the two given alloys, viz., AISI 201 and USS tenelon steels whose compositions are presented in Table 13, two more alloys were produced by melting these two alloys of known compositions in different proportions in a radio frequency induction furnace. The various manganese and iron compositions in the four alloys utilized for the determination of the calibration curve are presented in Table 14. All these four alloys were laser irradiated under identical welding conditions and emission spectra were obtained. A typical spectrum obtained from AISI 201 stainless steel is shown in Figure 41.

The spectrum was collected using a vertical arrangement of the monochromator slit. The spectra obtained for the other alloys are depicted in appendix F. The ratios of the intensities of Mn 4030.76 ^{O}A and Fe 4143.87 ^{O}A were noted from each of the spectra and the logarithm of their ratio as a function of logarithm of the ratio of wt % Mn and wt % Fe are plotted in Figure 42. Each data point in Figure 42 corresponds to an average of at least

Table 13: Composition of AISI 201 and USS tenelon stainless steels.

Element	Composition in wt % of AISI 201 stainless steel.	Composition in in wt % of USS tenelon stainless steel.
Cr	16.5	17.6
Mn	6.1	15.6
Ni	4.85	0.75 (max)
C	0.15 (max)	0.12 (max)
Si	1.00 (max)	1.00 (max)
P	0.06	0.045
S	0.03	0.03
other elements	N, 0.25 (max)	N, 0.25 (max)
Fe	balance	balance

Table 14: Composition and intensity ratios of all the alloys utilized for the construction of the calibration curve.

Parameter	AISI 201 steel.	Steel A.	Steel B.	USS Tenelon steel.
wt % Mn	6.1	7.75	12.033	15.6
wt % Fe	72.5	70.49	68.36	67.5
$\left[\dfrac{wt\ \%\ Mn}{wt\ \%\ Fe}\right]$	0.0841	0.1099	0.176	0.2311
$\log\left[\dfrac{wt\ \%\ Mn}{wt\ \%\ Fe}\right]$	-1.075	-0.9588	-0.7544	-0.636
$\left[\dfrac{I_{Mn\ 4030}}{I_{Fe\ 4143}}\right]$	3.56	3.6	4.59	5.616
	3.65	4.29	4.085	5.042
	3.298			
	3.695			
Average $\left[\dfrac{I_{Mn\ 4030}}{I_{Fe\ 4143}}\right]$	3.55	3.945	4.3375	5.329
Average $\log\left[\dfrac{I_{Mn\ 4030}}{I_{Fe\ 4143}}\right]$	0.5502	0.596	0.6372	0.7266

Figure 41: A typical spectrum of the plasma produced during laser welding of AISL 201 stainless steel. (Ar gas flow rate = 3.33 x 10⁻⁵ m³/s, welding speed = 0.005 m/s, current = 45 mA, pulse length = 0.003 s, frequency = 100 Hz).

Figure 42: A log-log plot of the ratio of intensities of Mn and Fe as function of the ratio of wt % Mn and wt % Fe. (Ar gas flow rate = 3.33×10^{-5} m^{3}/s, welding speed = 0.005 m/s, current = 45 mA, pulse length = 0.003 s, frequency = 100 Hz).

two experimental observations of spectra obtained from a particular alloy. The data corresponding to Figure 42 are presented in Table 14 on page 130. It is clear that there is a considerable scatter in the data which is responsible for the deviation of the calibration curve from linearity. Possible source of error could be the instability of the plasma which is being produced under pulsed mode operation of the laser. In addition, self absorption effects could also contribute to the scatter in the data points wherein the emissions of iron and manganese present in the plasma in significant amounts could be absorbed before being detected by the spectroscope. These two lines of Mn and Fe were selected as they were found to satisfy most of the restrictions on the line pairs utilized for the construction of the calibration curve (65). It is clear that this ratio increases linearly with the wt % Mn present in the base metal as the amount of variation of wt % Fe in all the four alloys is not as significant as the variation of Mn. A calibration curve has thus been constructed from which within the composition range of about six to about sixteen wt % Mn, one can use Figure 42 to determine the composition of an unknown alloy from its emission spectra (for a known amount of iron in the alloy).

The data presented in Figure 42 have been linearly regressed and the following equation was obtained:

$$\log\left[\frac{I_{Mn\,4030}}{I_{Fe\,4143}}\right] = 0.941 + 0.366 \log\left[\frac{wt\ \%\ Mn}{wt\ \%\ Fe}\right] \qquad [32]$$

The above equation is similar to the general form of equation [31] derived earlier. From this study, it is clear that emission spectroscopic techniques can be utilized to determine the composition of the base metal.

Chapter 5

SUMMARY AND CONCLUSIONS

A significant loss of alloying elements was observed during laser welding of AISI 201 stainless steels. From the experimental data it was found that the vaporization rate increased significantly with laser power but was found to be insensitive to the welding speed during continuous wave laser welding. The weld pool temperature determined by the selective vaporization technique was found to increase mildly with laser power. The temperature was insensitive to the welding speed. The mechanism of vaporization was determined to be controlled by the vaporization at the weld pools surface as the transport of alloying elements in the liquid phase and gas phase were found to be rapid. The presence of plasma reduced the vaporization rate of pure copper drops. The rate of vaporization of alloying elements during laser welding of stainless steels was controlled by plasma influenced intrinsic vaporization at the weld pool surface.

Emission spectroscopy was utilized to characterize the plasma when high manganese stainless steel (AISI 201) samples were welded with a carbon dioxide laser at a peak power density of 1.2×10^6 watts/cm^2. The dominant species in the plasma were found to be iron, manganese and chromium which were present primarily in their excited neutral states. When the welding was conducted at constant welding speed, shielding gas flow rate, and composition, an increase in the vaporization rate was accompanied by a concomitant increase in the intensities of various peaks. The electron temperature was found to be between 4,000 and 9,400 K. The temperatures

obtained from the plasma produced during laser welding of pure iron samples were found to be more than those observed from the plasma produced from AISI 201 stainless steels. This is because of increased self-absorption effects in the former which, in turn, tends to raise the temperature of the pure iron plasmas determined by the slope method. When experiments were performed with ultrapure iron samples that were either doped with oxygen or sulfur, or were oxidized, the intensities of iron peaks and the vaporization rates were higher in all cases than the corresponding values for the untreated ultrapure iron samples.

Electron temperatures were measured in the entire plasma domain in three dimensions. The temperature data were utilized to calculate the number density of electrons contributed from pure Mn, Fe, Cr and He plasmas. In addition, the velocity and concentration profiles of various species were determined from fluid flow and mass transfer considerations. The overall number densities of electrons were determined from the number densities corresponding to pure Mn, Fe, Cr and He plasmas and their respective concentration profiles. The number density and the temperature data along with the data on the plasma domain revealed that the extent of attenuation of the laser beam due to inverse Bremsstrahhlung absorption could be about 5.8 % under the conditions of the present study. The decrease in the alloying element vaporization in the presence of plasma is not only due to the space charge effect but also due to the attenuation of the laser power by the plasma. It was demonstrated that the emission spectroscopic data can also be utilized to determine the concentration of manganese in stainless steels.

The significance of this work is that a technique has been developed by which the alloying element loss, the composition of the weldment, the weld penetration and the aspect ratio can be monitored under certain welding conditions by a non-contact, non-intrusive technique of emission spectroscopy. An understanding of the laser-plasma-interactions has been obtained from the studies involving the determination of the absorption of the laser beam by the plasma. In addition, an understanding of the mechanism of vaporization, the role of plasma on vaporization kinetics and the vaporization losses under various welding conditions obtained from this study in turn provide us a data base using which one can control or suppress the vaporization rates.

5.1   Suggestions for future work

The present study determined the various features essential for understanding the mechanism of alloying element vaporization. The emission spectroscopic studies provided us a technique to monitor the alloying element loss in addition to giving us an insight into the laser-plasma-solid interactions. However, there is a lot of scope for further research in this area as discussed below.

1. The extent of manganese loss can be controlled or compensated for by using filler rods of manganese in controlled amounts during laser welding.

2. Studies can be conducted to determine if the electron temperature, vaporization losses and penetration are insensitive to minor additions of

oxygen or nitrogen to the shielding gas. This study is of importance to practical laser welding environment as these gas impurities are easily brought into the shielding environment from air.

3. This study could be adapted to other commercially important alloys such as Al-Mg alloys in order to get an insight into the plasma obtained during laser welding of these alloys.

BIBLIOGRAPHY

1) C.O. Brown, Appl.Phys. Letters., vol. 17, no. 9, 1970.

2) C. K. N. Patel, Physics Review., vol. 136, A1187, 1964.

3) A. Blake and J. Mazumder, J. Eng. Ind., vol. 107, P. 275, 1964.

4) J. C. Chennat and C.E. Albright, Proceedings of the International Congress of Application of Lasers and Electron Optics (ICALEO), Laser Institute of America, vol. 44, pp. 76-85, 1984.,

5) J. F. Ready, Industrial Applications of Lasers, Academic Press, New York, pp. 353-354, 1971.

6) A. Paul and T. DebRoy, Advances in Welding Science and Technology, S. A. David, ed., ASM International, pp. 29-33, 1986.,

7) E. V. Locke, E. D. Hoag and R. A. Hella, Welding Journal, vol. 51, pp. 245s-249s, 1972.

8) C. M. Banas, Proceedings of the C.E.G.B. International Conference on Welding Research Related to Power Plants, N. E. Eaton and I. M. Wyatt, Southampton, England, p. 565, September 17-21, 1972.

9) W. B. Estill and B. D. Formisano, Proceedings of the International Congress of Application of Lasers and Electron Optics (ICALEO), Laser Institute of America, vol. 38, p. 67, 1983.

10) M. M. Savitskii and G. I. Leskov, Automatic Welding, vol. 33, no. 9, pp. 11-16, 1980.

11) S. S. Glickstein, Welding Journal, vol. 55, pp. 222s-229s, 1976.

12) C. B. Shaw, Jr, Welding Journal, vol. 54, pp. 33s-44s, 1975.

13) W. S. Bennet and G. S. Mills, Welding Journal, vol. 53, pp. 548s-553s, 1974.

14) J. C. Metcalfe and M. B. C. Quigley, Welding Journal, vol. 56, pp. 133s-139s, 1977.

15) J. F. Key, M. E. Mciwain and L. Isaacson, Sixth International Conference on Gas Discharges and Their Applications, Conf. Publ., no. 189, part 2, Institution of Electrical Engineers, New York, pp. 235-238, 1980.,

16) G. J. Dunn, C. D. Allemand and T. W. Eagar, Metall. Trans.,vol. 17A, pp. 1851-1863, 1986.

17) G. S. Mills, Welding Journal, vol. 56, pp. 186s-188s, 1977.

18) G. S. Mills, Welding Journal, vol. 56, pp. 93s-96s, 1977.

19) T. J. Rockstroh and J. Mazumder, Journal of Applied Physics, vol. 61, no. 3, pp. 917-923,1987.,

20) J. T. Knudtson, W. B. Green and D. G. Sutton, Journal of Applied Physics, vol. 61, no. 10, pp. 4771-4780, 1987.

21) L. R. Hettche, E. A. Metzbower, J. D. Ayers and P. G. Moore, Naval Research Reviews, vol. 28, p. 4, 1981.,

22) D. W. Moon and E. A. Metzbower, Welding Journal, vol. 62, p. 53s, 1983.

23) D. B. Snow and E. M. Breinan, United Technologies Research Center, Connecticut, ONR report # R78-911989-14, July, 1978.

24) E. A. Metzbower, Naval Engineers Journal, pp. 49-58, August 1981.

25) N. Rykalin, A. Uglov and A. N. Kokora, Laser Machining and Welding, Mir Publishers, Moscow, p. 226, 1978.

26) P. A. A. Khan and T. DebRoy, Met. Trans., vol. 15B, p. 641, 1984.

27) A. Paul, Ph.D. thesis, The Pennsylvania State University, 1987.

28) A. Block Bolten and T. W. Eagar, Metall. Trans., vol. 15B, pp. 461-469, 1984.

29) L. F. Mondolfo, Aluminum Alloys, Butterworth & Co. Ltd., p. 315 and 369, 1976.

30) P. E. Denny and E. A. Metzbower, Proceedings of the ICALEO, Laser Institute of America, vol. 38, pp. 80-86, 1983.

31) T. J. Rockstroh, Ph.D. thesis, University of Illinois at Urbana Champaign, 1986.

32) G. V. Marr, Plasma Spectroscopy, Elsevier Publishing Company, p. 1, 1968.

33) Yu. P. Raizer, Soviet Physics JETP, vol. 31, no. 6, pp. 1148-1154, 1970.

34) M. C. Fowler and D. C. Smith, Journal of Applied Physics, vol. 46, no.1, pp. 138-150, Jan. 1975.

35) A. N. Pirri, R. G. Root and P. K. S. Wu, AIAA Journal., vol. 16, no. 12, pp. 1296-1304.

36) G. Weyl, A. N. Pirri and R. G. Root, AIAA Journal., vol. 19, no. 4, pp. 460-469.

37) K. Minamida, S. Yamaguchi, H. Sakurai and H. Takafuji, Proceedings of the ICALEO, Laser Institute of America, vol. 31, pp. 65-72, 1982.

38) R. S. Arnot and C. E. Albright, Proceedings of the ICALEO, Laser Institute of America, vol. 38, pp. 51-58, 1983.

39) R.D. Dixon and G.K. Lewis, Proceedings of the ICALEO, Laser Institute of America, vol. 38, pp. 44-50, 1983.

40) E. Beyer, L. Bakowsky, R. Poprowe and G. Herziger, Proceedings Laser-83, Opto-Elektronik, Munchen, 1983.

41) A. Matsunawa, H. Yoshida and S. Katayama, Proceedings of the ICALEO, Laser Institute of America, vol. 44, pp. 35-42, 1984.

42) A. Matsunawa and S. Katayama, Proceedings of the ICALEO, Laser Institute of America, , vol. 38, pp. 41-43, 1983.

43) G. K. Lewis and R. D. Dixon, Welding Journal, , vol. , pp. 49s-54s,

44) R. D. Dixon and G. K. Lewis, Welding Journal, , vol. , pp. 71s-78s,

45) R. D. Dixon and G. K. Lewis, Proceedings of the ICALEO, Laser Institute of America,, vol. 44, pp. 28-34, 1984.

46) I. Miyamato, H. Maruo and Y. Arata, Proceedings of the ICALEO, Laser Institue of America. , vol. 44, pp. 68-75, 1984.

47) Y. Arata, N. Abe, T. Oda and N. Tsujii, Plasma, Electron and Laser Beam Technology,, Y. Arata, ed., ASM Metals Park, pp. 517-523.

48) R. C. Johnson, Atomic Spectra, chapter 1, John Wiley and Sons, New York, 1961.

49) B. P. Straughan and S. Walker, Spectroscopy, vol. 1, chapter 1, John Wiley and Sons, New York, 1976.

50) M. Venugopalan, Reactions under Plasma Conditions, vol. 1, chapter 7, Wiley-Interscience, 1968.

51) R. S. Adrian, D. R. Airey, R. C. Kleine and E. J. Ormerod, Sixth International Conference on Gas Discharges and their Applications, Conf. Publ., no. 189, part 2, Institution of Electrical Engineers, New York, NY, pp. 231-234, 1980.

52) C. R. Heiple and J. R. Roper, Trends in Welding Research in the U.S., S. A. David, ed., ASM, Metals Park, p 489, 1982.

53) H. R. Griem, Plasma Spectroscopy, McGraw-Hill Book Company, 1964.

54) W. L. Wiese, Line Broadening,Plasma Diagnostic Techniques, R. H. Huddlestone and S. L. Leonard, eds., Academic Press, New York, p. 267, 1965.

55) P. Sahoo and T. DebRoy, Metall. Trans., vol. 18B, pp. 597-601, 1987.

56) Y. Arata, S. Miyake, H. Matsuoka and H. Kishimoto, Trans. JWRI., vol. 61, no. 10, pp. 4771-4780.

57) E. T. Turkdogan, S. Ignatowicz and J. Pearson, Journal of the Iron and Steel Institute, pp. 349-354, August 1955.

58) J. A. Kitchener, J. O'M. Bockris, Molly Gleiser and J. W. Evans, Acta Metallurgica, vol. 1, pp. 93-101, Jan. 1953.

59) J. M. Levner and A. Thevenon, Lasers and Applications, pp. 89-93, Jan. 1984.

60) P. A. A. Khan, Ph.D. thesis, The Pennsylvania State University, 1987.

61) R E. Honig and D. A. Kramer, Physico-Chemical Measurements in Metals Research, Interscience Publishers, New York, vol. 4, pp. 505-517, 1970.

62) R. Hultgren, P. D. Desai, D. T. Hawkins, M. Gleiser, K. K. Kelly and D. D. Wagman, Selected Values of the Thermodynamic Properties of the Elements, ASM, p. 6-7, 1973.

63) F. D. Richardson, Physical Chemistry of Metals in Metallurgy,Academic Press, London, 1973, vol. 2, p. 447.

64) P. Kozakevitch, Surface Phenomena of Metals, S. C. I. Monograph, no. 28, 1968, p. 223.

65) P. W. J. M. Boumans, Theory of Spectrochemical Excitation, Hilger and Watts Ltd., London, 1966.

66) R. C. Weast, Handbook of Chemistry and Physics, 64 th edition, CRC press Inc., pp. E-192 to E-318, 1983-84.

67) G. Bekefi, Principles of Laser Plasmas, Wiley, New York, 1976.

68) J. T. Fuhr, G. A. Martin, W. L. Wiese and S. M. Younger, Journal of Phys. Chem. Reference Data, vol. 10, no. 2, pp. 327-387, 1981.

69) W. L. Barr, Journal of the Optical Society of America, vol. 52, pp. 885-888, 1962.

70) H. N. Olsen, The Physics of Fluids, vol. 2, pp. 614-623, 1959.

71) J. T. Fuhr, Private Communication, Data Center on Atomic Center Transition Probabilities, Center for Radiation Research, NBS, August 1987.

72) A. N. Pirri, N. H. Kemp, R. G. Root and R. K. S. Wu, Theoretical Laser Effects Studies, Final Report, PSI-TR-89, Physical Sciences Inc., Jan. 1977.

73) G. J. Dunn and T. W. Eagar, Metall. Trans., vol. 17A, pp. 1865-1871, 1986.

74) C. Weisman, Welding Handbook, 7 th edition, vol. 1, p. 52, AWS, Miami, Florida, 1976.

75) C. E. Moore, Atomic Energy Levels,vols.1-3, NSRDS-NBS35, NBS Washington, D.C., 1971.

76) FLUENT MANUAL, Version 2.8 update,Creare Incorporated, Hanover, New Hampshire 03755, June 1985.

77) F. M. White, Viscous fluid flow,McGraw-Hill, New York, pp. 172-178, 1974.

78) Ya. B. Zwl'dovich and Yu. P. Raizer, Physics of Shock Waves and High-temperature Hydrodynamic Phenomena, vol. 1, Academic Press, 1966.

79) P. Sahoo, M. M. Collur and T. DebRoy, Met. Trans. B (in press).

80) W. G. Schrenk, Applied Spectroscopy, vol. 42, No. 1, pp. 4-11, 1988.

81) F. Brech and L. Cross, Applied Spectroscopy, vol. 16, No. 59, p. 59.,1962.

82) C. J. Belle and J. D. Johnson, Applied Spectroscopy., vol. 27, No. 2, pp. 118-124, 1973.

83) D. A. Cremers, Applied Spectroscopy., vol. 41, No. 4, pp. 572-579, 1987.

84) W. G. Schrenk, Analytical Atomic Spectroscopy, Plenum Press, New York, pp. 169-210, 1975.

85) H. C. Dilworth, X Ray and optical emission analysis of high-temperature alloys., A symposium presented at the sixty-seventh annual meeting of ASTM, Chicago, Illinois, June 23rd, 1964.

86) M. M. Collur, A. Paul and T. DebRoy, Metall. Trans., vol. 18B, pp. 733-740, 1987.

87) H. C. Peebles, Private Communication, Sandia National Laboratories, n New Mexico, May 1988.

88) P. Sahoo and T. DebRoy, Materials Letters (in press).

89) A. Paul and T. DebRoy, Met. Trans. B. (in press).

90) R. Miller, Unpublished Research, The Pennsylvania State University.

91) R. B. Bird, W. E. Stewart and E. N. Lightfoot, Transport Phenomena, John Wiley & Sons, Inc., New York, p.521, 1966.

92) M. M. Collur and T. DebRoy, <u>Met. Trans. B. (in press).</u>

Appendix A

EQUILIBRIUM VAPOR PRESSURE DATA USED

The equilibrium vapor pressure of the various vaporizing species over the respective pure liquids expressed were calculated using the following equations.

Iron[61] :

$$\log P_{Fe} = -24.609 \times 10^3/T - 8.321 \log T + 0.6686 \times 10^{-3}/T - 0.305 \times 10^{-7} T^2 + 38.002$$ where P_{Fe} is in torr (mm Hg) and T is temperature in K.

Manganese[61,62] :

The vapor pressure of manganese at temperatures less than 2900K is given by the following equation[62].

$$\log P_{Mn} = -5.58 \times 10^{-4} T - 1.503 \times 10^{4}/T + 7.603$$ where P_{Mn} is in atmospheres and T is temperature in K.

At temperatures greater than 2900K, the vapor pressure of manganese was computed from the following equation[61].

$$\log P_{Mn} = -27.936 \times 10^3/T - 60.675 \log T + 16.026 \times 10^{-3} T - 16.589 \times 10^{-7} T^2 + 190.877$$ where P_{Mn} is in torr (mm Hg) and T is temperature in K.

Chromium[61] :

$$\log P_{Cr} = -13.505 \times 10^3/T + 33.658 \log T - 9.290 \times 10^{-3} T +$$

$$8.381 \times 10^{-7} T^2 - 89.201 \text{ where } P_{Cr} \text{ is in torr (mm Hg) and T is}$$

temperature in K.

Nickel[61] :

$$\log P_{Ni} = -3.519 \times 10^3/T + 74.940 \log T - 18.042 \times 10^{-3} T +$$

$$15.140 \times 10^{-7} T^2 - 216.422 \text{ where } P_{Ni} \text{ is in torr (mm Hg) and T is}$$

the temperature in K.

Appendix B

ESTIMATION OF ERRORS IN ELECTRON TEMPERATURES

The radial distribution of temperature shown in Figure 29 on page 93 was determined from the local emissivities of the two thermometric peaks of manganese using equation [13]. The primary source of error in the estimation of temperature is the uncertainty in the transition probability data. Since these errors in the available data cannot be estimated with a predetermined level of confidence, the uncertainties in the temperatures presented in Figure 29 on page 93 cannot be estimated with sufficient level of confidence and therefore, the errors are not indicated in this figure. However a rough estimation of the error in temperature was made assuming an error of +25 % in the transition probability data. The upper limit of the temperature was determined by decreasing the transition probability of Mn 5377.63 ^{O}A line by a factor of 25 % and increasing the transition probability of Mn 5341.06 ^{O}A line by a factor of 25 % and calculating a new temperature value using equation [13]. The lower limit of the temperature was determined in a similar manner by appropriately changing the values of the two transition probabilities for the two peaks by 25 %. The average errors in the ten values of electron temperatures reported in Figure 29 on page 93 are +22 % and -15 % for the upper and lower limits, respectively.

The errors in the electron temperatures reported in Table 6 on page 86 were calculated from the uncertainties in the slopes of the plots used to determine temperature values such as the one presented in Figure 26 on page 85. The errors correspond to an 80 % confidence interval for the slope and were calculated by a standard regression technique (88). It is to be noted that the slope of the plot in Figure 26 on page 85 is a nonlinear function of electron temperature. Although statistically the slope has equal uncertainties in both upper and lower limits, this does not translate into equal errors in the upper and lower limits of temperature values because of the hyperbolic relation between the slope of the line and temperature.

Appendix C

COMPUTER PROGRAMS

C.1   Program to conduct Abel Inversion by Barr's Method in BASIC

```
10   REM PROGRAM TO ABEL INVERT BY BARRS METHOD
20   DIM A(20),B(20),A1(20),B1(20),C(20),C1(20),T(20),AA(20)
30   REM N IS THE NUMBER OF TRACKS
40   N = 16
50   REM READ DATA FOR THE MN 5377.63 ANGSTROM PEAK
60   FOR I = 1 TO N
70   READ A(I)
80   LPRINT "A AT " I " = " A(I)
90   C(I) = A(I)
100  NEXT I
110  GOSUB 410
120  FOR I = 1 TO N
130  A1(I) = C1(I)
140  PRINT " A1 AT " I " = "A1(I)
150  LPRINT " A1 AT " I " = "A1(I)
160  NEXT I
170  REM READ THE DATA FOR THE MN 5341.06 ANGSTROM PEAK
180  FOR I = 1 TO N
190  READ B(I)
200  LPRINT " B AT " I " = B(I)
210  C(I) = B(I)
220  NEXT I
230  GOSUB 410
240  FOR I = 1 TO N
250  B1(I) = C1(I)
260  PRINT " B1 AT " I " = " B1(I)
270  LPRINT " B1 AT " I " = " B1(I)
280  NEXT I
290  REM CALCULATION OF TEMPERATURE VALUES FROM ABEL
         INVERTED VALUES
300  V = 0.62489 * (49591 - 35770)
310  U = (LOG(1.68/0.112))/(2.302585)
320  W = (LOG(5377.63/5341.06))/(2.302585)
330  FOR I = 1 TO N
340  AA(I) = A1(I)/B1(I)
```

```
350  AA(I)  =  LOG(AA(I))/(2.302585)
360  T(I)  =  (V)/(U-W-AA(I))
370  PRINT " TEMP AT " I " = " T(I)
380  LPRINT " TEMP AT " I " = " T(I)
390  NEXT I
400  GOTO 610
410  REM SUBROUTINE ABEL INVERSION
420  C1(1) = 0.2029*C(1) + 0.4439*C(2) - 0.1791*C(3)
         - 0.5111*C(4) - 0.1298*C(5) - 0.0095*C(6) -
         - 0.0237*C(7) - 0.0193*C(8) - 0.0152*C(9) -
         - 0.0122*C(10) - 0.0099*C(11) - 0.0082*C(12)
         - 0.0069*C(13) - 0.0059*C(14) - 0.0051*C(15)
         - 0.0044*C(16) - 0.0039*C(17)
430  C1(2) = 0.1831*C(1) + 0.4041*C(2) + 0.1778*C(3)
         - 0.4342*C(4) - 0.1299*C(5) - 0.0204*C(6)
         - 0.0262*C(7) - 0.0203*C(8) - 0.0157*C(9)
         - 0.0157*C(9) - 0.0125*C(10) - 0.0101*C(11)
         - 0.0084*C(12) - 0.007*C(13) - 0.006*C(14)
         - 0.0051*C(15) - 0.0045*C(16) - 0.0039*C(17)
440  C1(3) = 0.1239*C(1) + 0.2847*C(2) + 0.174*C(3)
         - 0.2034*C(4) - 0.1304*C(5) - 0.0531*C(6)
         - 0.0338*C(7) - 0.0235*C(8) - 0.0173*C(9)
         - 0.0134*C(10) - 0.0107*C(11) - 0.0087*C(12)
         - 0.0073*C(13) - 0.0061*C(14) - 0.0053*C(15)
         - 0.0046*C(16) - 0.0045*C(17)
450  C1(4) = 0.1324*C(2) + 0.1936*C(3) + 0.0928*C(4)
         - 0.0964*C(5) - 0.0969*C(6) - 0.0501*C(7)
         - 0.0292*C(8) - 0.0202*C(9) - 0.015*C(10)
         - 0.0117*C(11) - 0.0094*C(12) - 0.0077*C(13)
         - 0.0065*C(14) - 0.0055*C(15) - 0.0047*C(16)
         - 0.0041*C(17)
460  C1(5) = 0.1172*C(3) + 0.1523*C(4) + 0.0722*C(5)
         - 0.0538*C(6) - 0.081*C(7) - 0.046*C(8)
         - 0.026*C(9) - 0.0179*C(10) - 0.0133*C(11)
         - 0.0104*C(12) - 0.0084*C(13) - 0.0069*C(14)
         - 0.0058*C(15) - 0.005*C(16) - 0.0043*C(17)
470  C1(6) = 0.1036*C(4) + 0.1291*C(5) + 0.0636*C(6)
         - 0.0033*C(7) - 0.0714*C(8) - 0.0431*C(9)
         - 0.0236*C(10) - 0.0162*C(11) - 0.012*C(12)
         - 0.0094*C(13) - 0.0076*C(14) - 0.0063*C(15)
         - 0.0053*C(16) - 0.0046*C(17)
480  C1(7) = 0.093*C(5) + 0.114*C(6) + 0.0586*C(7)
         - 0.0214*C(8) - 0.0646*C(9) - 0.0403*C(10)
         - 0.0217*C(11) - 0.0148*C(12) - 0.0111*C(13)
         - 0.0087*C(14) - 0.007*C(15) - 0.0058*C(16)
         - 0.0049*C(17)
490  C1(8) = 0.0847*C(6) + 0.1032*C(7) + 0.0551*C(8)
         - 0.0142*C(9) - 0.0595*C(10) - 0.038*C(11)
         - 0.0202*C(12) - 0.0138*C(13) - 0.0103*C(14)
         - 0.0081*C(15) - 0.0065*C(16) - 0.0054*C(17)
500  C1(9) = 0.0781*C(7) + 0.0951*C(8) + 0.0524*C(9)
         - 0.0095*C(10) - 0.0555*C(11) - 0.0359*C(12)
```

```
        - 0.0189*C(13) - 0.0129*C(14) - 0.0096*C(15)
        - 0.0075*C(16) - 0.0061*C(17)
510  C1(10) = 0.0727*C(8) + 0.0886*C(9) + 0.0501*C(10)
        - 0.0063*C(11) - 0.0522*C(12) - 0.0342*C(13)
        - 0.0179*C(14) - 0.0122*C(15) - 0.0091*C(16)
        - 0.0071*C(17)
520  C1(11) = 0.0682*C(9) + 0.0834*C(10) + 0.0482*C(11)
        - 0.0039*C(12) - 0.0495*C(13) - 0.0326*C(14)
        - 0.017*C(15) - 0.0115*C(16) - 0.0086*C(17)
530  C1(11) = 0.0682*C(9) + 0.0834*C(10) + 0.0482*C(11) -
        0.0039*C(12) - 0.0495*C(13) - 0.0326*C(14)
        - 0.017*C(15)- 0.0115*C(16) - 0.0086*C(17)
540  C1(12) = 0.0644*C(10) + 0.079*C(11) + 0.0465*C(12) -
        0.0022*C(13) - 0.047*C(14) - 0.0313*C(15)
        - 0.0162*C(16) - 0.011*C(17)
550  C1(13) = 0.0612*C(11) + 0.0752*C(12) + 0.045*C(13) -
        0.0009*C(14) - 0.045*C(15) - 0.0301*C(16)
        - 0.0155*C(17)
560  C1(14) = 0.0583*C(12) + 0.072*C(13) + 0.0437*C(14) +
        0.0001*C(15) - 0.0432*C(16) - 0.029*C(17)
570  C1(15) = 0.0558*C(13) + 0.0691*C(14) + 0.0424*C(15) +
        0.0009*C(16) - 0.0416*C(17)
580  C1(16) = 0.0536*C(14) + 0.0666*C(15) + 0.0413*C(16) +
        0.0015*C(17)
590  C1(17) = 0.0517*C(15) + 0.0643*C(16) + 0.0402*C(17)
600  RETURN
610  STOP
620  REM DATA CHECK
630  DATA 2711,2807,3044.5,3411,2450,1807.5,805.5,180,24,0
640  DATA 3169,3228.5,3658,4094.5,3039.5,2083,1168.5,216,
        60,0
```

C.1.1   List of important variables.

A   Experimental intensities of Mn 5377.63 angstrom peak.

B   Experimental intensities of Mn 5341.06 angstrom peak.

A1   Local emissivities of Mn 5377.63 angstrom peak.

A2   Local emissivities of Mn 5341.06 angstrom peak.

T   Plasma temperature.

C.2   Program for the calculation of number density of electrons in BASIC

```
10   REM PROGRAM SPECIES DENSITY
20   DEFDBL A-H,O-Z
30   DIM ZIM(100),ZAM(100),SIM(100),SAM(100),ZIC(100),
     ZAC(100,SIC(100),SAC(100),ZIF(100),ZAF(100)
     SIF(100),SAF(100)
40   DIM T(100),ZIH(100),ZAH(100),TI(100),TA(100),
     SAH(100),SIH(100)
50   DIM TH(100),TM(100),TF(100),TC(100),TAI(100)
60   ZAH = 1
70   ZIH = 2
80   REM DECLARE THE IONIZATION POTENTIALS IN ELECTRON VOLTS
90   VM = 7.432
100  VF = 7.87
110  VC = 6.764
120  VHE = 24.581
130  C = 0.69476
140  LPRINT " TOTAL NEUTRALS  TOTAL IONS  TOTALIONT   TEMP
     IN K "
150  FOR I = 1 TO 60
160  T(I) = 4000 + (I-1)*100
170  D = T(I)*C
180  REM CALCULATION OF PARTITION FUNCTION AND NUMBER
     DENSITY FOR MN
190  ZAM(I) = 6 + (74*EXP(-19751.32/D)) +
     (86*EXP(-27059.45/D)) + (96*EXP(-33839.52/D)) +
     + (104*EXP(-37783.14)) + (100*EXP(-43308.07/D)) +
     + (90*EXP(-45539.56/D)) + (130*EXP(-47245.36/D))
200  ZIM(I) = 7 + (5*EXP(-9472.86/D)) + (25*EXP(-14712.2/D))
     + (45*EXP(-27575.68/D)) + (76*EXP(-30659/D)) +
     (88*EXP(-34112.51/D)) + (86*EXP(-40413.18/D))
210  C1 = 2*2.41*(ZIM(I)/ZAM(I))*((T(I)^1.5)*
     *EXP(-VM/(0.00008615*T(I))))*(10)^15
220  C2 = 7.34D + 21/(T(I))
230  SIM(I) = ((4*C1*C1 + 4*C1*C2)^0.5 - 2*C1)/(2)
240  SAM(I) = (SIM(I)*SIM(I))/C1
250  TM(I) = 2*SIM(I) + SAM(I)
260  REM CALCULATION OF PARTITION FUNCTION AND NUMBER
     DENSITY FOR CR
270  ZAC(I) = 7 + (5*EXP(-7593.16/D)) + (25*EXP(-7978.37/D))
     + (60*EXP(-21018.9/D)) + (88*EXP(-23899.9/D)) +
     156*EXP(-26106.55/D)) + (113*EXP(-29201.73/D)) +
     + (145*EXP(-32103.45/D))
280  ZAC(I) = ZAC(I) + (83*EXP(-34798.4/D)) +
     (125*EXP(-36701.46/D)) + (99*EXP(-40659.81/D))
290  ZIC(I) = 6 + (30*EXP(-12188.7/D))
     + (68*EXP(-20592.5/d)) + (102*EXP(-26617.47/D))
     + (158*EXP(-31630.1/D)) + (138*EXP(-38475.4/D)) +
     + (134*EXP(-47517.2/D)
```

```
300  C1 = 2.41*2*(ZIC(I)/ZAC(I))*((T(I)^1.5)*)
     EXP(-VC/0.000086*T(I))*(10)^15
310  SIC(I) = ((4*C1*C1 + 4*C1*C2)^0.5 - 2*C1)/(2)
320  SAC(I) = (SIC(I)*SIC(I))/C1
330  TC(I) = 2*SIC(I) + SAC(I)
340  REM CALCULATION OF PARTITION FUNCTION AND NUMBER
     DENSITY FOR FE
350  ZAF(I) = 9 + (7*EXP(-415.95/D)) + (3*EXP(-704.0/D)) +
     (3*EXP(-888.132/D)) + EXP(-978.074/D)) +
     (11*EXP(-6928.28/D)) + (9*EXP(-7376.77/D)) +
     (7*EXP(-7728.07/D)) + (5*EXP(-7985.79/D)) +
     (3*EXP(-8154.72/D)) + (21*EXP(-12501.93/D))
360  ZAF(I) = ZAF(I) + (24*EXP(-18528.86/D)) +
     (89*EXP(-19996.07/D)) + (133*EXP(-23197.56/D))
     + (91*EXP(-25901.58/D)) + (82*EXP(-28266.73/D))
     + (141*EXP(-32519.08/D)) + (158*EXP(-36233.17/D))
     + (105*EXP(-40513.275/D))
370  ZIF(I) = 10 + (8*EXP(-384.77/D)) + (6*EXP(-667.64/D))
     + (4*EXP(-862.63/D)) + (2*EXP(-977.03/D))
     + (10*EXP(-1872.6/D)) + (8*EXP(2430.08/D))
     + (6*EXP(-2837.94/D)) + (4*EXP(-3117.48/D))
     + (8*EXP(-7955.24/D)) + (6*EXP(-8391.92/D))
     + (4*EXP(-8680.47/D))
380  ZIF(I) = ZIF(I) + (2*EXP(-8846.76/D))
     + (12*EXP(-13684.17/D)) + (18*EXP(-16107.05/D)) +
     (6*EXP(-18623.7/D)) + (44*EXP(-21146.23/D)) +
     (78*EXP(-22301.25/D)) + (96*EXP(-27050.24/D)) +
     (90*EXP(-33213.47/D)) + (82*EXP(-40305.79/D))
390  ZIF(I) = ZIF(I) + (102*EXP(-45327.69/D))
400  C9 = EXP(-VF/(0.000086*T(I)))
410  C1 = 2.41*2*(ZIF(I)/ZAF(I))*((T(I)^1.5))*(C9*(10)^15)
420  C2 = 7.34D + 21/T(I)
430  SIF(I) = ((4*C1*C1 + 4*C1*C2)^0.5 - 2*C1)/2
440  SAF(I) = (SIF(I)*SIF(I))/C1
450  TF(I) = 2*SIF(I) + SAF(I)
460  REM CALCULATION OF NUMBER DENSITY OF HELIUM
470  C1 = 2.41*2*(ZIH/ZAH)*((T(I)^1.5))
     *((EXP(-VHE/(00008615*T(I)))*(10)^15
480  SIH(I) = ((4*C1*C1 + 4*C1*C2)^0.5 - 2*C1)/2)
490  SAH(I) = (SIH(I)*SIH(I))/C1
500  TH(I) = 2*SIH(I) + SAH(I)
510  REM TOTAL NUMBER DENSITY OF SPECIES IN THE PLASMA
520  REM TAKE THE WEIGHTED AVERAGE USING MOLE FRACTIONS
530  REM OF FE, MN, CR AND HE
540  TA(I) = 0.001733*SAM(I) + 0.002011*SAF(I)
     + 0.00051192*SAC(I) + 0.99574*SAH(I)
550  TI(I) = 0.001733*SIM(I) + 0.002011*SIF(I) +
     0.0005192*SIC(I) + 0.99574*SIH(I)
560  TAI(I) = 2*TI(I) + TA(I)
570  REM TOTAL NUMBER DENSITY IF PLASMA IS NOT WELL MIXED
580  TA(I) = CMN*SAM(I) + CFE*SAF(I) + CCR*SAC(I)
     + CHE*SAH(I)
```

```
590  TI(I) = CMN*SIM(I) + CFE*SIF(I) + CCR*SIC(I)
        + CHE*SIH(I)
600  TAI(I) = 2*TI(I) + TA(I)
610  LPRINT " USING  #.####^^^^ " TA(I),TI(I),TAI(I),T(I)
620  NEXT I
630  STOP
```

C.2.1   List of important variables.

ZIM Array containing partition function of manganese ions.

ZAM Partition function of manganese atoms.

ZIH Partition function of helium ions.

ZAH Partition function of helium atoms.

ZIC Partition function of chromium ions.

ZAC Partition function of chromium atoms.

ZIF Partition function of iron ions.

ZAF Partition function of iron atoms.

SIM Number density of manganese ions.

SAM Number density of manganese atoms.

SIH Number density of helium ions.

SAH Number density of helium atoms.

SIC Number density of chromium ions.

SAC Number density of chromium atoms.

SIF Number density of iron ions.

SAF Number density of iron atoms.

T   T is the electron temperature.

TI Total number density of ions in the plasma.

TA Total number density of atoms in the plasma.

TC Total number density of chromium species in the plasma.

TM Total number density of manganese species in the plasma.

TF Total number density of iron species in the plasma.

TH Total number density of helium species in the plasma.

Appendix D

DATA USED FOR THE CALCULATION OF PARTITION FUNCTIONS FOR MANGANESE, IRON AND CHROMIUM IN THEIR ATOMIC AND IONIC STATES

In this appendix the data required for the calculation of partition functions, viz., degeneracy g_j and the upper energy level u_j for various species in both their ionic and atomic states are presented. These values of g_j and u_j along with the boltzmann constant k can then be substituted in equation [15] at a given temperature for various energy levels and the corresponding degeneracies from which the corresponding partition functions can be obtained. For each of the species, viz., Mn, Fe and Cr, various energy levels and degernacies exist which are different for their ionic and atomic states. These values are presented in the tables provided in this appendix from the data listed by Moore (75).

Table 15: Degeneracy and energy values for manganese for both ionic and atomic states for various levels.

Energy Level (i)	Degeneracy of atom (g_i)	Energy of atom $(E_i$ in cm$^{-1})$	Degeneracy of ion (g_i)	Energy of ion $(E_i$ in cm$^{-1})$
1	6	0	7	0
2	74	19751.32	5	9472.86
3	86	27059.45	25	14712.2
4	96	33839.52	45	27575.68
5	104	37783.14	76	30659.0
6	100	43308.07	88	34112.51
7	90	45539.56	86	40413.18
8	130	47245.36	-	-

Table 16:   Degeneracy and energy values for iron for both ionic and
            atomic states for various levels.

Energy Level (i)	Degeneracy of atom (g_i)	Energy of atom (E_i in cm^{-1})	Degeneracy of ion (g_i)	Energy of ion (E_i in cm^{-1})
1	9	0	10	0
2	7	415.95	8	384.77
3	3	704.0	6	667.64
4	3	888.13	4	862.63
5	1	978.07	2	977.03
6	11	6928.28	10	1872.6
7	9	7376.77	8	2430.08
8	7	7728.07	6	2837.94
9	5	7985.79	4	3117.48
10	3	8154.72	8	7955.24

Table 17:   Degeneracy and energy values for chromium for both ionic and atomic states for various levels.

Energy Level (i)	Degeneracy of atom (g_i)	Energy of atom $(E_i$ in cm$^{-1})$	Degeneracy of ion (g_i)	Energy of ion $(E_i$ in cm$^{-1})$
1	7	0	6	0
2	5	7593.16	30	12188.70
3	25	7978.37	68	20592.50
4	60	21018.9	102	26617.47
5	88	23899.9	158	31630.10
6	156	26106.55	138	38475.40
7	113	29201.73	134	47517.20
8	145	32103.45	-	-
9	83	34798.40	-	-
10	125	36701.46	-	-
11	99	40659.81	-	-

Appendix E

FORMALISM UTILIZED FOR THE COMPUTATION OF

CONCENTRATION PROFILES FROM GIVEN VELOCITY

PROFILES.

In this appendix the computation scheme utilized for the determination of the concentration profiles from a given velocity profile data (obtained from FLUENT) will be discussed. A schematic of the grid arrangement used for the calculation is presented in Figure 43. There are ten cells in the radial direction each of width 0.25 mm while there are fifteen cells in the axial direction each of width 0.45 mm.

A schematic of the control volume utilized for these calculations is presented in Figure 44. The location of the velocity vectors of helium gas with respect to the location of concentrations is presented in this figure. It should be noted that the north and south areas are equal to each other while the west area is always smaller than the east area. The angle θ shown in the figure was taken as 180 degrees in the present study.

In Figure 44 at steady state the total amount of mass flux entering is equal to the total amount of mass flux leaving. The directions of the various fluxes in the north, south, east and west directions are indicated in the figure. The various flux terms in different directions are given below:

Convective mass flux in moles/sec. at west face $=$ CW

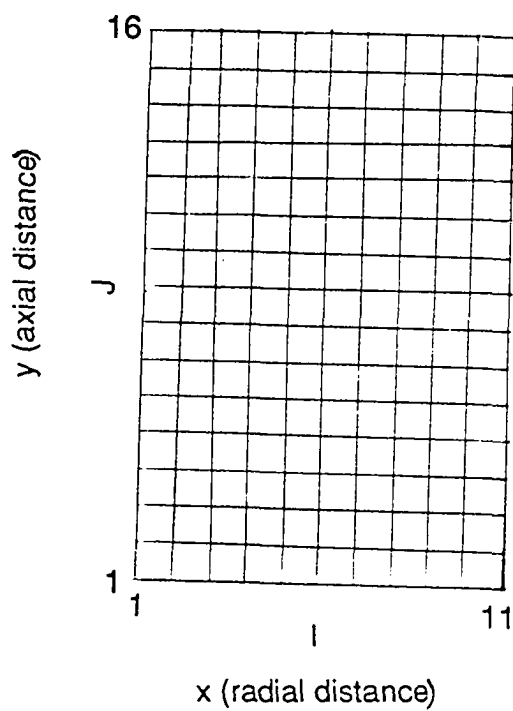$$= DAY1(I)^{*}U(I,J)^{*}(C(I,J) + C(I-1,J))/2$$

Figure 43: Schematic of the grid arrangement used in the computer program for the computation of the concentration profiles.
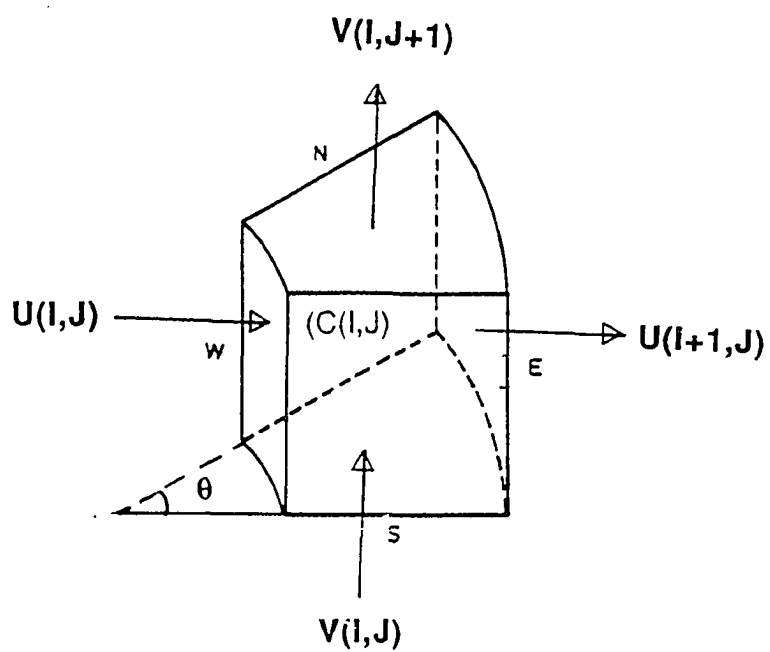
Figure 44: Schematic of the control volume used for setting up the finite difference equations

where DAY1(I) is the area of the west face, C(I,J) is the concentration in moles/cm^3 of the reference cell and C(I-1,J) is the concentration of the cell located to the left of the reference cell with indicees I and J.

Convective mass flux in moles/sec. at east face = CE

$$= DAY1(I+1)^*U(I+1,J)^*(C(I+1,J) + C(I,J))/2$$

where DAY1(I+1) is the area of the east face and C(I+1,J) is the concentration of the cell to the right of the reference cell with indicees I and J. Similarly convective mass fluxes in moles/sec. at the north and south faces are given by

$$DAX1(I)^*V(I,J+1)^*(C(I,J+1) + C(I,J))/2 \text{ and}$$

$$DAX1(I)^*V(I,J)^*(C(I,J-1) + C(I,J))/2 \text{ respectively.}$$

Diffusive mass flux at west face = DW

$$= DAY1(I)^*DF^*(C(I-1,J) - C(I,J))/DX1$$

where DF is the interdiffusivity of iron in helium which was calculated using the chapman-enskog equation at a temperature of about 2670 K (the average temperature in the boundary layer whose thickness was determined to be 1.8 mm for the present system) and DX1 is the increment in the X direction. In addition, the diffusivity was assumed constant throughout the computation domain and the same value of interdiffusivity was used for manganese and iron.

Diffusive mass flux at east face = DE

$$= DAY1(I+1)^*DF^*(C(I,J) - C(I+1,J))/DX1$$

Similarly, diffusive fluxes for the north and the south faces are given by DAX1(I)*DF*(C(I,J+1) - C(I,J))/DY1 and DAX1(I)*DF*(C(I,J) - C(I,J-1))/DY1 respectively where DY1 is the increment in the Y direction.

One can then write a mass balance equation as follows:

$$CW + DW - CE - DE + CN + DN - CS - DS = 0$$

The above finite difference equation was solved with the appropriate boundary conditions discussed below using the tridiagonal matrix algorithm.

E.1 Left-hand boundary

There is no mass flux entering from the west side resulting in $CW + DW = 0$. With this boundary condition a TDMA on the left hand boundary was executed.

E.2 Bottom boundary at the sample

$C(1,1) = 1.67 \times 10^{-6}$ Moles/cm^3 corresponding to the equilibrium concentration of iron at 2670 K at a partial pressure of iron of 0.368 atm. (calculated from the mole fraction of iron and the equilibrium vapor pressure of pure iron at the weld pool temperature of about 3000 K). Similar values were determined for manganese and and chromium and used in the program as the node boundary condition.

In addition, at the bottom boundary, the value of $C(2,1)$ was calculated from the value of $C(1,1)$, $C(1,2)$ and the vaporization rate JI (obtained from experimental data). This was obtained by a simple mass balance on the cell with indicees of I and J each being equal to 1. For cells with I indices ranging from 3 through 10, $C(I,1)$ was equated to $C(I,2)$.

E.3 Top boundary condition

The concentration values are zero as they are very far off from the source where the mass or vaporized material originates.

E.4 Tridiagonal matrix algorithm

The tridiagonal matrix algorithm (also known as the Thomas algorithm) is an iterative technique to solve a set of simultaneous equations. It is a special case of gauss elimination in which the coefficient matrix is tridiagonal. This method has been adapted for the present work in the following manner.

Suppose we have a variable ϕ and the TDMA direction is north-south i.e. at one time we are only solving for values of the variable in the north-south direction. Then the solution of the equation

$$AA.\phi(I+1) + BB.\phi(I-1) + CC = DD.\phi(I)$$

is

$$\phi(I) = PP(I).\phi(I+1) + Q(I) \quad \text{for } I = N\text{-}1 \text{ to } 2$$

$$\text{where } PP(I) = \frac{AA(I)}{DD(I) - BB(I) \cdot PP(I-1)} \quad \text{for } I = 2 \text{ to } N-1 \quad \text{and } PP(1) = 0$$

where $\phi(I-1)$ is to the north of $\phi(I)$ and $\phi(I+1)$ is to the south of $\phi(I)$. To use this technique, solutions at the two ends (north and south) must be known. The solution is started at the left end of the computational domain where the solution is known (boundary conditions). The variable is now calculated at all

points on the next north-south line. In this way values of the variable are calculated on a line of constant x. But this value depends upon not-so-correct variables on the two adjacent lines of the current line. So this procedure is applied to the entire mesh several times till the maximum difference at any location between sweeps is less than a predetermined value. This gives us the steady state solution.

```
10 REM PROGRAM USING TDMA ALGORITHM TO CALCULATE THE
     CONCENTRATION PROFILES OF MN, FE AND CR FROM GIVEN
VALUES
     OF U AND V VELOCITIES OBTAINED FROM FLUENT SOFTWARE.
20 DEFDBL V(40,20),U(40,20)
30 DIM C(30,20),CN(30,20),A(30),B(30),D(30),CC(30),P(30),Q(30)
40 DIM X1(30),Y1(20),DAX1(30),DAY1(30),CO(30,20)
50 REM INPUT THE TOTAL VAPORIZATION RATE OF SPECIES I IN
MOLES/SEC.
50 REM VAPORIZATION RATE FOR MANGANESE
60 REM JI = 0.000142/54.94
70 REM VAPORIZATION RATE FOR IRON
80 JI = 0.000165/55.85
90 REM VAPORIZATION RATE FOR CHROMIUM
100 REM JI = 0.0000426/52
110 REM READ THE U AND V VELOCITIES FROM THE OUTPUT OF
FLUENT
120 FOR J = 1 TO 15
130 U(1,J) = 0
140 NEXT J
150 FOR J = 1 TO 15
160 READ U(2,J)
170 NEXT J
180 FOR J = 1 TO 15
190 READ V(2,J)
200 NEXT J
210 FOR J = 1 TO 15
220 READ U(3,J)
230 NEXT J
240 FOR J = 1 TO 15
250 READ V(3,J)
260 NEXT J
270 FOR J = 1 TO 15
280 READ U(4,J)
290 NEXT J
300 FOR J = 1 TO 15
310 READ V(4,J)
320 NEXT J
330 FOR J = 1 TO 15
```

```
340 READ U(5,J)
350 NEXT J
360 FOR J = 1 TO 15
370 READ V(5,J)
380 NEXT J
390 FOR J = 1 TO 15
400 READ U(6,J)
410 NEXT J
420 FOR J = 1 TO 15
430 READ V(6,J)
440 NEXT J
450 FOR J = 1 TO 15
460 READ U(7,J)
470 NEXT J
480 FOR J = 1 TO 15
490 READ V(7,J)
500 NEXT J
510 FOR J = 1 TO 15
520 READ U(8,J)
530 NEXT J
540 FOR J = 1 TO 15
550 READ V(8,J)
560 NEXT J
570 FOR J = 1 TO 15
580 READ U(9,J)
590 NEXT J
600 FOR J = 1 TO 15
610 READ V(9,J)
620 NEXT J
630 FOR J = 1 TO 15
640 READ U(10,J)
650 NEXT J
660 FOR J = 1 TO 15
670 READ V(10,J)
680 NEXT J
690 FOR J = 1 TO 15
700 READ U(11,J)
710 NEXT J
720 FOR J = 1 TO 15
730 READ V(11,J)
740 NEXT J
750 WIDTH "LPT1:",233
760 LPRINT CHR$(15):
770 FOR J = 1 TO 15
780 FOR I = 1 TO 10
790 V(I,J) = -V(I,J)
800 NEXT I
810 NEXT J
820 FOR J1 = 15 TO 1 STEP -1
830 FOR I = 1 TO 11
840 LPRINT USING " + #.###^^^^ " U(I,J1)
850 NEXT I
```

```
860 LPRINT
870 NEXT J1
880 REM END OF READING AND PRINTING THE VELOCITIES
890 REM INPUT THE GRID SIZE IN X AND Y DIRECTIONS IN CMS
900 DX1 = 0.025
910 DY1 = 0.045
920 REM INPUT THE INTERDIFFUSIVITY OF SPECIES I IN HELIUM IN
930 REM SQ.CM/SEC.
940 DF = 28.24
950 REM GENERATION OF GRIDS
960 FOR I = 1 TO 15
970 X1(I) = 0.025*(I-1)
980 NEXT I
990 FOR J = 1 TO 16
1000 Y1(J) = 0.045*(J-1)
1010 NEXT J
1020 REM CALCULATION OF CELL AREA
1030 FOR I = 1 TO 15
1040 REM DAX1 GENERATES THE NORTH AND SOUTH CELL AREAS
1050 DAX1(I) = 3.142*((X1(I + 1)^2 - X1(I)^2))*0.5
1060 REM DAY1 GENERATES THE EAST AND WEST CELL AREAS
1070 DAY1(I) = 3.142*((X1(I)*DY1))
1080 NEXT I
1090 REM INITIALIZE ALL THE CONCENTRATIONS
1100 FOR J = 1 TO 15
1120 FOR I = 1 TO 10
1130 C(I,J) = 0
1140 NEXT I
1150 NEXT J
1160 K = 1
1170 REM K IS THE NUMBER OF ITERATIONS
1180 PRINT " THE NUMBER OF ITERATIONS COMPLETED IS " K
1190 REM STORE ALL THE OLD CONCENTRATIONS
1200 FOR J = 1 TO 15
1210 FOR I = 1 TO 10
1220 CO(I,J) = C(I,J)
1230 NEXT I
1240 NEXT J
1250 REM INPUT THE CONCENTRATION OF SPECIES I IN MOLES/CU.CM
AT THE
1260 REM WELD POOL
1270 REM INPUT EQUILIBRIUM CONCENTRATION FOR MANGANESE
1280 REM C(1,1) = 2.31748/1000000
1290 REM INPUT EQUILIBRIUM CONCENTRATION FOR IRON
1300 C(1,1) = 1.6798/1000000
1310 REM INPUT EQUILIBRIUM CONCENTRATION FOR CHROMIUM
1320 REM C(1,1) = 1.022/1000000
1330 REM STARTING TDMA ON THE LEFT BOUNDARY
1340 FOR J = 2 TO 14
1350 P(1) = 0
1360 A(J) = (DAX1(1)*V(1,J + 1))/2 + (DAX1(1)*DF)/DY1
1370 CC(J) = -C(2,J)*((DAY1(2)*U(2,J))/2 -
```

```
           (DAY1(2)*DF)/DX1)
1380 B(J) = (-DAX1(1)*V(1,J))/2 + (DAX1(1)*DF)/DY1
1390 D(J) = (DAY1(2)*U(2,J))/2 + (DAY1(2)*DF)/DX1
         - (DAX1(1)*V(1,J + 1))/2 + (DAX1(1)*DF)/DY1
         + (DAX1(1)*V(1,J))/2 + (DAX1(1)*DF)/DY1
1400 P(J) = (A(J))/(D(J) - B(J)*P(J-1))
1410 Q(1) = C(1,1)
1420 Q(J) = (B(J)*Q(J-1) + CC(J))/(D(J) - B(J)*P(J-1))
1430 NEXT J
1440 FOR J = 14 TO 2 STEP -1
1450 C(1,J) = P(J)*C(1,J + 1) + Q(J)
1460 NEXT J
1470 REM BOUNDARY CONDITION AT THE NODE
1480 C1 = (DAY1(2)*U(2,1)/2 - DAY1(2)*DF/DX1)
1490 C2 = (V(1,2)*DAX1(1)/2) - (DF*DAX1(1)/DY1)
         - (U(2,1)*DAY1(2)/2) - (DF*DAY1(2)/DX1)
1500 C3 = (V(1,2)*DAX1(1)/2) + (DAX1(1)*DF/DY1)
1510 C(2,1) = (JI/2 + C(1,1)*C2 + C(1,2)*C3)/C1
1520 REM TDMA APPLIED TO THE BULK
1530 P(1) = 0
1540 FOR I = 2 TO 10
1550 FOR J = 2 TO 14
1560 Q(1) = C(I,1)
1570 D(J) = (DAY1(I)*U(I,J)/2) - (DAY1(I)*DF/DX1)
         - (DAY1(I + 1)*U(I + 1,J)/2) - (DAY1(I + 1)*DF/DX1) +
         (DAX1(J)*V(I,J + 1)/2) - (DAX1(I)*DF/DY1) -
         (DAX1(I)*V(I,J)/2) - (DAX1(I)*DF/DY1)
1580 A(J) = (-DAX1(I)*V(I,J + 1)/2) - (DAX1(I)*DF/DY1)
1590 B(J) = (DAX1(I)*V(I,J)/2) - (DAX1(I)*DF/DY1)
1600 CC(J) = (-DAY1(I)*U(I,J)*C(I-1,J)/2) -
         (DAY1(I)*DF*C(I-1,J)/DX1) +
         (DAY1(I + 1)*U(I + 1,J)*C(I + 1,J)/2) -
         (DAY1(I + 1)*DF*C(I + 1,J)/DX1)
1610 P(J) = A(J)/(D(J) - B(J)*P(J-1))
1620 Q(J) = (B(J)*Q(J-1) + CC(J))/(D(J) - B(J)*P(J-1))
1630 NEXT J
1640 FOR J = 14 TO 2 STEP -1
1650 C(I,J) = P(J)*C(I,J + 1) + Q(J)
1660 NEXT J
1670 NEXT I
1680 REM BOTTOM BOUNDARY CONDITIONS
1690 FOR I = 3 TO 10
1700 C(I,1) = C(I,2)
1710 NEXT I
1720 K = K + 1
1730 FOR J = 1 TO 15
1740 FOR I = 1 TO 10
1750 CN(I,J) = C(I,J)
1760 DIFF = ABS(CN(I,J) - CO(I,J))
1770 IFF DIFF > 1E-08 GOTO 1180
1780 IF K > 100 GOTO 1830
1790 NEXT I
```

```
1800 NEXT J
1810    LPRINT    "NUMBER    OF    ITERATIONS    REQUIRED    FOR
CONVERGENCE = " K
1820 GOTO 1840
1830 LPRINT "CONVERGENCE IS NOT REACHED EVEN AFTER 100
     ITERATIONS"
1840 FOR J1  =  15 TO 1 STEP -1
1850 FOR I  =  1 TO 10
1860 LPRINT USING  " + #.###^^^^ "  C(I,J1);
1870 NEXT I
1880 LPRINT
1890 NEXT J1
1900 DATA -0,-103.8,-181.62,-245.88,-297.34,-337.79,-369.73,-395.28,
     -416.03,-433.15,-447.5,-459.67,-470.07,-478.97,-486.57
1910 DATA 29.356,21.98,18.18,14.54,11.44,9.03,7.22,5.86,4.84,4.05,
     3.44,2.94,2.51,2.15,1.81
1920 DATA -0,-101.83,-178.49,-241.6,-291.86,-331.2,--362.08,-386.67,
     -406.56,-422.93,-436.64,-448.34,-458.47,-467.36,-475.24
1930 DATA 57.87,43.49,35.85,28.58,22.39,17.61,14.03,11.36,9.355,
     7.84,6.67,5.76,5.023,4.41,3.88
1940 DATA -0,-98.15,-172.67,-233.58,-281.7,-319.2,-348.4,-371.5,
     -390.12,-405.4,-418.2,-429.2,-438.83,-447.48,-455.39
1950 DATA 84.83,64.1,52.6,41.75,32.56,25.5,20.25,16.34,13.43,
     11.25,9.62,8.38,7.42,6.66,6.0385
1960 DATA -0,-93.29,-164.76,-222.78,-268.34,-303.5,-330.77,
     -352.25,-369.47,-383.56,-395.37,-405.54,-414.53,-422.68,
     -430.25
1970 DATA 109.78,83.43,68.15,53.85,41.81,32.62,25.8,20.76,
     17.04,14.28,12.24,10.73,9.59,8.73,8.065
1980 DATA -0,-87.74,-155.48,-210.13,-252.88,-285.66,-310.95,
     -330.77,-346.57,-359.46,-370.23,-379.5,-387.7,-395.16,
     -402.13
1990 DATA 132.48,101.21,82.36,64.8,50.12,38.96,30.72,24.65,20.18,
     16.9,14.5,12.75,11.47,10.52,9.82
2000 DATA -0,-81.82,-145.4,-196.6,-236.4,-266.8,-290.1,-308.3,
     -322.7,-334.4,-344.08,352.4,-359.7,-366.38,-372.6
2010 DATA 152.8,117.3,95.14,74.62,57.53,44.56,35.02,28.0,22.86,
     19.11,16.39,14.42,13.0,11.98,11.256
2020 DATA -0,-75.82,-135.0,-182.62,-219.5,-247.6,-269.0,-285.6,
     -298.6,-309.1,-317.73,-325.0,-331.5,-337.32,-342.72
2030 DATA 170.79,131.65,106.5,83.32,64.05,49.44,38.7,30.84,
     25.09,20.91,17.89,15.73,14.19,13.1,12.34
2040 DATA -0,-69.89,-124.75,-168.71,-202.76,-228.6,-248.17,
     -263.17,-274.85,-284.14,-291.72,-298.1,-303.65,-308.62,
     -313.22
2050 DATA 186.5,144.26,116.5,90.95,69.74,53.63,41.81,33.17,26.87,
     22.31,19.0,16.7,15.05,13.9,13.099
2060 DATA -0,-64.16,-114.68,-155.14,-186.43,-210.09,-227.87,-241.35,
     -251.71,-259.85,-266.41,-271.87,-276.56,-280.73,-284.56
2070 DATA 200.05,155.2,125.16,97.55,74.62,57.16,44.36,35.02,28.23,
     23.33,19.83,17.34,15.6,14.39,13.56
2080 DATA -0,-58.69,-105.0,-142.06,-170.69,-192.26,-208.32,-220.32,
```

-229.42,-236.45,-218.71,-222.45,-225.59,-228.32,-230.79
2090 DATA 211.57,164.55,132.55,103.17,78.74,60.07,46.36,36.40,
29.18,23.99,20.29,17.69,18.88,14.62,13.76
2100 DATA -0,-53.52,-95.78,-129.58,-155.66,-175.21,-189.61,-200.2,
-208.09,-214.06,-196.52,-199.49,-201.94,-204.05,-205.95

E.4.1   List of important variables.

U   Horizontal velocity in radial or x direction in cm/sec.

V   Vertical velocity in axial or y direction in cm/sec.

DX1   Increment in the horizontal direction in cm.

DY1   Increment in the vertical direction in cm.

X1   Horizontal coordinate in cm.

Y1   Vertical coordinate in cm.

C   Concentration of a species in moles/cm^3.

CO   Old concentration values calculated at various cells.

CN   New concentration values calculated at various cells.

DF   Interdiffusivity of the vaporizing species in helium
    gas (cm^2/s.)
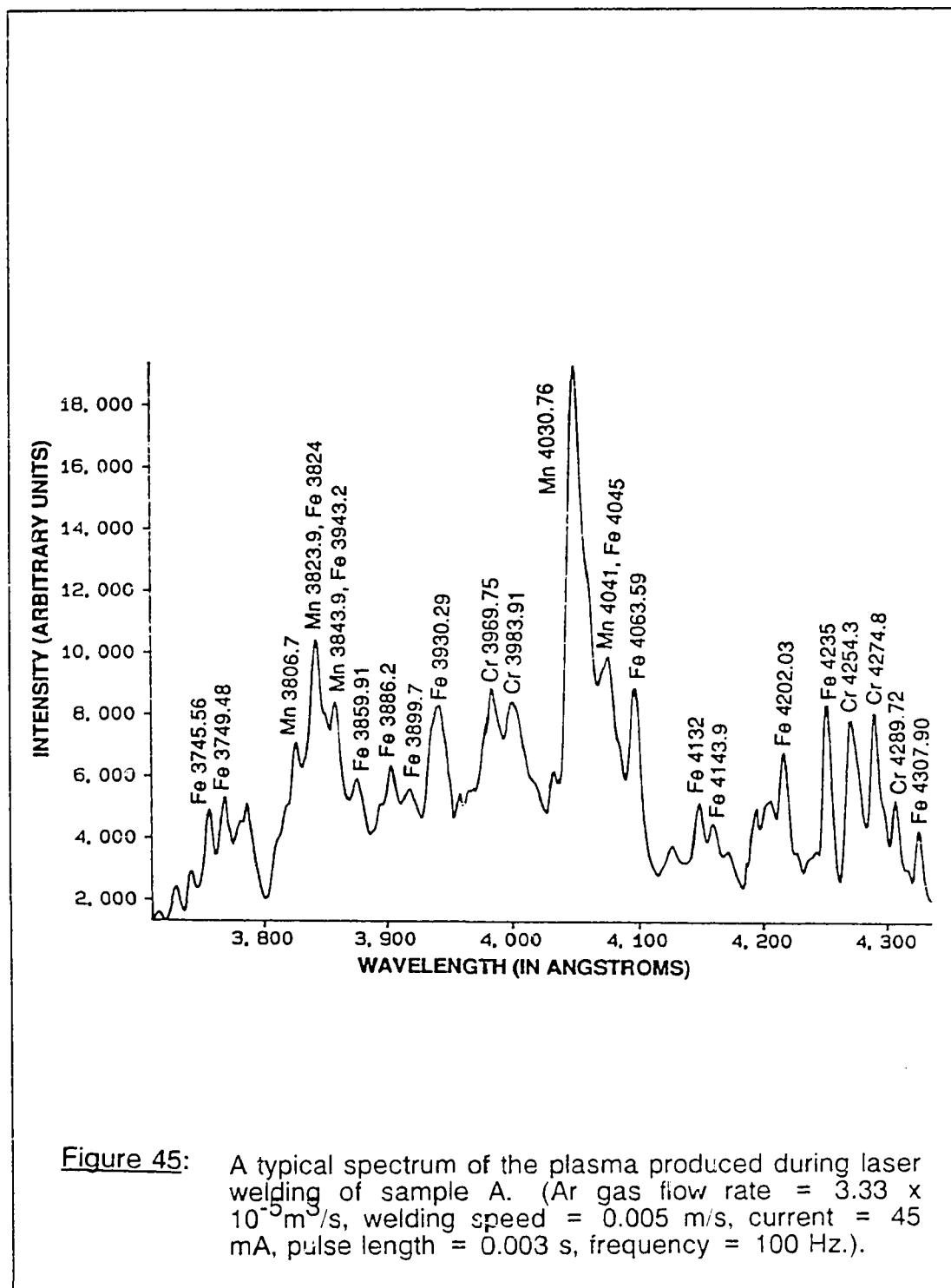
DAY1 Area term in the east and west faces.

DAX1 Area term in the north and south faces.

J   Index in the y or axial direction.

I   Index in the x or radial direction.
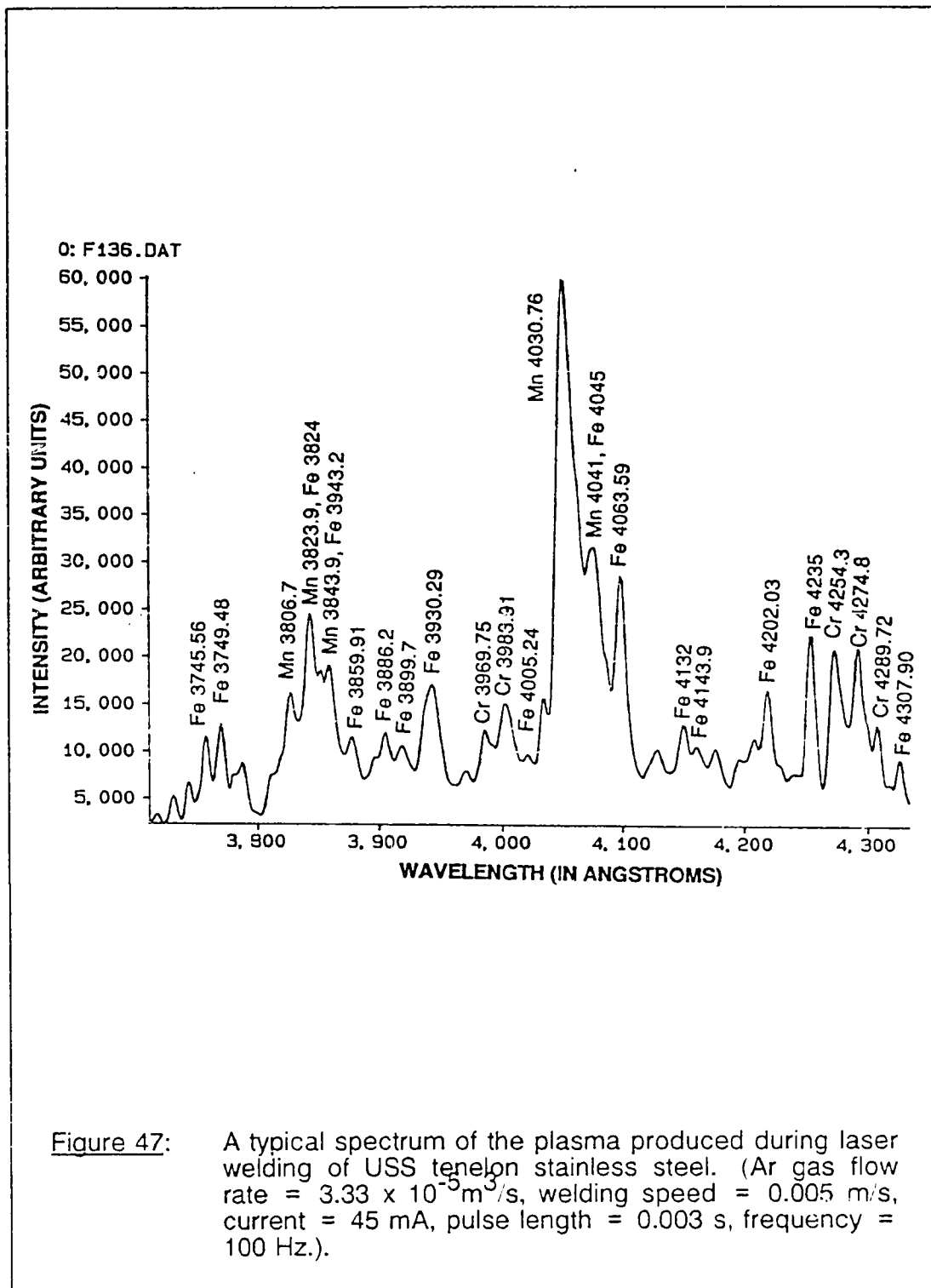
JI   Vaporization rate of species in moles/sec.

Appendix F

TYPICAL SPECTRA CORRESPONDING TO VARIOUS
ALLOYS UTILIZED FOR THE CONSTRUCTION OF THE
CALIBRATION CURVE.

Figure 45: A typical spectrum of the plasma produced during laser welding of sample A. (Ar gas flow rate = 3.33 x $10^{-5} m^3/s$, welding speed = 0.005 m/s, current = 45 mA, pulse length = 0.003 s, frequency = 100 Hz.).

Figure 46: A typical spectrum of the plasma produced during laser welding of sample B. (Ar gas flow rate = 3.33 x $10^{-5}m^3$/s, welding speed = 0.005 m/s, current = 45 mA, pulse length = 0.003 s, frequency = 100 Hz.).

Figure 47:   A typical spectrum of the plasma produced during laser welding of USS tenelon stainless steel. (Ar gas flow rate = 3.33 x 10^{-5}m^3/s, welding speed = 0.005 m/s, current = 45 mA, pulse length = 0.003 s, frequency = 100 Hz.).

VITA

Murali Mohan Collur was born in Vizianagaram, India, on June 28, 1960. In 1977, he entered the Indian Institute of Technology, Kanpur, from where he received his Bachelor of Technology in Metallurgical Engineering in 1982. He started his graduate studies in the fall of 1982 at South Dakota School of Mines and Technology, Rapid City, South Dakota, from where he received a Master of Science in Metallurgical Engineering in December 1983. He then started his doctoral research work at The Pennsylvania State University in spring of 1984 leading to the degree of Doctor of Philosophy in Metals Science and Engineering. He held a research assistantship during his entire graduate studies.

He is a member of the AIME, AWS, MRS and Alpha Sigma Mu. He is the co-author of the following publications.

(1)   "Sintering of 9 % tin-bronze alloys through pre-mixed and pre-alloyed routes," M. M. Collur and G. S. Upadhyaya, Transactions of the Powder Metallurgy Association of India, 1982, vol. 9, pp. 36-40.

(2)   "Mechanism of alloying element vaporization during laser welding," M. M. Collur, A. Paul and T. DebRoy, Metall. Trans., vol. 18B, pp. 733-740, 1987.

(3)   "Emission spectroscopy of plasma during laser welding of stainless steels," M. M. Collur and T. DebRoy, Accepted for publication by Metallurgical Transactions B, 1988 (in press).

(4)   "Effect of oxygen and sulfur on alloying element vaporization rates during laser welding," P. Sahoo, M. M. Collur and T. DebRoy, Accepted for publication by Metallurgical Transactions B, 1988 (in press).